Institute for Measurement Systems and Sensor Technology

Attenuated Total Reflection technique for on-line oil monitoring by means of a FTIR fiber-optic probe

Katarzyna Kudlaty

Vollständiger Abdruck der von der Fakultät für Elektrotechnik und Informationstechnik der Technischen Universität München zur Erlangung des akademischen Grades eines

Doktor-Ingenieurs

genehmigten Dissertation.

Vorsitzender:		Univ.-Prof. Dr. rer. nat. Doris Schmitt-Landsiedel
Prüfer der Dissertation:	1.	Univ.-Prof. Dr.-Ing. habil. Alexander W. Koch
	2.	Univ.-Prof. Dr.-Ing. Markus-Christian Amann

Die Dissertation wurde am 29.04.2004 bei der Technischen Universität München eingereicht und durch die Fakultät für Elektrotechnik und Informationstechnik am 01.10.2004 angenommen.

Abstract

In the presented thesis, infrared measurement techniques adapted to on-line monitoring of the deterioration of lubricants are presented. The deterioration of lubricants is revealed by changes of their infrared spectra. For purposes of on-line monitoring a Fourier-Transform Infrared Spectroscopy (FTIR) was combined with the Attenuated Total Reflectance (ATR) measurement technique using infrared transmitting fibers. The proposed set-up enables direct access to the investigated substances and is characterized by its high measurement sensitivity. The spectroscopic results enabled the development of a novel, robust and industry-suitable ATR-sensor to monitoring of lubricant while in use. The sensor is characterized by a higher mechanical stability and a significant price advantage in comparison to FTIR-ATR-fiber-optic technique. The results obtained from the new sensor concur with those of a traditional spectroscopic investigation to prove the applicability of the proposed solution for the detection of significant degradation of lubricants.

Zusammenfassung

In der vorliegenden Arbeit werden Infrarot-Messtechniken dargestellt, die zur on-line Überwachung von Ölalterungsprozessen in industriellen Anlagen einsetzbar sind. Der Ölalterungsprozess wird durch die Analyse der Infrarot-Spektren der Öle sichtbar. Um diese on-line messen zu können, wird die Fourier-Transform-Infrarot-Spektroskopie (FTIR) mit Abgeschwächter Total-Reflexions-Messtechnik (ATR) mittels Infrarot-Lichtwellenleiter kombiniert. Diese Messanordnung ermöglicht den direkten Zugang zu Proben bei gleichzeitiger Aufrechterhaltung der hohen Sensitivität der Messanordnung. Auf dieser Grundlage wurde ein neuartiger, kompakter, mechanisch stabiler und preiswerter ATR-Sensor, der zur on-line Überwachung des Zustands der Öle geeignet ist, konzipiert, entwickelt und im praktischen Betrieb getestet.

Contents

1 Introduction

1.1 Motivation

Moving parts in industrial devices require lubrication. The efficiency of a production process depends on the quality of this lubrication and on the kind and the quality of the lubricant used. The quality of a lubricant does not remain constant during its use. It changes depending on the loads, operating temperatures, pressures and its working environment. Just as a slight loss of lubricating properties leads to a decrease in the production efficiency through an increase in production costs, an advanced degradation or even a decomposition of a lubricant threatens with serious failures of devices followed by production delays and high repair costs. Thus, an important part of maintenance programs in industrial facilities is the determination of a degradation state of the used lubricant and prediction of its remaining life-time. Similar to the danger connected with an overdue exchange of a lubricant, changing it too early is connected with a series of negative features such as: overly short maintenance intervals followed by production losses, costs of lubricants, which in amounts of thousands of liters can not be neglected, and finally expenses connected with the disposal of old lubricants. It must be emphasized that used lubricants are serious environmental pollutants. Therefore special attention must be given to the disposal programs. In Germany, the yearly consumption of industrial lubricants is on the order of 700 000 tons. About 40 % of this amount is re-refined, 10 % is burned and next 40 % are regenerated. The fate of the last 10 % is unknown [1, 2, 3, 4, 5].

As briefly described above, the determination of the exchange-time of industrial lubricants is an important task. The exchange-time is determined based on results from a periodic analysis conducted off-site in laboratories. A standard analysis is comprised of a refractive index measurement, a viscosity measurement, a Total Acid Number TAN or a Total Base Number TBN determination and infrared spectroscopy. In case of additional uncertainties, more advanced tests are carried out. It must be emphasized that none of above tests separately deliver trustworthy information about the condition of the investigated lubricant. The results from all the tests are collected in so called correlation charts from which final conclusions are drawn. The accuracy of the obtained results is influenced by: the frequency of the analysis (which must increase with time), the quality of extracted samples (whether they are proper representatives of the whole population) and the transport conditions. Additionally, expenses of the shipment and the analysis, together with production losses connected with extraction of samples account for some of the serious disadvantages for the off-site laboratory analysis [5, 6, 7, 8, 9, 10, 11, 12, 13, 14, 15, 16].

Due to these facts, efforts towards the development of a reliable on-line lubricant analysis program have been made for years. As already mentioned, this program must comprise all of standard off-site tests. Presently, there exist on-line working sensors, which measure the dynamic viscosity at 40°C and 100°C - offered by Bode, the density, the water content and the dielectric constant - produced by Bode, Temic or Sentronic and the amount of contaminating particles - offered by Hydac, Mahle or Pall. The sensors that can perform on-line infrared measurements are still not available. For this reason the idea to develop an infrared sensor for on-line lubricant analysis arose.

1.2 Aims of the Study

The following thesis deals with the problems associated with on-line infrared spectroscopy. Infrared spectroscopy is one method to identify the chemical composition of substances on a basis of their specific absorptions originating from transitions between vibrational and rotational energy levels of the molecules. The infrared spectral range divides into far-IR (500-50) μm, mid-IR (2.5-50) μm and near-IR (2.5-0.75) μm. Basic vibrational transitions of particles occur in the mid-IR spectral range. Thus, mid-IR spectra do not contain the overtones, combinational bands and artifacts associated with other areas making the interpretation of results from this area of the infrared spectrum less troublesome [17, 18, 19]. Depending on the type of the measured substance, an infrared measurement can be carried out with techniques known as Transmission, Attenuated Total Reflection (ATR), Specular or Diffuse Reflection [20, 21, 22, 23, 24]. Despite the last two measurement techniques, which can be also used to investigate existing surfaces of solids, samples for infrared measurements must be prepared and placed in specially designed sample cells. An infrared spectrum is created by a dividing a two separately collected sample and reference spectra. Infrared spectrometers are sensitive and expensive devices due to the optics used, as well as in the case of Fourier Transform Infrared (FTIR) spectrometers, due to their built in Michelson Interferometer. For all these reasons, infrared spectroscopy is an established measurement method, but its application field is limited to precisely controlled laboratory conditions and static measurements.

The newest research on the field of infrared spectroscopy has delivered a possibility of on-line reaction monitoring in laboratory conditions through the use of infrared fibers. The fibers for infrared spectral range differ strongly in their composition, structure and mechanical properties from the typical fibers used in visible spectral range. Infrared fibers are usually made of fused silica, silver-halide or chalcogenide glass. Their lengths are limited to few tens of centimeters due to their mechanical sensitivity. Spectroscopic measurements conducted with infrared fibers require extremely stable measurement conditions and sensitive detectors because of the strong light attenuation within the fibers [25, 26, 27, 28, 29, 30, 31].

The aim of the presented study was to prove of the applicability of mid-IR chalcogenide fibers to on-line FTIR monitoring of lubricant aging. First, an inspection of the sensitivity of the measurement set-up had to be made. Next, the aging of lubricants had to be conducted and its on-line monitoring with the set-up carried out. Also, the influence of the changeable temperature of the sample on the measurement results had to be examined. On the basis of FTIR-fiber examinations, a new robust and well-priced ATR-IR sensor, which performs on-line lubricant analysis has been developed.

1.3 Structure of the Thesis

At the beginning of the presented thesis the reader is introduced to problems facing lubrication, lubricant aging and its analysis. In the first chapter a classification of lubricants and additives is presented. The discussion of the aging process is limited to the chemical degradation in a form of oxidation. Because of the wide variety of existing lubricants, the thesis concentrates - as an example - on lubricants for different sorts of gearboxes. In the second chapter the basics of infrared spectroscopy are introduced. Firstly, a physical theory of the origin of infrared absorption is explained. Then the theory of infrared measurement, the construction and function of Fourier-Transform Infrared Spectrometers (FTIR) used in modern research are presented. The applied Attenuated Total Reflectance (ATR) technique is the subject of the third chapter, where the theory, the practical aspects and considerations concerning the applied measurement set-up are discussed. Infrared fibers, their variety, physical and mechanical properties are described in chapter number four. The FTIR-fiber investigations of lubricants as conducted are described in the next chapter. It begins with characteristic features of the measurement set-up, which consists of an FTIR spectrometer, mid-IR fibres, an ATR crystal and a special MCT detector. It continues with the adaptation of the set-up to on-line measurements; herewith the liquid nitrogen filling system, the measurement software and the temperature correction of the collected data. The chapter concludes with the results of static investigations of some received and self aged lubricant samples. Finally, in the sixth chapter the construction and principle of operation of the developed ATR-IR sensor are presented. The usefulness of the sensor is proved by concurring results of the same lubricant samples as compared with results obtained from traditional FTIR-fiber measurements. The summary of the thesis emphasizes once again the advantages and disadvantages of the investigated FTIR-fiber measurement and the developed ATR-IR sensor and indicates the problems to be solved in the future.

2 Lubricants

2.1 Classification and Properties

Lubricants are substances that reduce torsion forces while moving and preserve mechanical parts from wear, friction, debris and corrosion. Lubricants are characterized by sufficient resistance to aging and oxidation, ability to eliminate solid contaminants from the lubricated environment and operate at a desired temperature. Additionally, they should not form foams and emulsions and should not attack lubricated materials, seals and bearings. This definition includes:

- oils
- greases
- solids
- gases

The following thesis is focused on lubricating oils.

Lubricating oils are classified, with regard to the place of their origin, into:

- mineral oils
- synthetic oils

Mineral oils are lubricants obtained from natural crude oils. In their production process, impurities are removed and pure hydrocarbon chains are left. The chemical structure and in that, the properties of the oil, depend strongly on the place of origin of the crude oil. Mineral oils are composed of:

- saturated aliphatic hydrocarbons
- unsaturated aliphatic hydrocarbons

- hydrocarbons with cyclic rings
- hydrocarbons with aromatic rings
- trace amounts of asphaltenes - compounds of oxygen, sulphur, phosphorus and nitrogen

The chemical stability of mineral oils depends on the relative concentrations of the above listed constituents. The most stable are *paraffinic oils* containing only saturated aliphatic hydrocarbons. Less stable are *naphtenic oils* with majority of cyclic rings, and the weakest resistive properties are exhibited by *aromatic oils* with aromatic groups contained in their hydrocarbon chains. Mineral oils, although being cheap, exhibit worse resistive properties than synthetic oils. At about 80°C a chemical degradation of mineral oils begins. Additionally, they are aggressive to most of the parts being lubricated. Therefore, they are used in applications with low loads, low pressures and low operating temperatures.

Some sample structures of paraffinic, naphtenic and aromatic oils are illustrated in Figure 2.1.

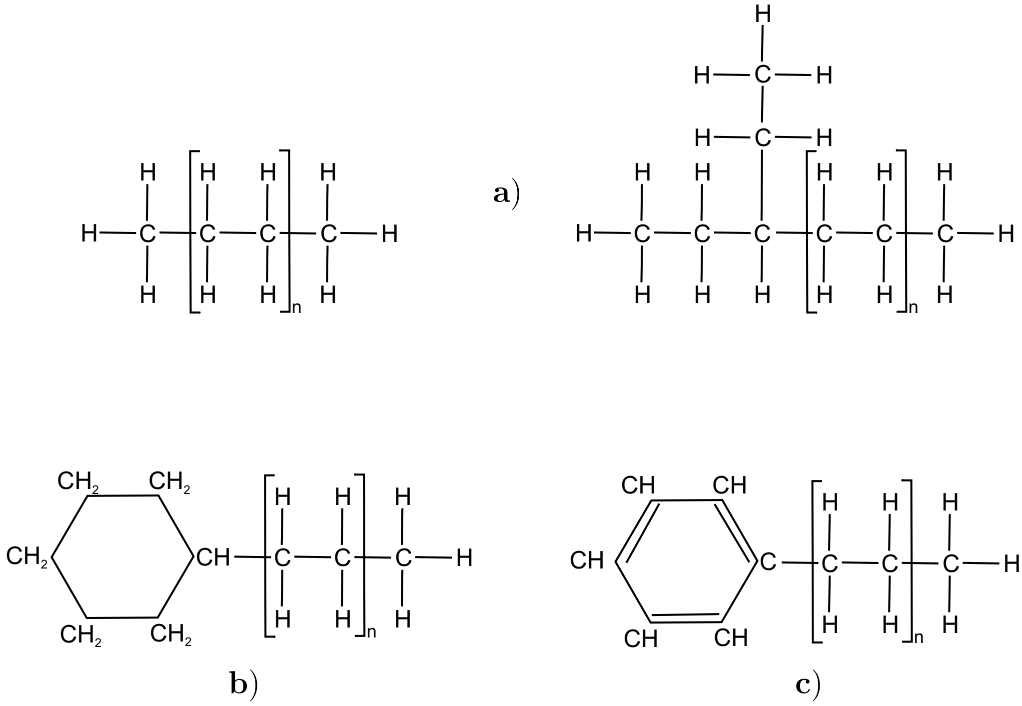

a)

b)

c)

Figure 2.1: Chain structure of hydrocarbons creating lubricants: a) paraffinic (straight and branched), b) naphtenic and c) aromatic. N ∈ (1-60).

Synthetic oils are hydrocarbons with a fully controlled chemical structure. In their production process the content of unsaturated and aromatic hydrocarbons is minimized. Thus, synthetic oils are characterized by: low variations of the viscosity with temperature, wide operating temperature ranges, the chemical stability, the aging and oxidation resistance and non-flammability [1, 2, 3, 4, 5].

The most important representatives of synthetic oils are:

- polyalphaolefins
- di-esters
- polyol-esters
- phosphate esters
- polyglycols
- ethers
- silicones

The most popular of synthetic oils are polyalphaolefins (PAO). Their structure is almost undistinguishable from the structure of mineral oils, but their molecular mass is strictly defined. They exhibit favorable low temperature characteristics. Poyalphaolefins are characterized by better chemical stability and longer life-times than mineral oils, even at elevated temperatures. A group exhibiting similar resistive and even better lubricating properties than PAOs are carboxylic esters (di-esters, polyol-esters). Phosphate esters have very good anti-wear performance, but their operating temperatures is limited to 100°C. Due to this fact, they are suitable for high-load, low-temperature applications. Polyglycols are used because of their good thermal stability, solubility in water and good low temperature behaviour. They are mostly applied in worm gears, where low torsion coefficients are required. They are, however, aggressive to most lubricated materials. Polyglycols are used in applications with temperatures up to 200°C. Finally, at temperatures exceeding 300°C, ethers are used.

Pure lubricants, both mineral and synthetic, are unable to preserve sufficient lubrication over long periods of time. In order to lengthen their use and improve, as well as introduce some new properties, special additives are used. There exists several classes of additives:

- oxidation inhibitors
- viscosity index improvers
- pour point depressants
- detergents and dispersants
- extreme pressure additives
- friction modifiers
- antifoam agents
- demulsifiers etc.

Oxidation inhibitors, (anti-oxidants), moderate the rates of oxidizing reactions mostly by reducing the concentrations of active radicals. Oxidation is the greatest danger to lubricants. An exact description of oxidation can be found in the next section. Natural anti-oxidants are sulfur and nitrogen compounds, which impair the formation of active radicals. Other substances exhibiting anti-oxidative behaviour are metal organophosphates, amines, hindered phenols, phenol derivatives, organic phosphites and organometallics.

Viscosity Index improvers, VI additives, change the viscosity-temperature (VT) characteristics of lubricants. Usually, the viscosity of lubricants varies strongly with temperature. VI improvers reduce the slope of VT plots. This is important especially for lubricants working in winter, as well as in summer. Presently, the most important VI improvers are oil-soluble linear polymer molecules, such as polyisobutenes, polyolefins and polyalkylstyrenes.

Pour point depressants are substances, which improve the flowing characteristics of oils at low temperatures. Some chemicals classified as pour point depressants are bicyclic aromatics with several alkyl chains, polymethacrylates, long chain alkyl phenols and copolymers of vinylacetate and ethylene.

Detergents and *Dispersants*, HD additives, are substances, which preserve oil-insoluble combustion and oxidation products from agglomeration. They neutralize acidic bi-products of combustion, thereby preventing corrosive wear. About 50 % of all additives used in lubricants are HD additives. HD additives are substances containing polar groups, metal ions or oleophilic aliphatic, cycloaliphatic and alkylaromatic hydrocarbon radicals. Such substances are naphthenates, stearates, sulfonates, phenates, phosphates and carbonates.

Extreme pressure (EP) and *anti-wear* (AW), additives increase the load capacity of lubricants. This class of additives consists of sulfur, chlorine, phosphorus and nitrogen compounds for example ZDDP (Zinc Diethyl Dithiophosphate) used in motor and hydraulic oils.

Friction modifiers reduce friction forces during start-up and shut-down processes by forming thin layers on friction surfaces. To the class of friction modifiers belong polar oil-soluble substances such as: fatty alcohols, amides and salts.

Antifoam agents prevent from formation of foam, which cannot provide sufficient lubrication. Antifoam agents are liquid silicones, polyethylene glycol ethers and sulfides.

Demulsifiers are anion-active compounds, which prevent from formation of water-in-oil emulsions in humid environments.

Corrosion inhibitors prevent the access of corrosive substances to metal surfaces. Corrosive substances are bi-products as lubricants or other additives such as EP additives degrade. Corrosion inhibitors are substances containing polar groups in long alkyl chains or substances reacting with metal surfaces and forming therewith protective layers. To the class of corrosion inhibitors belong nitrogen compounds, fatty acid amides, phosphoric acid derivatives, sulphonic acids, sulfur compounds, carboxylic acid derivatives and metal passivators.

A detailed description of the chemistry of lubricants, their additives and their operation can be found in [32, 33, 1, 2, 3, 4, 5].

2.2 Analysis

The chemical composition of a lubricant is specially adapted to each application, especially with regard to expected operating temperatures, speeds and loads. Due to this fact, properties of particular lubricants differ from each other and must be specified for each product separately. Such specification of a lubricant consists of:

- density - measured usually at 15°C according to DIN 51757
- viscosity - the resistance to flow. The viscosity determines the efficiency of lubrication. Usually, the viscosity of liquids decreases as the temperature increases. The viscosity is measured either as *kinematic* or as *dynamic viscosity*. Kinematic viscosity is measured at temperatures (10-150)°C, according to DIN 51561 and DIN 51562. The dynamic viscosity below 100°C is determined according to DIN 53015 and at low temperatures according to DIN 51377. From the kinematic viscosity a *viscosity index (VI)*, which defines the viscosity-temperature relationship (VT), is calculated. The better VT characteristic, the higher *VI*. *VI* is measured according to DIN ISO 2909
- refractive index - according to DIN 51423
- shear stability - a loss of viscosity with use, according to DIN 51382
- water separation test - according to DIN 51589
- emulsion forming - according to DIN 51599
- air separation characteristics - according to DIN 51381
- flash point - a temperature, at which first flash appears in the air-oil mixture, but no further burning occurs. Below 55°C flash point is measured according to DIN 51755, below 100°C - according to DIN 51758 and beyond 100°C according to DIN 51376
- cloud and pour point - a temperature, at which oil becomes cloudy or it starts flowing. Cloud point and pour point are measured according to DIN 51597 and DIN 51597, respectively
- evaporation loss - according to DIN 51581
- spectroscopical analysis - according to DIN 51384
- water content - for concentrations higher than 0,1 % measured according to DIN ISO 3733. For lower concentrations according to DIN 51777
- sulfur content - according to DIN 514000 and DIN 51364

- ash content and determination of hetero-elements - according to DIN 51575
- acidity (alkalinity) - Total Base Number (TBN) and Total Acid Number (TAN) - DIN 51558. TAN is defined as the amount of KOH (mg) required for neutralization of acidic substances contained in 1g of an oil. Similarly, TBN is the amount of an acid, expressed in mg of KOH, required for neutralization of a base contained in 1g of an oil.
- corrosiveness - according to DIN 51759, DIN 51353 and DIN 51759
- compatibility of the oil with lubricated parts
- thermal stability
- thermal conductivity
- chemical stability
- toxicity
- color - according to DIN ISO 2049
- contamination with solid particles - according to DIN 51592

In Germany, the classification of gear oils for automotive gears according to their viscosity class is defined in DIN 51512 and for industrial gears in DIN 51519. The classification according to the lubrication efficiency is contained in DIN 51517-1, DIN 51517-2, DIN 51517-3. Particular outlines for selection of an automotive gear lubricant are specified directly by producers. Outlines for proper selection of industrial lubricants are defined in DIN 51509. Some example properties of particular gear oils are collected in Table 2.1.

Properties of lubricants change with time, and eventually lubricants do not fulfill their function any more - they age. In order to determine a grade of this aging an analysis of a lubricant must be carried out. The information gained from the analysis serve to properly determine the service life of the lubricant or to detect system failures. It protects against high financial loses and damages of lubricated devices. The first visible signs of aging of the oil are: darkening, a change of the smell and usually an increase in viscosity. The analysis of used lubricants consists basically of the same tests as test conducted on fresh lubricants for their specification. The tests are conducted periodically in commercial laboratories,

Table 2.1: Typical features of example gear oils [1].

Property	**Unit**	**Manual Gear Oil**	**Hypoid Gear Oil 1**	**Industrial Gear Oil 1**	**Industrial Gear Oil 2**
Density at 15°C	g/ml	0.900	0.909	0.892	0.903
Viscosity at 40°C	mm^2/s	87.0	200	140	440
Viscosity at 100°C	mm^2/s	10.0	17.4	13	28
Viscosity Index		94	93	96	97
Pour Point	°C	-30	-24	-24	-12
Phosphorus content	mass %	0.07	0.11	0.05	0.05
Sulphated Ash	mass %	0.1	0.1	0.03	0.04

where samples must be delivered. The frequency of the laboratory analysis defines the accuracy of the exchange-time determination. The aging processes of lubricants accelerate with time and the frequency of the laboratory analysis must be therefore gradually increased. The amount of this increase is however undefined. Therefore, an optimal analysis of lubricants would be conducted on-line in lubricated devices. Such on-line analysis would have to consist of as many laboratory tests as possible, including infrared analysis to deliver information about the oxidation stage of lubricants. Presently, conduction of in-situ infrared measurements is still an unsolved problem, due to hardware limitations described in the following chapters.

As mentioned in the introduction a disposal of waste lubricants is a serious problem. Partially waste lubricants are collected in order to prevent contamination of the environment. In regions where collection of lubricants is expensive, or for some other reasons impossible, lubricants are burned. Partially aged lubricants are reconditioned or regenerated. Reconditioning is a term concerning contaminated oils, which did not lose their lubricating properties. In such cases impurities and sludge are removed by means of sedimentation, filtration, centrifugation or addition of adsorbents. Heavily contaminated and oxidized oils are regenerated. The process of regeneration consists of six stages: sedimentation, atmospheric distillation up to 250°C, sulfuric-acid treatment followed by lime neutralization, decanting with filtration, vacuum distillation and finally treatment with bleaching clay [1].

2.3 Aging Process

2.3.1 Aging in General

Aging means all changes in the composition or properties of a lubricant, regardless of the fact, whether they affect its quality or not. This definition includes contamination, chemical degradation, vaporization of components and additive depletion. Contamination originates from external and internal sources of macro- and micro-particles for example: metal, water, rust, dust or sludge. Extremely dangerous are metal particles, especially Fe and Cu, which catalyze the oxidation process. One source of metal particles are the lubricated parts themselves. External contaminants can get into a lubricating system through leaks leading to its surrounding. The chemical degradation of lubricants is identified with the oxidation process. A rate of the oxidation depends on the structure of the oil, operating temperature, load and a duration of the heat treatment. In principle, final primary products of the oxidation are acids, alcohols and water. The existence of these, cause accelerated corrosion and further oxidation. Thus, the oxidation process, once begun, cannot be stopped. The process runs differently, depending on oxidized lubricants and reaction conditions. However, its main pattern remains unchanged. In the next subsections, more detailed considerations of the oxidation process are presented [3].

2.3.2 Auto-Oxidation

Auto-oxidation is a self-accelerating oxidation occurring at moderate temperatures (<120°C). The reaction is auto-catalyzed and runs through a so called *free radical mechanism* [2]. It consists of four stages:

- initiation
- propagation
- chain branching
- termination

Initiation

In the initiation stage, the oxidation is catalyzed in the presence of oxygen and trace amounts of ions of transition metals:

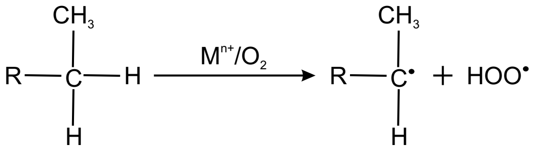

$$R-C(CH_3)(H)-H \xrightarrow{M^{n+}/O_2} R-C^{\bullet}(CH_3)(H) + HOO^{\bullet}$$

M^{n+} refers to one of the following metals: Co, Fe, V, Cr, Cu or Mn. In the above reaction an *alkyl radical* (-$C^{\bullet}RH$) is created. The rate of initiation is very slow. One place in a hydrocarbon chain, which is affected by the oxygen, depends on the structure of the hydrocarbon chain and increases in following order [2]:

$$RCH_2\text{-}H < R_2CH\text{-}H < R_3C\text{-}H < RCH{=}CH(R)HC\text{-}H < C_6H_5(R)HC\text{-}H$$

Propagation

Further, alkyl radicals react irreversibly with the oxygen, forming *alkyl peroxy radicals* :

$$R(CH_3)CH^{\bullet} + O_2 \longrightarrow R(CH_3)CH\text{-}OO^{\bullet}$$

This reaction demands a low activation energy and runs extremely fast. As next the peroxy radical abstract a hydrogen atom from another hydrocarbon chain:

$$R(CH_3)CH\text{-}OO^{\bullet} + RH \longrightarrow R(CH_3)CHOOH + R^{\bullet}$$

Peroxy radicals are not as reactive as alkyl radicals. Therefore, above and further reactions determine the rate of the whole oxidation process. Low reactivity of peroxy radicals results in relatively high concentrations of them in used lubricants. Products of the last reaction are: *hydroperoxide* and a new alkyl radical. The alkyl radical reacts again with the oxygen, as already described.

An even more favourable way of hydrogen abstraction from a hydrocarbon chain is called *intramolecular propagation*:

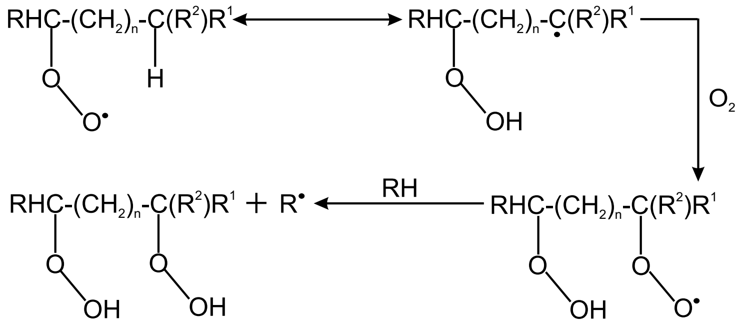

In this reaction *alkyl dihydroperoxides* are created. If the second to the last radical of the above reaction abstracts its own hydrocarbon *alkyl dihydroperoxide radicals* are created:

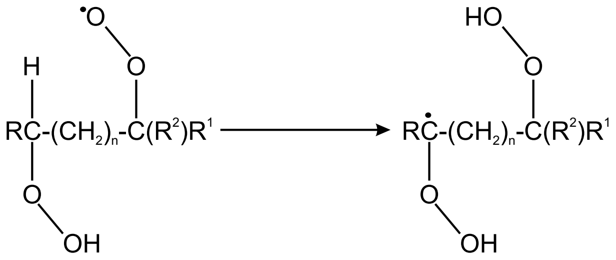

The formed alkyl dihydroperoxide radical further reacts with the oxygen. This is followed by another intramolecular hydrogen abstraction, in which *alkyl trihydroperoxide* and alkyl radical are created. To sum up, the chain propagation follows through the formation of various hydroperoxides and the degradation of the main hydrocarbon chain [2].

Chain Branching

Next comes to chain branching. If concentrations of hydroperoxides (ROOH) in the oil are low, catalysts are present and at high temperatures, *alkoxy* - (RO$^\bullet$) and *hydroxy radicals* (HO$^\bullet$) are created as follows:

$$\mathrm{ROOH} \longrightarrow \mathrm{RO}^\bullet + \mathrm{HO}^\bullet$$

These new radicals are chemically active and abstract hydrogen in the following way:

$$HO^\bullet + CH_3\text{-}R \longrightarrow H_2O + RCH_2^\bullet$$

$$HO^\bullet + R\text{-}CH_2\text{-}R^1 \longrightarrow H_2O + R(R^1)HC^\bullet$$

$$RCH_2O^\bullet + R\text{-}CH_3 \longrightarrow RCH_2OH + RH_2C^\bullet$$

Secondary and tertiary alkoxy radicals form *aldehydes* (RCHO) and *ketones* (RCOR'):

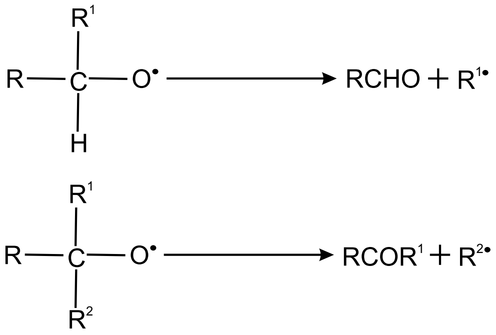

$$R\text{-}C(R^1)(H)\text{-}O^\bullet \longrightarrow RCHO + R^{1\bullet}$$

$$R\text{-}C(R^1)(R^2)\text{-}O^\bullet \longrightarrow RCOR^1 + R^{2\bullet}$$

If the concentration of hydroperoxides after the chain propagation is high enough, a *bimolecular mechanism* is preferable:

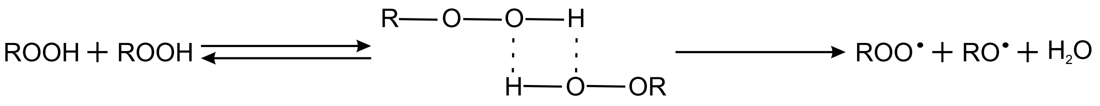

It is evident that up to this stage the concentration of hydroperoxides and active radicals initiating new chains increases [2].

Termination

Before all hydrocarbons are consumed, it comes to the termination of the oxidation. The termination follows through a combination of radicals producing unreactive species such as *ketones* (RCOR') and *alcohols* (RR'HCOH):

$$2RR^1CHOO^\bullet \longrightarrow R(R^1)CHOOOOCH(R^1)R$$

$$\longrightarrow R(R^1)C{=}O + O_2 + HO\text{-}CH(R^1)R$$

If the amount of the present oxygen is low, two other ways of the termination are possible:

$$R^\bullet + ROO^\bullet \longrightarrow ROOR$$

$$R^\bullet + R^\bullet \longrightarrow R\text{-}R$$

Generally products of the auto-oxidation are: alkylhydroperoxides, dialkylperoxides, alcohols, aldehydes, ketones, diketones, keto-aldehydes, hydroxyketones and so forth [2].

2.3.3 Oxidation at High Temperatures

At temperatures over 120°C the oxidation can be divided into a primary and a secondary phase. In the primary phase the initiation and the propagation of the radical chain reaction takes place. It follows exactly the same pattern as in the auto-oxidation, but reaction rates are higher. Additionally, organic acids (RCOOH) are created from hydroperoxy radicals:

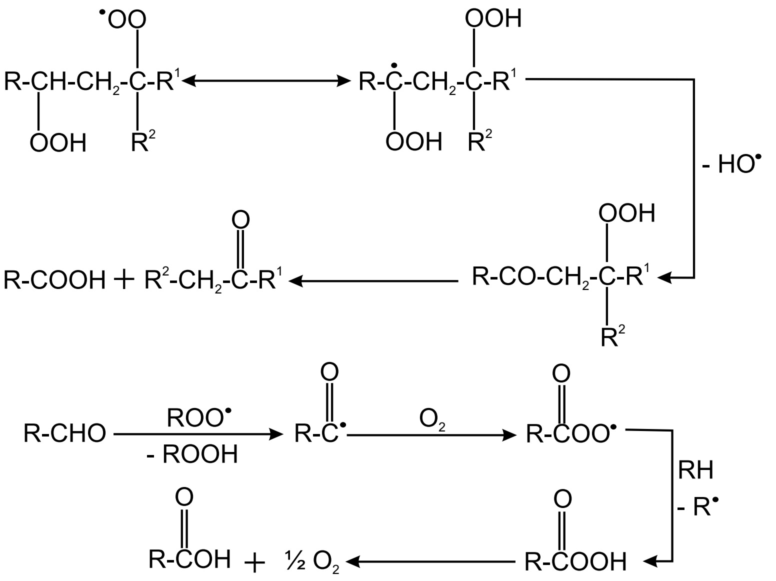

Or, as presented in the following reaction, ethers are formed:

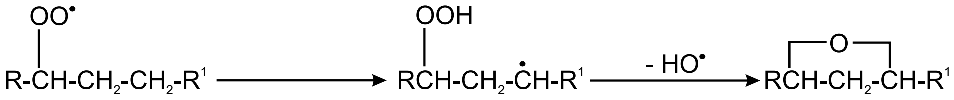

The termination follows the low temperature pattern or peroxy radicals interact giving primary and secondary *alkoxy radicals* :

$$\mathrm{2ROO^{\bullet} \longrightarrow ROOOOR \longrightarrow 2RO^{\bullet} + O_2}$$

In the secondary phase polycondensation and polymerization take place. In the reaction of polycondensation, aldehydes and ketones combine forming unsaturated aldehydes and ketones:

$$\mathrm{RCO\text{-}(CH_2)_nCHO + CH_3\text{-}COR^1 \longrightarrow RCO\text{-}(CH_2)_nCH\text{-}CHCOR^1 + H_2O}$$

Further condensation leads to high molecular weight, but still soluble products. As a result, the viscosity of the oil increases. Under these conditions the polymerization of the products of the polycondensation occurs. A product of the polymerization is an insoluble sludge. The presented overview of the oxidation process is not complete, because of its difficulty and a variety of possible reaction patterns. A more detailed description of the chemistry of above can be found in [2].

3 Infrared Spectroscopy

3.1 Infrared Spectroscopy

3.1.1 Infrared Absorption

Infrared Spectroscopy is also called *vibrational spectroscopy* due to the nature of the interaction of light with the matter. An electromagnetic wave interacts only with molecules having a natural or induced *dipole moment*. A schematic of this interaction is shown in Figure 3.2.

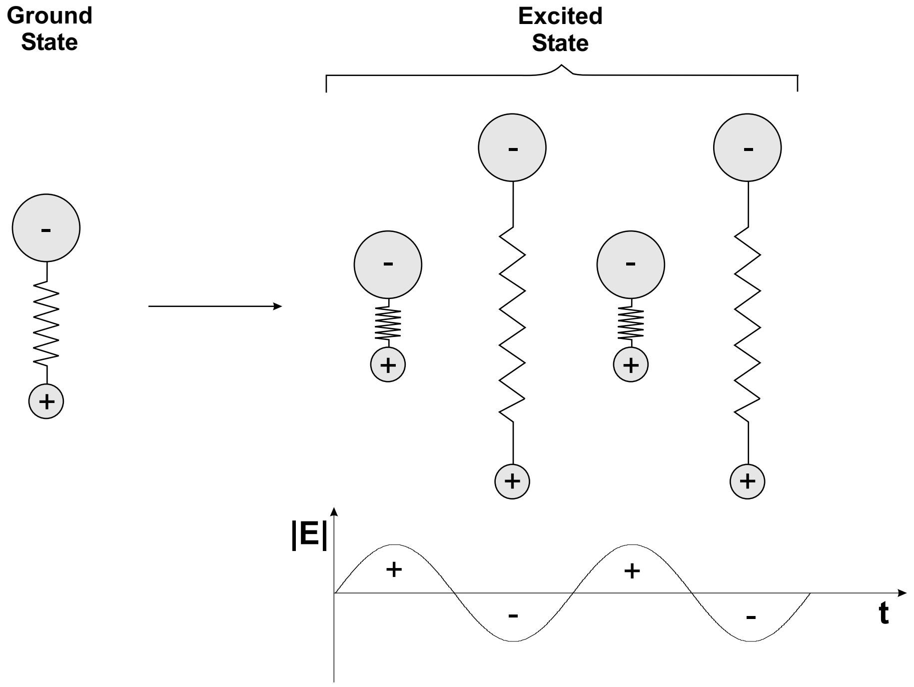

Figure 3.2: Vibrating molecule excited by the infrared radiation.

The dipole moment originates from different probabilities of finding electrons around particular atoms of a molecule. The Figure 3.2 presents the simplest case of a two atom molecule with a given spatial charge distribution. The magnitude of the dipole moment is expressed by:

$$\vec{\mu} = q\vec{r} \tag{3.1}$$

where q represents the elementary charge and r is the distance between the bonded atoms. If a molecule consists of more than two bonds, the total dipole moment is a vector sum of partial dipole moments. From Figure 3.2 it is evident that when an alternating electrical field interacts with the dipole, periodically attracting and repelling the atoms analogous to the attraction and repeal of electrical charges of the same sign, occurs. In this way a molecule begins to vibrate. The frequency of this vibration corresponds exactly the frequency of the electromagnetic wave and the energy is transferred from the light to the matter. Infrared absorption has taken place. The real change of the bond length is only of few percent of its unexcited length. The scale in Figure 3.2 is magnified for clarity. The number of possible vibrations, so called *modes* , increases with the number of atoms making up the molecule and depends on the spatial shape of the molecule. If a two atom molecule is considered, 6 degrees of freedom are necessary to describe its motion. These are: 3 - connected with the motion of the middle of the mass of the molecule, 1 - describing the vibration of the molecule along its axis and 2 - for rotations around the axes perpendicular to the molecule. The vibrational and rotational degrees of freedom of a two atom molecule are shown in Figure 3.3 [34].

In Table 3.2 expressions allowing the determination of the number of possible vibrational modes of a N-atom molecule, are listed.

Table 3.2: The number of possible vibrational modes. N represents the number of atoms making up the molecule [34].

Type of molecule	**Normal mode formula**
Linear	3N-5
Nonlinear	3N-6

Three conditions must be fulfilled in order for infrared absorption to take place. First of all, the change in the dipole moment with respect to the change in the distance between atoms can not be zero. It is expressed as:

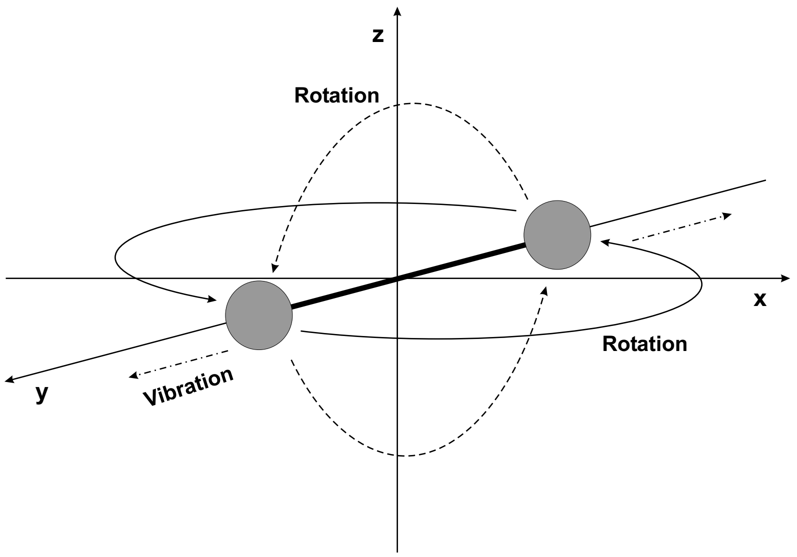

Figure 3.3: Three of six degrees of freedom of a two atom molecule: two rotational about x and z axis and one vibration along the y axis.

$$\frac{d\mu}{dx} \neq 0 \tag{3.2}$$

There exist molecules having a dipole moment, but not fulfilling the above condition, for example the symmetric stretch of a CO_2 molecule. Such molecules are either infrared inactive, or some of their modes, which do not fulfil the above condition, are not visible in an infrared spectrum. Examples of some basic infrared active modes, are depicted in Figure 3.4.

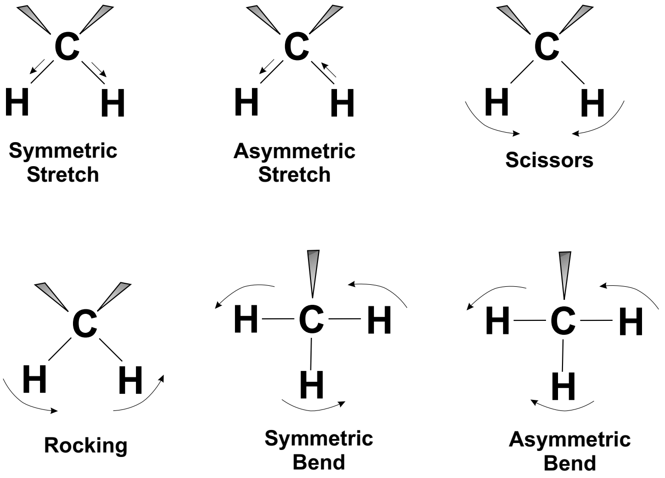

Figure 3.4: Examples of main classes of infrared induced vibrations [34, 19].

The vibrations of active molecules can be described as vibrations of a harmonic oscillator. The equation of a harmonic oscillator in classical physics results from comparison of Hook's and Newton's laws:

$$\frac{d^2x}{d^2t}m + kx = 0 \tag{3.3}$$

where k is the force constant of the spring N/cm, x is the displacement, m is the reduced mass calculated (for a two atom molecule with masses of atoms M_1 and M_2) according to:

$$m = \frac{M_1 M_2}{M_1 + M_2} \tag{3.4}$$

The approximated solution of the equation 3.3, obtained with classical methods, delivers the wavenumber $\overline{\nu}$ at which the infrared absorption takes place:

$$\overline{\nu} = \frac{1}{2\pi c}\sqrt{\frac{k}{m}} \tag{3.5}$$

The wavenumber $\overline{\nu}$ is a spectroscopic unit introduced by Rydberg in year 1880. It is defined as the reciprocal of the wavelength [34, 19, 18, 35]:

$$\overline{\nu} = \frac{1}{\lambda} \tag{3.6}$$

The problem of the harmonic oscillator can be exactly solved by means of quantum physics. For this purpose a potential in the form 3.7 has to be introduced to the Schrödinger's equation 3.8. The above potential represents the first part of the expansion of Morse's potential:

$$V = \frac{1}{2}m\omega^2 x^2 \tag{3.7}$$

$$-\frac{\hbar^2}{2m}\frac{d^2\Psi}{dx^2} + \frac{1}{2}\omega^2 x^2 \Psi = E\Psi \tag{3.8}$$

where m represents the mass of the molecule, x is the bond length, $\omega = 2\pi\nu$ is the angular frequency, $\hbar = h/2\pi$ with h Planck's constant h= $6.626{\cdot}10^{-34}$ $J \cdot s$,

Ψ represents the wave function and E are searched energy levels of the molecule. The solution of Schrödinger's equation delivers an expression for permitted energy states of the molecule, indicating therefore that the energy of the molecule is quantified. The allowed energy levels are described by an additional quantum number n, completing the set of atomic quantum numbers:

$$E_n = (n + \frac{1}{2})h\nu \tag{3.9}$$

where n = 0,1,2,... and ν the frequency of the absorbed radiation. Thus, the quantum physics shows that even in its ground state a molecule poses a rest vibrational energy equal to $E = \frac{1}{2}h\nu$. Only transitions fulfilling the condition $\Delta n = \pm1, \pm2, \pm3, ...$ or $\Delta J = \pm1, \pm2, \pm3, ...$ for rotational transitions (J - rotational quantum number) are allowed [36, 37, 35].

A plot of the classical potential energy of the harmonic oscillator with respect to the bond length and the quantified structure of its energy levels is presented in Figure 3.5. In the ground state the condition of the minimum energy defines the length of the chemical bond r_{min}.

From Figure 3.5 it is evident that the molecule can be excited to higher vibrational levels ($n \geq 1$) by energies fulfilling the condition:

$$\Delta E = E_m - E_n = h\nu \tag{3.10}$$

This excitation allows the bond to lengthen and shorten in a range limited by the potential obtained from the classical physics. Fundamental vibrational transitions (between the ground state E_0 and the first excited state E_1), of most molecules lie in the *mid-IR* (middle infrared) spectral range (400-4000) cm^{-1}. The transitions to the higher levels demand more energy. These transitions, called *overtones* are observed in the *near-IR* (near infrared) spectral range (4000-10000) cm^{-1}. Their amplitude is, however, significantly smaller than the amplitude of bands from mid-IR spectral range. It should be emphasized that the higher vibrational levels are not equally spaced. It is caused by the real anharmonic nature of vibrations, which results from the different masses of atoms making up the molecule.

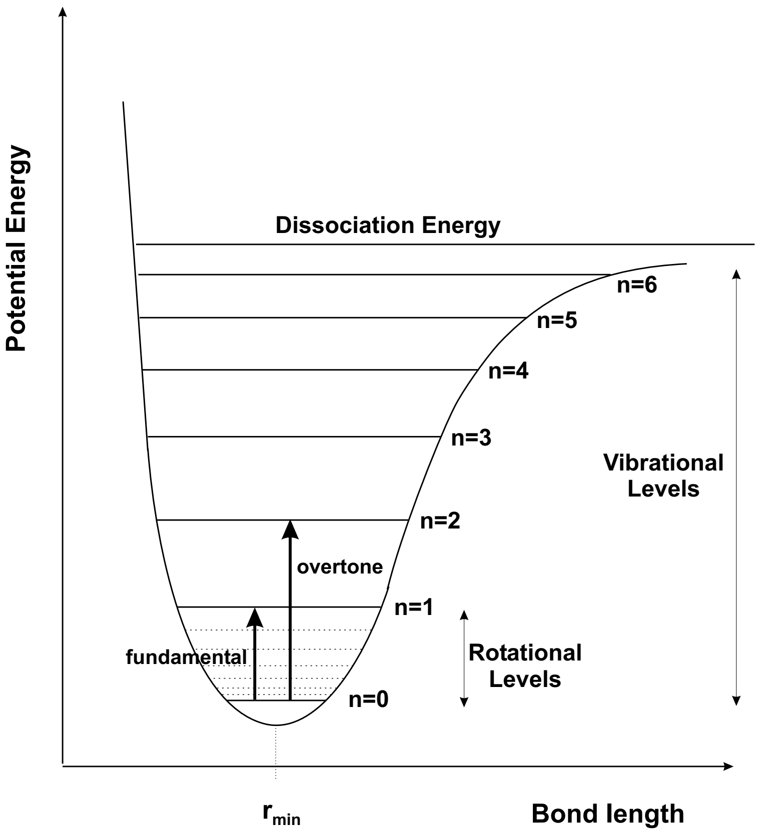

Figure 3.5: Plot of the harmonic potential of a molecule obtained from the classical solution. The quantified vibrational (—) and rotational levels (· · ·) are also marked.

This influences the amplitudes of vibrations of particular atoms. For this reason the interpretation of near-IR spectra is difficult. Between two vibrational levels rotational levels are placed. The distances between rotational levels are much smaller than those of vibrational levels and the demanded excitation energy respectively lower. It corresponds to *far-IR* (far infrared) spectral range (10-400) cm^{-1} [36].

So far, only the origin of positions of absorption peaks in an infrared spectrum has been explained. Information about the investigated substance is also included in the amplitude and the shape of absorption bands. The shape of infrared absorption bands originates from:

- natural broadening
- Doppler's broadening

- interaction with neighbours

The *natural broadening* comes from Heisenberg's Uncertainty Principle:

$$\Delta\nu = \frac{1}{2\pi\Delta t} \tag{3.11}$$

where $\Delta\nu$ is the frequency uncertainty and Δt is the time uncertainty.

The shape of the line caused only by the natural broadening is described by the Lorentzian function at the frequency ν:

$$I(\nu) = I_0 \frac{(\frac{\gamma}{4\pi})^2}{(\nu-\nu_0)^2 + (\frac{\gamma}{4\pi})^2} \tag{3.12}$$

The coefficient γ considers the radiation losses and is expressed by:

$$\gamma = \frac{2\pi q^2 \nu_0^2}{3\varepsilon_0 m c^3} \tag{3.13}$$

where q is elementary charge, ν_0 represents the frequency of the peak maximum, ε_0 is permittivity of vacuum, m is the mass and c is the speed of light. In real spectra, the natural shape of the line can be observed only in seldom cases and only at the edges of spectral lines. This is because the strong Doppler's broadening almost always covering the natural line shape.

The Doppler's broadening in infrared spectroscopy originates from thermal motions of molecules and atoms. The motions are purely random and can therefore be represented by Gaussian distribution. The resultant absorption lines are described by:

$$I(\nu) = I_0 \exp\left[-\left(2\sqrt{\ln 2}\frac{\nu_0-\nu}{\delta\nu_D}\right)^2\right] \tag{3.14}$$

with $\delta\nu_D$ - the FWHH (half width at half height) of the spectral line.

Only spectra of gases exhibit sharp absorption lines resembling theoretical Lorentzian or Gaussian functions. In reality, even their spectra are strongly dependant on the pressure broadening. Spectra of liquids and solids are generally influenced by a so called *intramolecular interaction*. Intramolecular interaction is an interaction between neighbouring molecules. An example of such is a hydrogen bond in water. This interaction causes infrared bands to be broad over a few tens of wavenumbers and impedes the identification of single absorbtion bands. On the other hand, intramolecular interaction, in a presence of variety of chemical environments, makes the identification of any substance explicit [36].

The variety of observed absorption lines are classified in so called *group wavenumbers*. The group wavenumbers are characteristic for special functional groups included in the sample, independent from the chemical composition of the rest substance. Examples of the most popular group wavenumbers and their positions in a spectrum are listed in Table 3.3.

Table 3.3: Examples of main functional groups and the corresponding wavenumbers [34, 18, 38].

Band Position, cm^{-1}	**Functional Group**
3500 - 3200	O-H or N-H
3200 - 2800	C-H
2250 - 2000	C≡ N or C≡ C
1800 - 1600	C=O
<1000	C=C and benzene rings

3.1.2 Absorption Measurement

A loss of the light intensity by passing through a sample is connected with a natural property of the matter called *absorption coefficient* α. The intensity $I(\overline{\nu})$ of the incident light decreases by an amount of $dI(\overline{\nu})$ after passing through the sample of the thickness *dx*. It is expressed by equation 3.15:

$$-dI(\overline{\nu}) = I(\overline{\nu})\alpha(\overline{\nu})dx \tag{3.15}$$

The expression $\alpha(\overline{\nu})dx$ is called the *optical depth* at the wavenumber $\overline{\nu}$. If the investigated sample is of thickness l, as depicted in Figure 3.6, than the total intensity loss, caused by passing through the sample, is calculated according to:

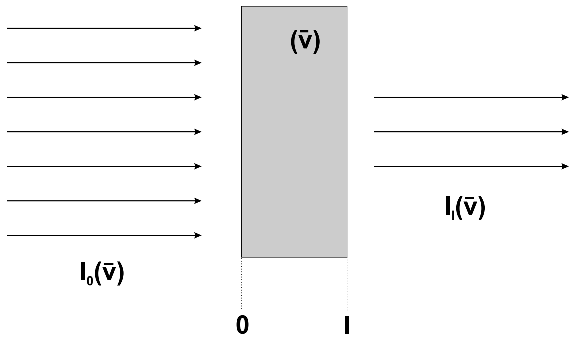

Figure 3.6: Absorption of the light on a sample of the thickness *l*.

$$-\int_0^l \frac{dI(\overline{\nu})}{I(\overline{\nu})} = \int_0^l \alpha(\overline{\nu})dx \tag{3.16}$$

The result of this integration is:

$$I_l(\overline{\nu}) = I_0(\overline{\nu})\exp[-\alpha(\overline{\nu})l] \tag{3.17}$$

The above formula is known as the *Lambert's law* of absorption and the quantity:

$$\frac{I_l(\overline{\nu})}{I_0(\overline{\nu})} = T \tag{3.18}$$

is called *Transmittance*. The unit of the Transmittance is %. The Lambert's law had already been discovered in year 1760. 100 years later, in 1852, Beer had noticed, that the above formula depends on relative concentrations of the components of the sample. He assumed that:

$$\alpha l = \alpha' cl \tag{3.19}$$

$$\ln I_l(\overline{\nu}) - \ln I_0(\overline{\nu}) = -\alpha' cl \tag{3.20}$$

where c represents the concentration of a sample. By changing from the natural to the decimal logarithm, the equation 3.20 becomes:

$$\log I_l(\overline{\nu}) - \log I_0(\overline{\nu}) = -\varepsilon cl \tag{3.21}$$

And finally, the today's well known *Lambert-Beer's* law can be written as:

$$A = \varepsilon c l \tag{3.22}$$

The new parameters ε and α' are wavenumber independent material constants, with ε representing the *molar absorptivity* of the sample [34, 20, 21, 18, 19, 35]. Consequently, the Absorbance A of a sample can be expressed as:

$$A = -\log T \tag{3.23}$$

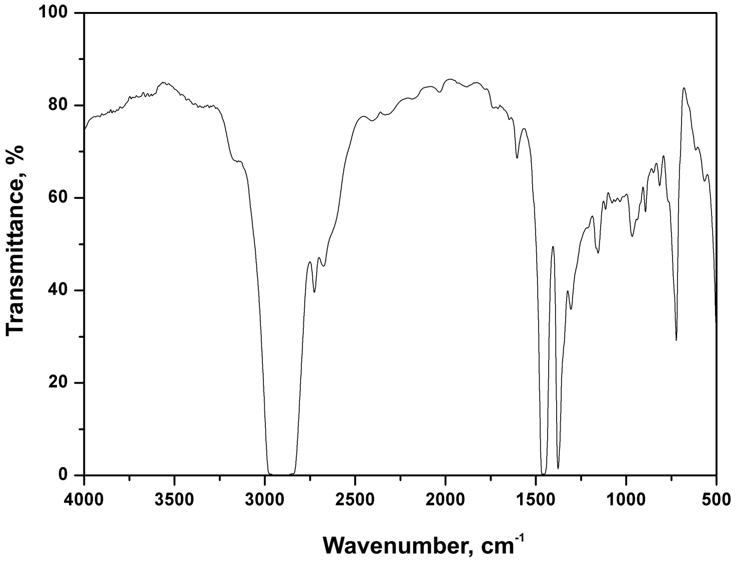

Figure 3.7: Example of a transmittance spectrum of an oil.

A measurement of an infrared transmission (absorption) follows in two steps. At first the total light intensity $I_0(\overline{\nu})$ reaching the detector, without the sample introduced into the pathlength, is measured. Next, the sample is placed between the light source and the detector and the attenuated light intensity $I_l(\overline{\nu})$ is measured. Finally, the transmittance spectrum is calculated according to 3.18. An example of an infrared transmittance spectrum is illustrated in Figure 3.7. The quality of the obtained infrared spectra is influenced by the optical and electronic components of spectrometers such as: light sources, optics and detectors. At this point, only the performance of light sources will be briefly described. Considerations of infrared detectors are presented in the next section.

In order to describe the performance of infrared light sources some basic considerations concerning light descriptions have to be made. The below mentioned definitions concern the radiometric description of light sources. The adequate photometric and photon definitions are listed in the literature [39].

A light source emits the *radiant energy* Q_e. The unit of the radiant energy is Joule J. With the radiant energy the *radiant power*, sometimes also called *radiant flux*, Φ_e in Watts W, is connected. Thus, the *spectral radiant power* $\Phi_e(\overline{\nu})$, is the wavenumber dependant radiant power:

$$\Phi_e(\overline{\nu}) = \frac{d\Phi_e}{d\overline{\nu}} \qquad , \frac{W}{cm^{-1}} \tag{3.24}$$

The *radiant exitance* or *emittance* M_e is defined as the radiant power Φ_e emitted through the surface dA:

$$M_e = \frac{d\Phi_e}{dA} \qquad , \frac{W}{m^2} \tag{3.25}$$

Similar to the spectral radiant power, the *spectral radiant emittance* $M_e(\overline{\nu})$ is obtained by a derivation of the radiant emittance M_e on the wavenumber:

$$M_e(\overline{\nu}) = \frac{dM_e}{d\overline{\nu}} \qquad , \frac{W}{m^2 cm^{-1}} \tag{3.26}$$

The *radiant intensity* I_e is the radiant power Φ_e emitted in the solid angle Ω:

$$I_e = \frac{d\Phi_e}{d\Omega} \qquad , \frac{W}{sr} \tag{3.27}$$

The *radiance* L_e of the light source is defined as the radiant emittance M_e emitted in the solid angle Ω. Thus, the radiant power Φ_e emitted through the surface dA in the solid angle Ω:

$$L_e = \frac{dM_e}{d\Omega} \qquad , \frac{W}{m^2 sr} \tag{3.28}$$

And finally, the *spectral radiance* $L_e(\overline{\nu})$ is the wavenumber dependant radiance L_e [20, 40, 41, 42, 39]:

$$L_e(\overline{\nu}) = \frac{dL_e}{d\overline{\nu}} \qquad , \frac{W}{m^2 cm^{-1} sr} \tag{3.29}$$

With the use of above definitions the emissivity of a black body can be described. The spectral distribution of the radiant energy inside of the black body with respect to the frequency ν and the temperature T is expressed by Planck's radiation law:

$$W_{e\nu}(\nu, T) = \frac{8\pi\nu^2}{c^3} \frac{h\nu}{e^{\frac{h\nu}{kT}} - 1} d\nu \tag{3.30}$$

Or with dependence on wavelengths:

$$W_{e\lambda}(\lambda, T) = \frac{8\pi hc}{\lambda^5} \frac{1}{e^{\frac{hc}{\lambda kT}} - 1} d\lambda \tag{3.31}$$

The spectral radiant exitance from a non perturbing aperture in the black body cavity, $M_{e\lambda}(\lambda, T)$ is given by:

$$M_{e\lambda}(\lambda, T) = \frac{c}{4} W_{e\lambda}(\lambda, T) \tag{3.32}$$

The corresponding spectral radiance $L_{e\lambda}(\lambda, T)$ is:

$$L_{e\lambda}(\lambda, T) = \frac{c}{4\pi} W_{e\lambda}(\lambda, T) \tag{3.33}$$

For the needs of spectroscopy, it is convenient to express the above equation dependant on wavenumbers. Thus:

$$L_{e\overline{\nu}}(\overline{\nu}, T) = 2hc^2\overline{\nu}^3 \frac{1}{e^{\frac{hc\overline{\nu}}{kT}} - 1} d\overline{\nu} \tag{3.34}$$

Integrating the spectral radiant exitance over all wavelengths gives:

$$\int M_{e\lambda}(\lambda, T) d\lambda = \sigma T^4 \tag{3.35}$$

The above formula is known as the *Stefan-Boltzmann law*. The constant σ is equal to $5.67 \cdot 10^{-8}\ W/m^2K^4$. The plots of spectral radiances of the black body at different temperatures, are depicted in Figure 3.8 [20, 43, 42, 44, 39].

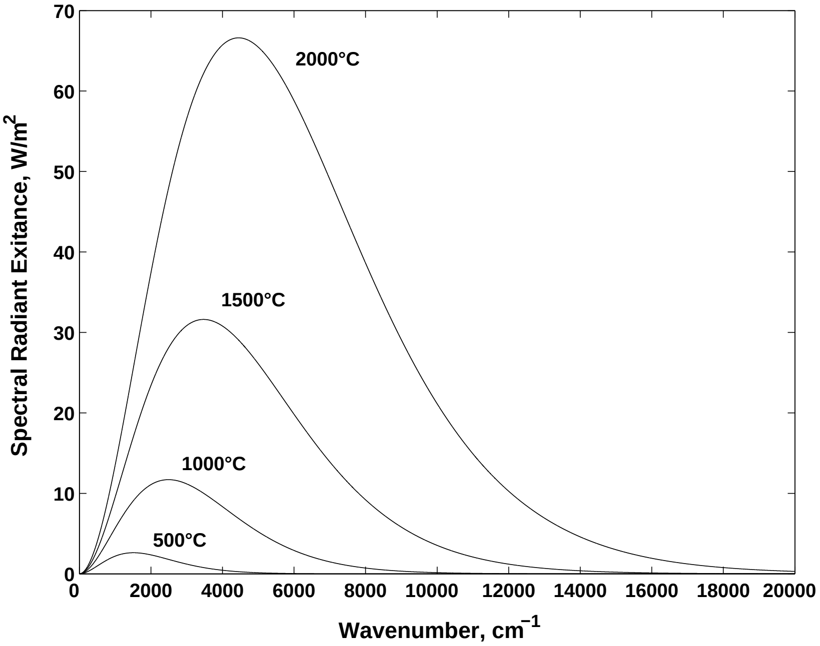

Figure 3.8: Spectral radiant exitances of four black bodies of different temperatures: 2000°C, 1500°C, 1000°C and 500°C.

From Figure 3.8 it is evident that with increasing temperature the peaks of spectral radiant exitance move towards higher wavenumbers. This phenomenon is known as the *Wien's displacement law*, which is mostly presented in the dependance on wavelengths:

$$\lambda_{max} = \frac{B}{T} \tag{3.36}$$

The constant B is equal to 2898, if λ and T are expressed in micrometers and Kelvins respectively.

Real light sources only resemble the performance of the ideal black body. The rate of this similarity is described by a parameter called *emissivity* $\varepsilon(\lambda, T)$ [39]:

$$\varepsilon(\lambda, T) = \frac{M_{e\lambda}(\lambda, T)_{real}}{M_{e\lambda}(\lambda, T)_{bb}} \tag{3.37}$$

Light sources used in infrared spectroscopy are mostly glowing ceramic lamps working at temperatures exceeding 1000°C. This provides sufficient radiant energy, higher than the background radiation, in the whole infrared spectral range. Sizes of infrared light sources range from a few millimeters to a few tens of centimeters. In cases of large, hot sources used in sophisticated spectrometers, a special cooling of the source body is required. In sensor applications, small infrared light sources without cooling and temperatures not exceeding few hundreds degrees Celsius are used.

It was already mentioned, that for transmission measurements a light source, a sample and a detector are sufficient. Such a system determines the transmission for monochromatic light sources. If used with broad-band light sources, the system would not deliver any spectral resolution. The resolution of wavenumbers is obtained by applying of prisms, gratings or, as in this work presented, Michelson-Interferometers, before the sample compartment. The spectrometer with an implemented Michelson-Interferometer is called an FTIR (Fourier Transform Infrared Spectrometer). A schematic of which is depicted in Figure 3.9. In the next section the exact description of its optical bench is presented [18, 45, 46, 47, 35].

3.2 Fourier Transform Infrared Spectroscopy

3.2.1 Michelson Interferometer

Infrared Spectroscopy is a measurement technique existing since the 1930's. The first commercially available infrared spectrometers were dispersive spectrometers, in which the light coming from a broad band source is split into separate wavelengths through a grating or a prism. Spectral resolution of such spectrometers is limited by the grating constant. Another disadvantage of dispersive spectrometers is the duration of the measurement. The scanning of the whole spectral

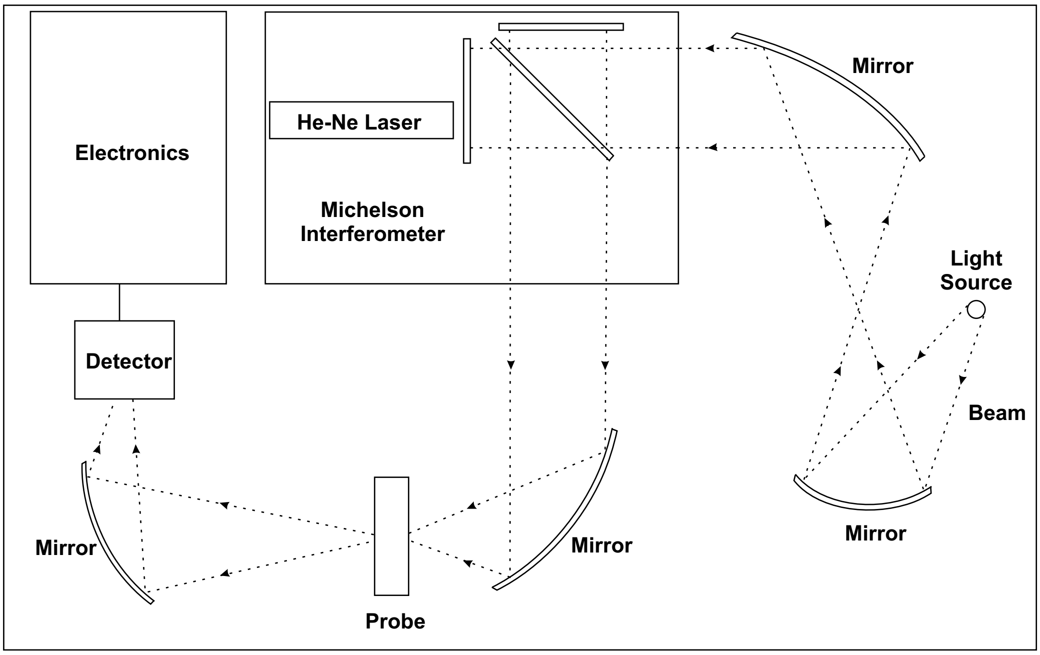

Figure 3.9: Schematic of the FTIR spectrometer, Bruker IFS-66.

range is obtained by changing the position of the detector or the prism. Thus, the collection of the whole spectrum requires a relatively long time. A turning point for infrared spectroscopy was the development of the Fourier Transform Infrared Spectrometer (FTIR), in which the spectral resolution is obtained through modulation of the light, occurring in the Michelson-Interferometer. In this way the information about the whole spectrum is collected within one measurement. However, a further Inverse Fourier Transform of the collected signal is necessary. For years this calculation represented the most serious problem of the FTIR measurement. The discovery of Fast Fourier Transform algorithm, by Cooley and Tukey in 1964, has changed this situation. Presently, FTIR spectroscopy is a well established method of chemical analysis. The world-wide known manufacturers of FTIR spectrometers are: Perkin-Elmer, Thermo-Nicolet, Bomem, Bruker etc.. The measurements presented in this thesis were made with two FTIR spectrometers, therefore the theory of FTIR spectroscopy is closer explained below [20, 21, 35, 47].

The heart of a Fourier Transform Infrared Spectrometer is the Michelson-Interferometer. The structure of the Michelson-Interferometer is illustrated in

Figure 3.10. If a monochromatic light source of infinitely narrow, perfectly collimated beam of the wavelength λ_0 is considered, the electrical part of the emitted electromagnetic wave is defined through:

$$\vec{E} = \vec{E}_0 \exp\left[j(\vec{k} \cdot \vec{x} - \omega t)\right] \tag{3.38}$$

where k represents a *wavevector* defined as $k = 2\pi/\lambda_0$. The Intensity I of this electromagnetic wave is defined as the time average of the Poynting's Vector S [48] defined as:

$$S = \frac{1}{\mu_0}|\vec{E} \times \vec{B}| \tag{3.39}$$

The light intensity I is therefore equal to:

$$I = \langle S \rangle = \frac{c\varepsilon_0}{2} E_0^2 \tag{3.40}$$

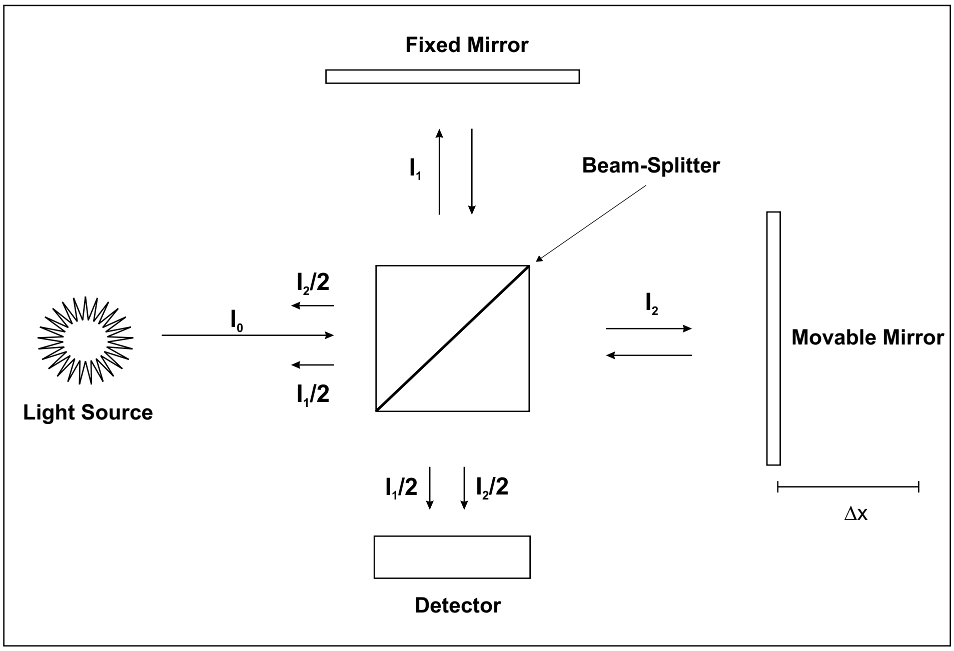

Figure 3.10: Structure of the Michelson-Interferometer with the beam-splitter of 50 % efficiency.

In Figure 3.10, the emitted light of intensity $I_0(\lambda_0)$ is directed to the beam-splitter. In the beam-splitter the light undergoes splitting into two perpendicular beams $I_1(\lambda_0)$ and $I_2(\lambda_0)$. Each of the resultant beams has the same light intensity, being the half of the initial source intensity:

$$I_1(\lambda_0) = I_2(\lambda_0) = \frac{1}{2} I_0(\lambda_0) \tag{3.41}$$

One of the beams travels to the fixed mirror, where it is reflected and directed back to the beam-splitter. The same happens with the second beam and the movable mirror. The shift of the movable mirror Δx, introduces phase differences equal to $(2k\Delta x)$, between the beams $I_1(\lambda_0)$ and $I_2(\lambda_0)$. The reflected beams meet again at the beam-splitter, where they undergo the second splitting. Thus, the resultant light intensity measured at the detector originates from the interference of the doubly splitted incident beam. This is described by:

$$\vec{E}_{total} = \vec{E}_{01} \exp\left[j(\vec{k}\cdot\vec{x} - \omega t)\right] + \vec{E}_{02} \exp\left[j(\vec{k}\cdot(\vec{x} + 2\Delta\vec{x}) - \omega t)\right] \tag{3.42}$$

where indices *01* and *02* describe first and second interfering electromagnetic wave of which $I_{01} = I_{02} = I_1/2 = I_0/4$. The *optical path difference* (OPD) equal to $2\Delta x$, between the beams $I_1(\lambda_0)$ and $I_2(\lambda_0)$, is called the *retardation* and usually denoted by the symbol δ. Conditions for constructive interference at the detector are fulfilled if $\delta = n\lambda$, for n = 0,1,2,.... On the contrary, if $\delta = (n + \frac{1}{2}\lambda)$ the interference is completely destructive. The intensity measured at the detector depends therefore from the phase shift introduced through the movable mirror [17].

As mentioned in subsection 3.1.1, the spectroscopic units are wavenumbers $\overline{\nu}$. Therefore, the light intensity measured at the detector I_D calculated from 3.42 is expressed by:

$$\begin{aligned} I_D(\delta) &= \frac{1}{2} I_0(\lambda_0)\{1 + \cos(2\pi\frac{\delta}{\lambda_0})\} \\ &= \frac{1}{2} I_0(\overline{\nu}_0)\{1 + \cos(2\pi\delta\overline{\nu}_0)\} \end{aligned} \tag{3.43}$$

It is now evident that the signal at the detector consists of a DC component equal to the half of the initial intensity $I_0(\nu_0)$ and an AC component equal to:

$$I(\delta) = \frac{1}{2} I_0(\overline{\nu}_0)\cos(2\pi\delta\overline{\nu}_0) \tag{3.44}$$

It is this AC component, which is usually called the *interferogram* $I(\delta)$. In practice the measured signal is influenced by a variety of parameters introducing deviations from this ideally cosinusoidal pattern. Sources of these deviations are: a) non-ideal transmission efficiency of the beam splitter, b) non-uniform spectral response of infrared detectors, c) wavenumber dependant response of electronic circuits and filters. These influences are constant within a measurement and can be therefore described by an additional function $H(\overline{\nu}_0)$. Using the notation:

$$B(\overline{\nu}_0) = \frac{1}{2} H(\overline{\nu}_0) I_0(\overline{\nu}_0) \tag{3.45}$$

the interferogram of a monochromatic light can be written as:

$$I(\delta) = B(\overline{\nu}_0)\cos(2\pi\delta\overline{\nu}_0) \tag{3.46}$$

So far, a monochromatic light source has been considered. In case of polychromatic light sources, such as used in infrared spectrometers, the interferogram contains decoded information about all wavenumbers. It is expressed by the integration of the monochromatic interferogram over all wavenumbers:

$$I(\delta) = \int_{-\infty}^{+\infty} B(\overline{\nu})\cos(2\pi\delta\overline{\nu})d\overline{\nu} \tag{3.47}$$

The quantity $B(\overline{\nu})$ is the spectrum of the light source. The interferogram, according to the above formula, is from a mathematical point of view a Cosine Fourier Transform of $B(\overline{\nu})$. Thus, a signal at the detector is a function of the retardation instead of the wavenumber. In order to get the spectral representation of results, the Inverse Fourier Transform of the interferogram has to be calculated.

$$B(\overline{\nu}) \circ \overset{\mathcal{F}}{-} \bullet\, I(\delta) \tag{3.48}$$

$$I(\delta) \bullet \overset{\mathcal{F}^{-1}}{-} \circ\, B(\overline{\nu}) \tag{3.49}$$

The Inverse Fourier Transform of 3.47 is:

$$B(\overline{\nu}) = \int_{-\infty}^{+\infty} I(\delta)\cos(2\pi\delta\overline{\nu})d\delta \tag{3.50}$$

The performance of Michelson Interferometer is precisely explained in [17, 18, 49, 50, 51, 52, 44, 53, 46, 54]. In Figure 3.11 an example of a real interferogram $I(\delta)$ and the corresponding spectrum $B(\overline{\nu})$ of a polychromatic light source, measured with an FTIR spectrometer is shown.

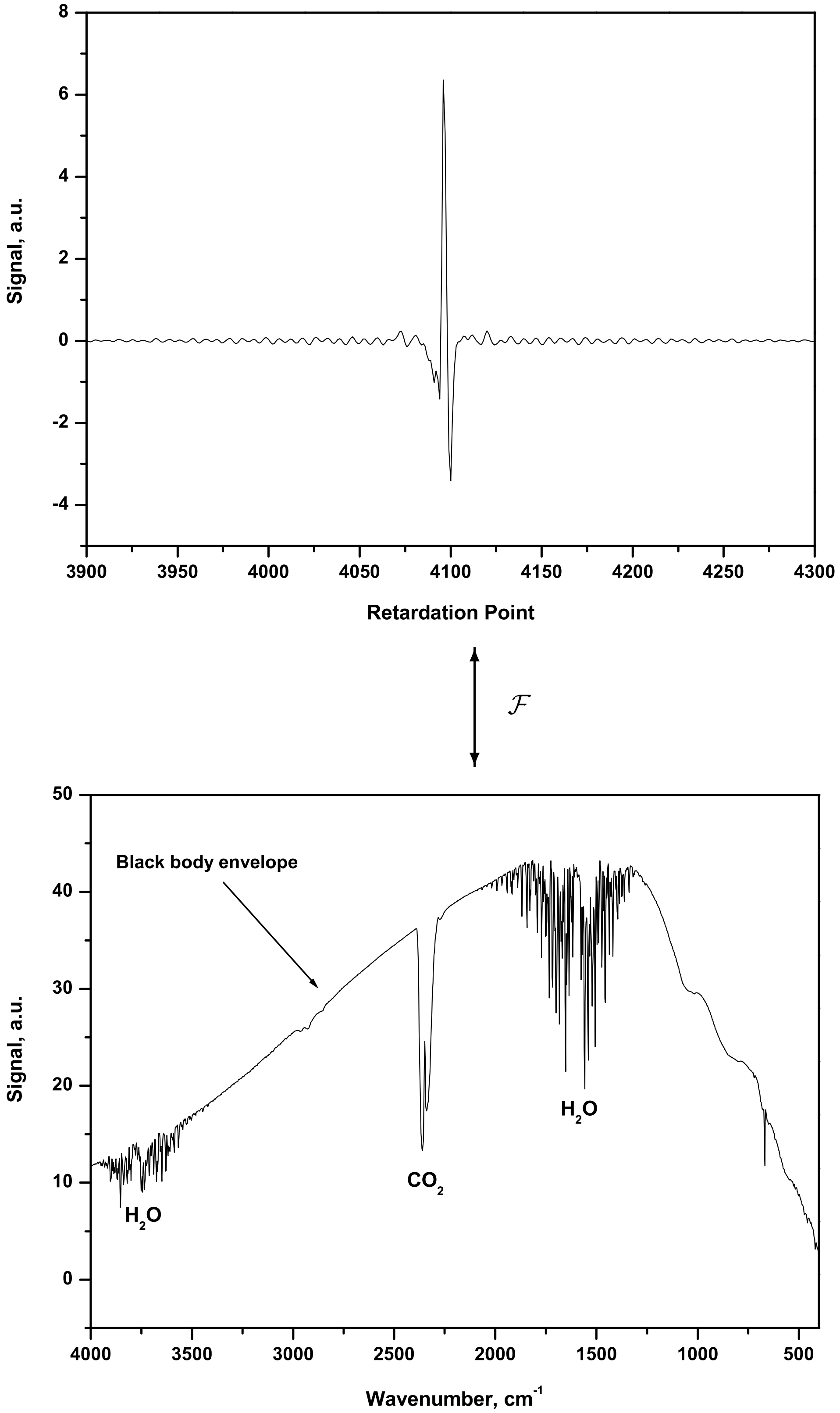

Figure 3.11: Above a real interferogram measured with 32 scans at 4 cm^{-1} resolution. Beneath the spectrum being a Fourier Transform of the upper Interferogram. The shape of the spectrum originates from the black body. Particular absorption lines of air constituents (H_2O, CO_2) are visible.

3.2.2 Spectral Resolution

The integration limits in equation 3.50 indicate an infinite shift of the movable mirror of the Michelson Interferometer. It results in the infinite spectral resolution of the spectrum $B(\overline{\nu})$. In practice the retardation δ is limited. This limitation influences the obtainable spectral resolution. In the first approximation, the resolution of the FTIR spectrometer can be expressed as:

$$\Delta\overline{\nu} = \frac{1}{\Delta_{max}} \tag{3.51}$$

The Δ_{max} is a maximum retardation obtainable during the measurement. A detailed description of the resolution requires, however, consideration of an *Instrument Line Shape Function* (ILS). The ILS describes the broadening of a monochromatic spectral line recorded with a spectrometer, caused by two factors: the limited retardation and the extended size of the light source. A consideration of the finite retardation can be expressed through $D_1(\overline{\nu})$ function, being a Fourier Transform of a boxcar function $d_1(\delta)$:

$$d_1(\delta) = \begin{cases} 1 & : \quad -\Delta_{max} \leq \delta \leq +\Delta_{max} \\ 0 & : \quad \delta > |\Delta_{max}| \end{cases} \tag{3.52}$$

The Fourier Transform $D_1(\overline{\nu})$ of the $d_1(\delta)$ is a sine-function:

$$D_1(\overline{\nu}) = 2\Delta_{max}\frac{\sin(2\pi\overline{\nu}\Delta_{max})}{2\pi\overline{\nu}\Delta_{max}} \tag{3.53}$$

The second part of the ILS function originates from an extended size of a light source and can be, under condition of an uniform illumination, relatively well approximated by:

$$D_2(\overline{\nu}) = \begin{cases} \frac{1}{\Delta\overline{\nu}_i} & : \quad \Delta\overline{\nu}_i \leq \overline{\nu} \leq 0 \\ 0 & : \quad beyond \quad this \quad range \end{cases} \tag{3.54}$$

It is a boxcar function of the width of $\Delta\overline{\nu}_i$ and the hight of $1/\Delta\overline{\nu}_i$. The parameter $\Delta\overline{\nu}_i$ is defined by the diameter d_F of the light source or the collimating aperture. If the focus length of the aperture is *f*, then:

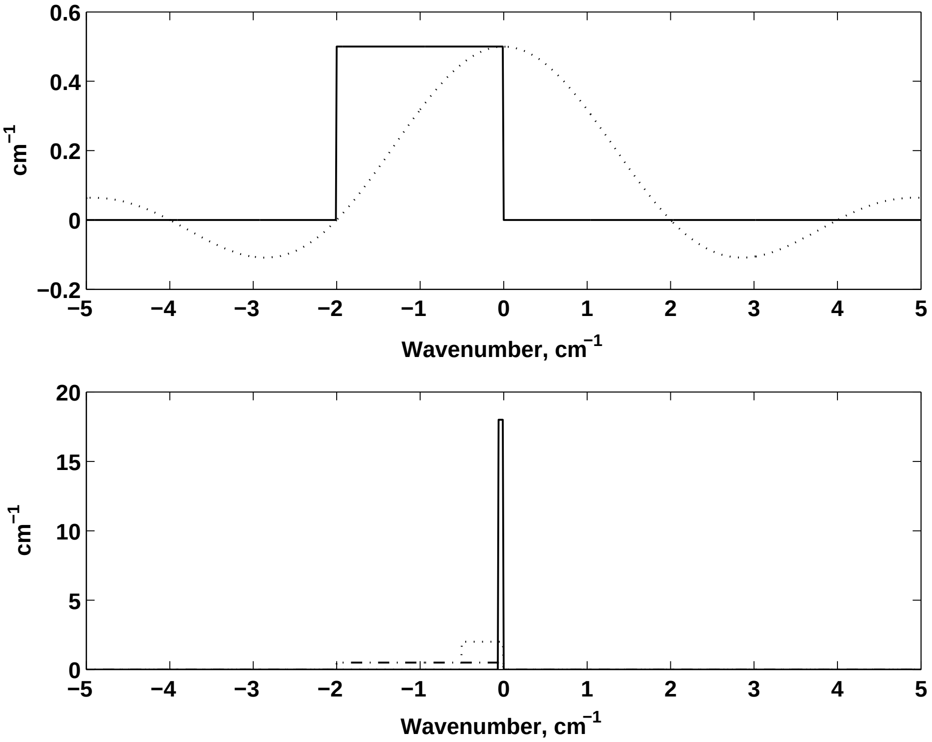

Figure 3.12: Upper figure shows simulated partial functions creating an ILS. The $D_1(\overline{\nu})$ function $(\cdots)$ was calculated for $\Delta_{max} = 2.5$ mm and the diameter of the aperture 12 mm. Lower figure presents the $D_2(\overline{\nu})$ function calculated for different diameters of the aperture: $(- \cdot -)$ 12 mm, $(\cdots)$ 6 mm and (—) 2 mm. A significant narrowing of the $D_2(\overline{\nu})$ function with the decreasing diameter of the apertures is evident. The narrowing improves the spectral resolution of the measurement. All calculations conducted for f = 150 mm and $\overline{\nu}_i = 2500 \ cm^{-1}$.

$$\Delta\overline{\nu}_i = \left(\frac{d_F}{2f}\right)^2 \frac{\overline{\nu}_i}{2} \tag{3.55}$$

The final ILS function is a convolution of the $D_1(\overline{\nu})$ and $D_2(\overline{\nu})$.

$$D(\overline{\nu}) = D_1(\overline{\nu}) * D_2(\overline{\nu}) \tag{3.56}$$

Plots of simulated partial functions $D_1(\overline{\nu})$ and $D_2(\overline{\nu})$ are depicted in Figure 3.12.

With the use of the ILS function the real spectrum $G(\overline{\nu})$ can be written in a form of:

$$G(\overline{\nu}) = \int_{-\infty}^{+\infty} I(\delta) d(\delta) \cos(2\pi\delta\overline{\nu}) d\delta \tag{3.57}$$

where $d = d_1 \cdot d_2$ according to Fourier Theorem. The Fourier Transform of a product of two functions is a convolution of Fourier Transforms of these functions. Therefore, the real spectrum $G(\overline{\nu})$ is calculated as the convolution of the ideal spectrum $B(\overline{\nu})$ and the ILS function:

$$\begin{aligned} G(\overline{\nu}) &= B(\overline{\nu}) * D(\overline{\nu}) \\ &= \int_{-\infty}^{+\infty} B(\overline{\nu}')D(\overline{\nu} - \overline{\nu}')d\overline{\nu}' \end{aligned} \tag{3.58}$$

The obtained spectrum behaves still as a sine-function. It intersects the x axis at $\overline{\nu}_i - (1/2\Delta_{max})$ and $\overline{\nu}_i + (1/2\Delta_{max})$. Thus, it is evident that two lines lying at the distance of $1/\Delta_{max}$ will be completely separated. It has to be emphasized that two monochromatic lines lying closer each other than $1/\Delta_{max}$ will also be identified. Therefore, the real spectral resolution of FTIR spectrometers is always better than this according to the definition 3.51. Two lines are hold for resolved, if the decrease of the intensity between the two maxima exceeds 20 % of the maximum peak intensity. This condition is fulfilled for sine-functions for a distance of $0.73/\Delta_{max}$ [17, 55]. It should be also underlined that according to equation 3.55 high spectral resolution of FTIR measurements demands small collimating apertures.

3.2.3 Apodisation

The pure ILS function poses quite strong side lobes, as depicted in Figure 3.13, influencing the shape, the position and the amplitude of measured spectral lines and therewith limiting the spectral resolution. This phenomenon is explained on example curves plotted in Figure 3.14.

In order to improve the spectral resolution a so called *apodisation* is conducted. In this process the infinite interferogram in equation 3.50 is limited by some other functions instead of, as so far considered, a boxcar function $d_1(\delta)$. The

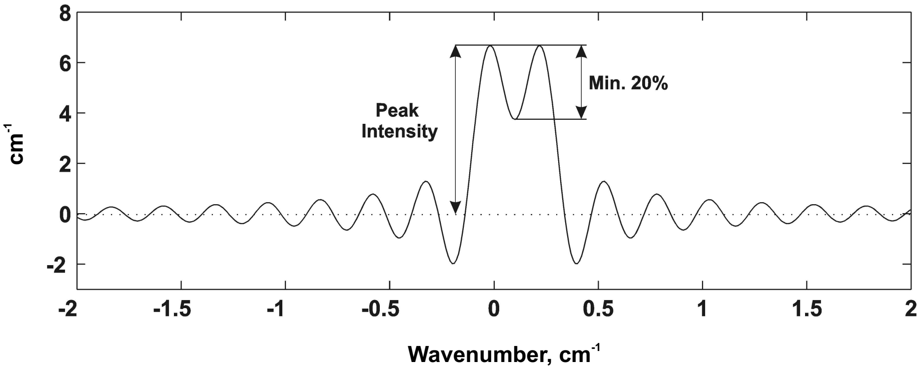

Figure 3.13: Two covering spectral lines lying at the limit of the spectral resolution. The curves were simulated with f = 150 mm and $\Delta_{max} = 4$ cm^{-1}.

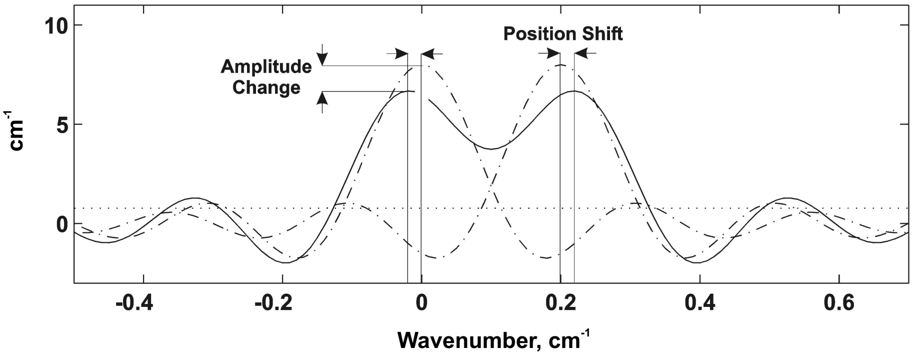

Figure 3.14: Two covering spectral lines (— · —), and the resultant spectrum (—). The differences in amplitudes and peak positions caused by side lobes of ILS functions are visible. Simulations conducted for f = 150 mm and $\Delta_{max} = 4$ cm^{-1}.

Table 3.4: Most Popular Apodisation Functions [17, 55].

Apodisation Function		**ILS**		
Name	**Formula**	**FWHH**	**Resolution**	**Peak Height**
Boxcar	1	$0.605/\Delta_{max}$	$0.68/\Delta_{max}$	2.0
Triangular	$1-\left\lvert\frac{\delta}{\Delta_{max}}\right\rvert$	$0.88/\Delta_{max}$	$0.88/\Delta_{max}$	1.0
Norton-Beer	$\sum C_i\left[1-\left(\frac{\delta}{\Delta_{max}}\right)^2\right]^i$			
- weak	$C_0 = 0.348093$	$C_1 = -0.0876$	$C_2 = 0.7035$	$C_3 = 0$
- medium	$C_0 = 0.152442$	$C_1 = -0.1362$	$C_2 = 0.9837$	$C_3 = 0$
- strong	$C_0 = 0.045335$	$C_1 = 0$	$C_2 = 0.5549$	$C_3 = 0.4$
Happ-Genzel	$0.54 + 0.46\cos\left(\frac{\pi\delta}{\Delta_{max}}\right)$	$0.91/\Delta_{max}$	$0.89/\Delta_{max}$	1.08

apodisation reduces the amplitudes of the side lobes, but causes the broadening of spectral lines. It has to be emphasized that, since apodisation influences the spectral line, in case of measurements of a high resolution, weak absorption bands or a high quantitative accuracy, a proper choice of the apodisation function is crucial for obtaining of accurate results. Most often recommended functions are Norton-Beer medium and strong apodisation functions. Some examples of the most popular apodisation functions are collected in Table 3.4.

The spectral resolution is also influenced by the divergence of beams passing through the Michelson-Interferometer. The divergent beam produces a ring pattern with alternating minima and maxima at the detector plane. This pattern originates from the phase differences introduced by the path differences between the central and edge beams, as illustrated in Figure 3.15. At the zero retardation point, in the middle of the detector plane, a maximum occurs. If the retardation is increased the rings wonder from each other. If one defines x as the path difference between the central and the external ray, then at the point of $x = \lambda/2$ the beams are out of phase. At this point the fringe contrast at the detector disappears. Therefore, the retardation at which x reaches the value $x = \lambda/2$ gives the maximum obtainable spectral resolution of an FTIR spectrometer. Thus, the maximum half-angle, which can be passed through the interferometer by collecting of a spectrum of the resolution $\Delta\overline{\nu}$ and the maximum wavenumber $\overline{\nu}_{max}$ is [17, 55]:

$$\alpha_{max} = \sqrt{\left(\frac{\Delta\overline{\nu}}{\overline{\nu}_{max}}\right)} \tag{3.59}$$

The maximum tolerated solid angle is:

$$\Omega_{max} = 2\pi\frac{\Delta\overline{\nu}}{\overline{\nu}_{max}} \tag{3.60}$$

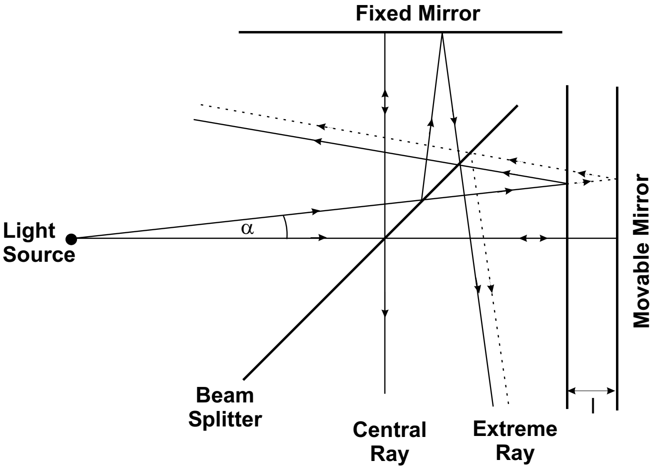

Figure 3.15: Divergent beam passing through the Michelson-Interferometer [17].

3.2.4 Phase Correction

Additional factors, which have to be considered in FTIR measurements are influences of the optics, the electronics or sampling effects on the interferogram. These introduce an additional phase shift of $\theta_{\overline{\nu}}$ to the interferogram and therewith an additional noise to the spectrum:

$$I(\delta) = \int_{-\infty}^{+\infty} B(\overline{\nu})\cos(2\pi\delta\overline{\nu} - \theta_{\overline{\nu}})d\overline{\nu} \tag{3.61}$$

By the extension of the cosine term in equation 3.61 the interferogram can be written in a complex form:

$$I(\delta) = \int_{-\infty}^{+\infty} B(\overline{\nu}) \exp\left[-j\left(2\pi\delta\overline{\nu} - \theta_{\overline{\nu}}\right)\right] d\overline{\nu} \tag{3.62}$$

The real part of this expression is the interferogram. The additional phase reveals in the imaginary part. The process of removal of the imaginary part is called *phase correction*. The most popular method of phase correction was developed by Mertz. In this method the low resolution Cosine (C) and Sine (S) Fourier Transforms of the interferogram are first calculated. Next, the phase angle $\theta_{\overline{\nu}}$ at each wavelength of the measured spectrum is calculated according to:

$$\theta_{\overline{\nu}} = \arctan\left(\frac{Im(C(\overline{\nu}))}{Re(S(\overline{\nu}))}\right) \tag{3.63}$$

With the use of the found $\theta_{\overline{\nu}}$, the corrected spectrum is calculated from Cosine or Sine Fourier Transform, for example [55]:

$$B(\overline{\nu}) = \frac{C(\overline{\nu})}{\sin\theta_{\overline{\nu}}} \tag{3.64}$$

More exact considerations of phase correction methods are contained in [17, 56, 57, 55].

3.2.5 Sampling and Signal to Noise Ratio

The collected interferogram is sampled with a frequency fulfilling the *Nyquist's Criterion*, which in case of the interferogram means:

$$\frac{1}{\Delta x} \leq 2\overline{\nu}_{max} \tag{3.65}$$

where $\overline{\nu}_{max}$ represents the maximum measured wavenumber for the spectral range $(0{-}\overline{\nu}_{max})$ and Δx is the sampling interval. If this criterion is not fulfilled, artificial spectral features appear in the spectrum. This phenomenon is known as *aliasing* or *folding*, which means that frequencies occurring at $(\overline{\nu}_{max} + \overline{\nu}_1)$ appear in the spectrum at $(\overline{\nu}_{max} - \overline{\nu}_1)$. Therefore, additional optical and electronic filters are applied, in order to limit the frequency bandwidth to the wanted $(\overline{\nu}_{max} - \overline{\nu}_{min})$. For limited spectral range $(\overline{\nu}_{max} - \overline{\nu}_{min})$, Δx is defined by the minimum and the maximum measured wavenumber according to:

$$\Delta x = \frac{1}{2(\overline{\nu}_{max} - \overline{\nu}_{min})} \tag{3.66}$$

The number of collected data points remains in this case unchanged, but the number of data points to be computed N_S, is thus reduced to:

$$N_S = \frac{\Delta_{max}}{\Delta x} = \frac{2(\overline{\nu}_{max} - \overline{\nu}_{min})}{\Delta \overline{\nu}} \tag{3.67}$$

with $\Delta \overline{\nu}$ being the spectral resolution. Due to the possible deviations from the constant mirror velocity, the sampling is conducted at equal retardation intervals Δx instead of equal time intervals Δt. Equal retardation intervals are obtained from an additional interferogram collected by the use of a He-Ne laser coupled to the Michelson-Interferometer. Sampling takes place for example at zeros of the He-Ne interferogram.

The *Dynamic range* of an FTIR spectrometer is defined as a ratio of the signal collected at the zero retardation (maximum of the interferogram) to the r.m.s. (root-mean-square) noise level. Typical values are in order of 10^4. Thus, for appropriate signal analysis at least 16 bit ADCs are required.

The *Signal to Noise Ratio* (SNR) is a parameter describing the quality of the measured spectra. It is defined as the ratio of the gained signal power to the noise power. The measured light power is expressed by Planck's equation 3.32. It is limited by the *throughput* Θ_D of the system. The throughput is a product of the area of the beam with its solid angle at any focus. In case of low resolved measurements the throughput Θ_D is limited by the acceptance angle Ω_D of the used detector and its area A_D.

$$\Theta_D = A_D \Omega_D \tag{3.68}$$

Therefore, the power P received at the detector, calculated in a unit wavenumber interval with efficiency ξ, can be expressed by:

$$P = M_e(\overline{\nu}, T)\Theta_D \xi \Delta\overline{\nu} \tag{3.69}$$

The *Noise Equivalent Power* (NEP) is a parameter describing the internal property of the applied detector. It is defined as a ratio of the r.m.s. detector noise voltage V_n to the voltage responsivity R_v:

$$NEP = \frac{V_n}{R_v} \qquad , W \tag{3.70}$$

where R_v is the detector *responsivity* defined as a ratio of the obtained voltage signal V_s to the incident radiant power $\Phi_e(\lambda)$:

$$R_v(\lambda, f) = \frac{V_s}{\Phi_e(\lambda)} \qquad , \frac{V}{W} \tag{3.71}$$

The *detectivity* of the detector is described by the reciprocal of the NEP.

$$D = \frac{1}{NEP} \qquad , \frac{1}{W} \tag{3.72}$$

Jones introduced a new parameter called *normalized detectivity* D^*. It is the detectivity in reference to the area of the detector A_D and the unit frequency band Δf:

$$D^* = \frac{\sqrt{A_D \Delta f}}{NEP} \qquad , \frac{cm\sqrt{Hz}}{W} \tag{3.73}$$

The noise power observed in the time interval t is given by:

$$N = \frac{NEP}{\sqrt{t}} \qquad , \frac{W}{\sqrt{s}} \tag{3.74}$$

And finally, the SNR can be calculated according to:

$$SNR = \frac{P}{N} = \frac{M_e(\overline{\nu}, T)\Theta_D \xi \Delta\overline{\nu}\sqrt{t}}{NEP} \tag{3.75}$$

In general, SNR of an FTIR measurement is proportional to the measurement time (number of collected scans) N, according to:

$$SNR \sim \sqrt{t} \Rightarrow \sqrt{N} \tag{3.76}$$

It is now evident that in order to obtain two times better SNR values, four time longer measurement times are required [17, 40, 45, 58]. A more detailed descriptions of errors occurring in FTIR measurements and the methods of their removal are to find in [59, 60, 61].

3.2.6 Advantages of FTIR Spectroscopy

FTIR spectrometers are characterized by three principal advantages over standard grating spectrometers. These are: *Jacquinot*, *Fellgett* and *Connes* advantage.

Jacquinot Advantage

Jacquinot advantage means a higher optical throughput of FTIR spectrometers than the grating spectrometers measured at the same resolution $\Delta\overline{\nu}$. The difference arises from the fact that the optical throughput Θ_{MI} of an FTIR spectrometer is limited by the entrance aperture of the Michelson-Interferometer.

$$\Theta_{MI} = 2\pi A_{MI} \frac{\Delta\overline{\nu}}{\overline{\nu}_{max}} \tag{3.77}$$

where A_{MI} are the areas of the interferometer mirrors being illuminated. The corresponding expression for the optical throughput of a grating spectrometer Θ_G is:

$$\Theta_G = \frac{h A_G \Delta\overline{\nu}}{f a \overline{\nu}^2} \tag{3.78}$$

where A_G is the area of the illuminated grating, f represents the focal length of the collimating mirror, h and a are the slit height and the grating constant respectively. Usually, the Jacquinot advantage of FTIR spectrometers is of two or more orders of magnitude with respect to grating spectrometers. But in case of low resolved FTIR measurements, optical throughput is limited by the detector optics and the Jacquinot advantage is significantly smaller. Additionally, at low wavenumbers, gratings in grating spectrometers are changed and the Jacquinot advantage decreases.

Fellgett Advantage

The Fegllett advantage is also called the multiplex advantage. It says that FTIR measurements of the same SNR values, spectral resolutions, equal optical throughput etc., take M times less time than the corresponding measurements taken on a grating spectrometer.

$$M = \frac{\overline{\nu}_{max} - \overline{\nu}_{min}}{\Delta\overline{\nu}} \tag{3.79}$$

where M is the number of resolution elements, $\Delta\overline{\nu}$ is the spectral resolution, $\overline{\nu}_{max}$ and $\overline{\nu}_{min}$ are the maximum and minimum wavenumber of the measured spectrum respectively. Thus, FTIR spectra collected with equal data acquisition times as the spectra collected with grating spectrometers, exhibit $\sqrt{M}$ better SNR values.

Connes Advantage

The last advantage of FTIR spectrometers is called Connes advantage, which describes the improved spectral accuracy of FTIR spectrometers in comparison to dispersive spectrometers. It is connected with the sampling mechanism of the interferogram, which was already described in subsection 3.2.5. The accuracy of the sampling is provided by the second He-Ne interferogram instead of the measurement of the mirror velocity or the position of the grating [17, 20, 21, 18, 55].

3.2.7 Infrared Detectors

Infrared detectors are classified with regard to their light detection mechanism. There exist two basic classes of infrared detectors: *thermal* and *photon* detectors. To the class of thermal detectors belong: thermo-elements, bolometers and pyroelectric detectors. The class of photon detectors consists of photoresistors, photovoltaic and photoemissive detectors. In the following subsection the performance of infrared detectors on examples of pyroelectric and MCT-photoconductive detectors, which were used in measurements presented in this thesis, is explained.

In thermal detectors the absorbed radiation induces a change of some material property such as: thermoelectric force, resistance or capacity, due to the rise of the temperature of the sensitive element. The kind of the influenced parameter defines the subtype of the thermal detector. In case of pyroelectric detectors it is the internal electrical polarization and in bolometers the resistance. The amount of this change is proportional to the power, not to the wavelength, of the incident radiation. Therefore, thermal detectors do not exhibit any spectral sensitivity. The detectivity of thermal detectors is low and the response times are long (10^{-3}-10^{-1}) s, but these disadvantages are compensated with the relatively low price and the simplicity of handling of pyroelectric detectors.

The detection process in photon detectors is connected with the absorption of the radiation by lattice-, doping- and conduction- electrons of semiconducting materials. This process is dependant on the energy of the incident radiation. Thus, photon detectors are spectrally sensitive. A comparison of spectral responses of thermal and photon detectors is shown in Figure 3.16. Photon detectors are characterized by higher detectivities and shorter response times in comparison to the thermal detectors. Therefore, they find a place in high sensitive applications. Photon detectors demand, however, to be cooled to temperatures much lower than the ambient temperature. Cooling with liquid nitrogen, to 77 K, is usually sufficient, but in extreme applications liquid helium is used. The handling of liquid gases is cumbersome and influences the price of photon detectors. A promising possibility is thermoelectric cooling not delivering such low temperatures, but together with improved properties of the detector material, providing comparable detectivities to standard photon detectors [62, 40, 63, 64, 65].

Pyroelectric Detectors

Pyroelectric detectors belong to the class of thermal detectors. A thermal detector is characterized by the thermal capacitance C_{th} of the material and the thermal

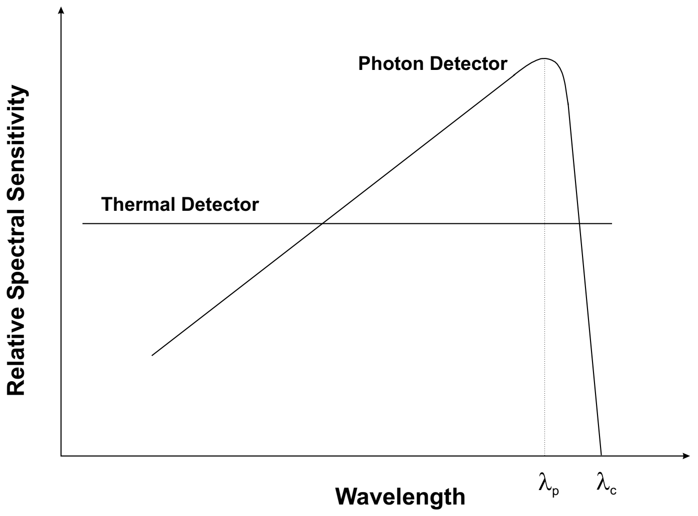

Figure 3.16: Comparison of spectral sensitivities of thermal and photon detectors. Thermal detectors exhibit a constant sensitivity over the whole spectral range. Photon detectors exhibit maximum sensitivity at the peak wavelength λ_p and have a cut-off wavelength λ_c [40].

conductance G_{th} depending on the connection of the detector to the surrounding. The temperature T of the detector element in the thermal equilibrium state (without the illumination) increases by a factor ΔT after the illumination:

$$C_{th}\frac{d\Delta T}{dt} + G_{th}\Delta T = \varepsilon\Phi_0 \tag{3.80}$$

The parameter ε describes the emissivity of the detector and Φ_0 is the incident radiant flux as defined in equation 3.24. The solution of the above equation delivers the expression for the increase of the temperature ΔT:

$$\Delta T = \frac{\varepsilon\Phi_0}{\sqrt{(G_{th}^2 + \omega^2 C_{th}^2)}} \tag{3.81}$$

where Φ_0 represents the amplitude of the incident radiant flux and ω the angular frequency of this radiation. It is now obvious that, in order to obtain significant temperature changes ΔT, small C_{th} and G_{th} are necessary. Small C_{th} values correspond to a small size of the sensitive element. Low thermal conductance G_{th} is obtained by sufficient isolation of the detector body from the surrounding. In practice the detector body is sealed in a vacuum capsule. With the use of these two parameters a so called *thermal time constant* τ_{th} of the thermal detector is defined:

$$\tau_{th} = \frac{C_{th}}{G_{th}} = C_{th}R_{th} \tag{3.82}$$

where R_{th} is thermal resistance of the detector element. Thus, the equation 3.81 takes the form:

$$\Delta T = \frac{\varepsilon \Phi_0 R_{th}}{\sqrt{(1+\omega^2\tau_{th}^2)}} \tag{3.83}$$

Values of thermal constants of thermal detectors are high, typically in order of a few milliseconds. It is also important to emphasize that the quick thermal response of thermal detectors is related to the lower detector responsivity and vice versa.

Next important parameter used in descriptions of thermal detectors is the coefficient K. It is defined as the ratio of the gained voltage signal ΔV to the temperature change ΔT:

$$K = \frac{\Delta V}{\Delta T} \tag{3.84}$$

With the use of the parameter K, the output signal of the detector ΔV generated by the change in the temperature ΔT can be expressed:

$$\Delta V = K\Delta T = \frac{K\varepsilon \Phi_0 R_{th}}{\sqrt{(1+\omega^2\tau_{th}^2)}} \tag{3.85}$$

Thus, the voltage responsivity R_v of any thermal detector according to 3.71 can be expressed by:

$$R_v = \frac{K\varepsilon R_{th}}{\sqrt{(1+\omega^2\tau_{th}^2)}} \tag{3.86}$$

Further considerations concern exclusively pyroelectric detectors [40]. The change of the dipole moment of a material due to a change of its temperature is called the *pyroelectric effect*. Typical pyroelectric materials are insulating crystals. Pyroelectric detectors are sensitive to the speed of the temperature change instead of the absolute value of this change. Therefore, signals measured with pyroelectric detectors have to be modulated. In Figure 3.17 a schematic of a pyroelectric detector and its equivalent electrical circuit are depicted.

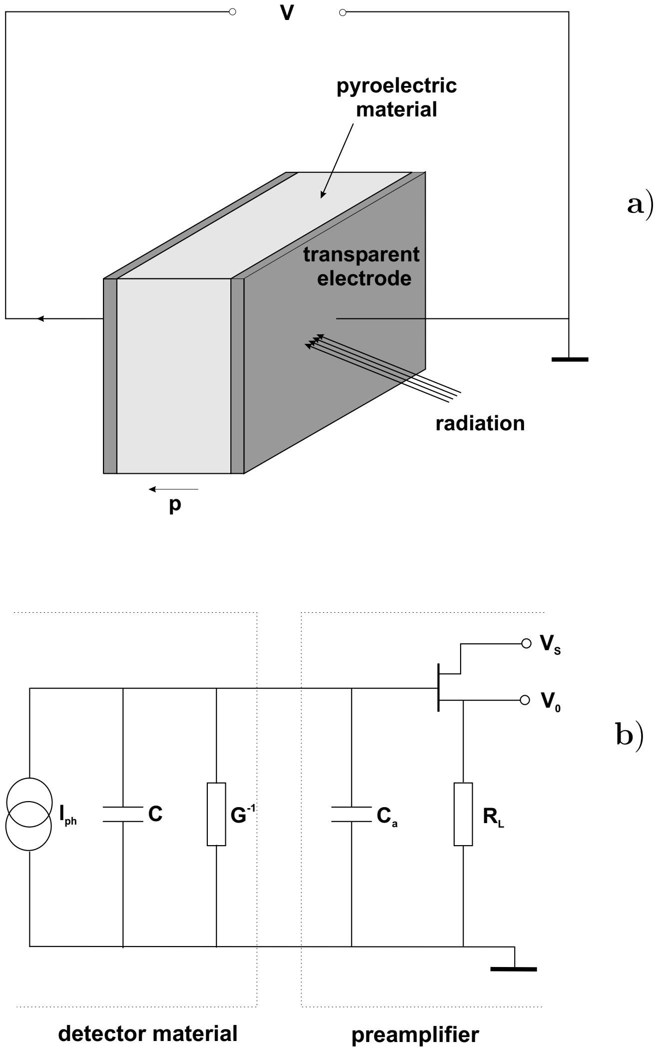

Figure 3.17: Principle of the operation of a pyroelectric detector a), and the corresponding electronic circuit b) [40].

Generally, a pyroelectric detector is a capacitor with electrodes placed perpendicular to the vector of electric polarization. The pyroelectric substance is in its natural state unpolarized. Before introducing the detector into the operating state an electric field is applied in order to arrange polarized domains. In its operating state the pyroelectric substance changes its capacitance, which is registered as a change in a current. The amount of this change is determined by the temperature change and the *pyroelectric coefficient* p of the detector material. The pyroelectric coefficient describes the speed of the change of the electric polarization evoked by the changes of the temperature.

$$p = \frac{dP}{dT} = \left(\frac{dD}{dT}\right)_{E=0} \tag{3.87}$$

In above equation P indicates the internal polarization of the material, which for most of pyroelectric materials, is equal to the electric induction D. As already mentioned, most pyroelectric materials demand an electric field arranging polarized domains, in order to create the electric induction. Thus, the coefficient p is often defined as:

$$p(E) = \left(\frac{dD}{dT}\right)_{E} \tag{3.88}$$

In the configuration presented in Figure 3.17 b, the signal V generated by the photocurrent I_{ph} is equal to:

$$V = \frac{I_{ph}}{\sqrt{(G^2 + \omega^2 C^2)}} \tag{3.89}$$

with G and C being the electric conductance and electric capacitance of the detector material, respectively, as shown in Figure 3.17 b. Thus, the voltage responsivity R_v of a pyroelectric detector is expressed by:

$$R_v = \frac{R\varepsilon pA\omega}{G_{th}\sqrt{(1+\omega^2\tau_{th}^2)}\sqrt{(1+\omega^2\tau_e^2)}} \tag{3.90}$$

where R represents the resistance and A is the surface of the detector body. τ_e is an *electrical time constant* characterizing the pyroelectric detector, defined through:

$$\tau_e = \frac{C}{G} \tag{3.91}$$

The maximum responsivity of the pyroelectric detector is observable for frequencies fulfilling the condition:

$$f_{max} = \frac{1}{\sqrt{\tau_{th}\tau_e}} \tag{3.92}$$

And is expressed by:

$$R_{vmax} = \frac{\varepsilon p A R}{G_{th}(\tau_{th} + \tau_e)} \tag{3.93}$$

Typical values of τ_{th} are on the order of (0.01-10) s and τ_e of (10^{-12}-100) s, dependently on the size of the detector, the capacity and the load resistance. In Figure 3.18 an overview of detectivities of some pyroelectric detectors is presented. A more detailed considerations concerning performance of pyroelectric detectors are contained in [66, 67, 68, 69, 70].

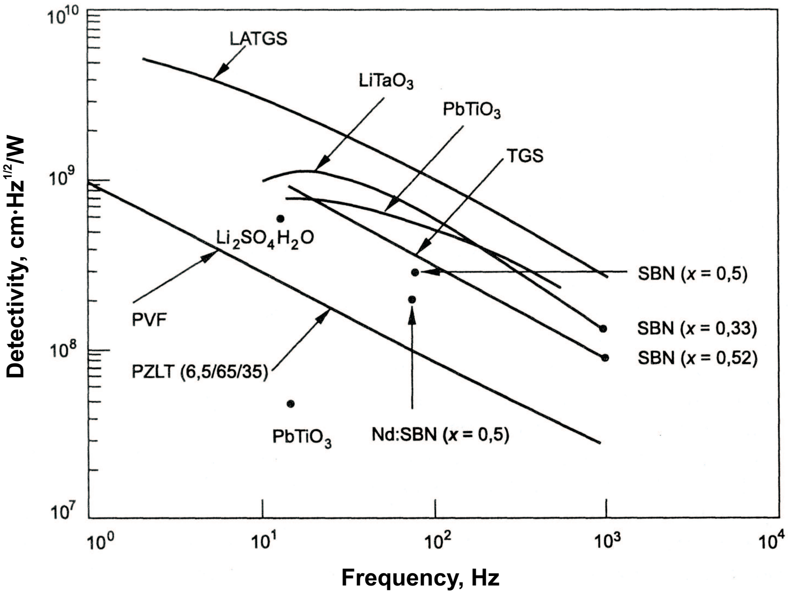

Figure 3.18: Overview of detectivities of pyroelectric detectors [40].

Photon Detectors

Photon detectors function due to the interaction of radiation with the electrons of the semiconducting material. The efficiency of this interaction is called the *quantum efficiency* η, defined as the number of electron-hole pairs generated by

Table 3.5: Physical properties of sample semiconductors [40].

Material	**Temp.** T, K	**Dielectric Constant** ε	**Carrier Life Time** τ, s	**Electron Mobility** $\mu_e, cm^2/Vs$	**Hole Mobility** $\mu_h, cm^2/Vs$	**Energy Bandgap** E_g, eV
Si	300	11.8	10^{-4}	$1.35 \cdot 10^3$	480	1.11
Ge	300	16.0	10^{-2}	$3.90 \cdot 10^3$	1900	0.67
GaN	300	9.00	-	$9.00 \cdot 10^2$	150	3.39
GaAs	300	13.2	$\geq 10^{-6}$	$8.50 \cdot 10^3$	400	1.43
$In_{0,53}Ga_{0,47}As$	300	14.6	10^{-4}	$1.38 \cdot 10^4$	200	0.75
PbS	300	161	$2 \cdot 10^{-5}$	$5.75 \cdot 10^2$	200	0.37
InSb	77	17.9	10^{-7}	$1.00 \cdot 10^6$	10^4	0.23
$Hg_{0,79}Cd_{0,21}Te$	77	18.0	10^{-6}	$2.00 \cdot 10^5$	440	0.10
$Hg_{0,72}Cd_{0,28}Te$	77	16.7	10^{-6}	$8.00 \cdot 10^4$	440	0.25

one absorbed photon. The quantum efficiency takes into account front reflections from the surface of the detector, the absorption, the dissipation as well as the recombination of the charge carriers in the material. Typical natural *reflectivities* of detecting materials are about 30 %. By the use of special antireflection coatings this rate can be minimized below 1 % and therewith the quantum efficiency η increased.

Semiconductors as all other materials are characterized by the absorption coefficient α and the penetration depth $1/\alpha$. Thus, the radiant power Φ_a absorbed in a material is expressed by:

$$\Phi_a(x) = \Phi_i(1 - r)(1 - e^{-\alpha x}) \tag{3.94}$$

where Φ_i represents the incident radiant power and r is the reflection coefficient of the material. In such case the quantum efficiency is equal to:

$$\eta(x) = (1 - r)(1 - e^{-\alpha x}) \tag{3.95}$$

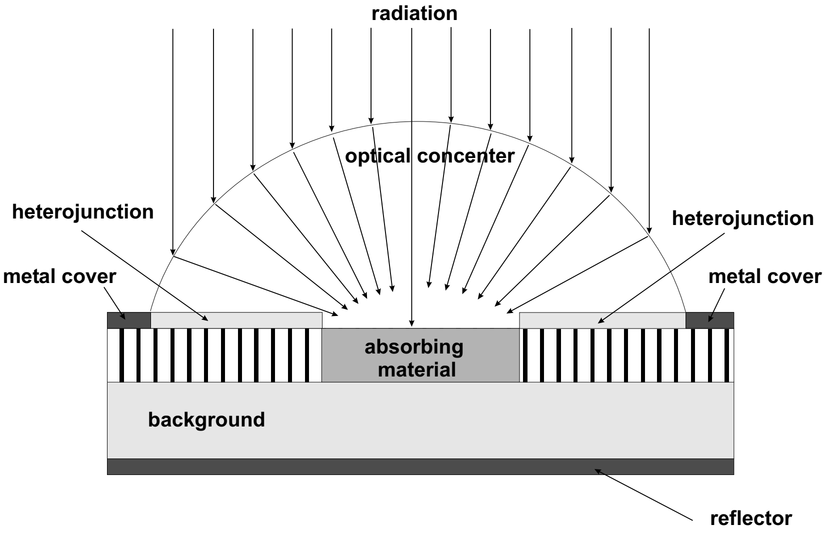

Figure 3.19: Construction of a photon detector. The optical concenter collects the radiation from a bigger area than the area of the semiconductor material itself [40].

Table 3.5 contains values of the main parameters important for materials chosen for the construction of photon detectors. The construction of photon detectors is shown in Figure 3.19. The detecting semiconductor is covered by an optical concenter, collecting the radiation from a much bigger area than the area of the detecting material itself. It increases additionally the efficiency of the detector.

One electron-hole pair generated by the absorbed radiation, induces the formation of next charge carriers. The final number of electron-hole pairs generated by one absorbed photon in the semiconducting material, is called *photon gain g*. Under the condition of a constant g and η, the current sensitivity of a photon detector can be derived [40]:

$$R_i = \frac{\lambda\eta}{hc} qg \tag{3.96}$$

where λ is the wavelength of the absorbed radiation, q is the elementary charge, h is the Planck's constant and c represents the speed of light. Therewith, the voltage responsivity is equal to:

$$R_v = \frac{\eta\lambda\tau V_b}{lwthcn_0} \tag{3.97}$$

In above equation τ is the life-time of photoinduced majority charge carriers, V_b is voltage polarizing the detector, n_0 indicates the equilibrium concentration of charge carriers, l, w *and* t are the length, the width and the thickness of the detector material respectively. Thus, the detectivity of a photon detector is given by:

$$D^* = \frac{\lambda}{hc}\sqrt{\frac{A_0}{A_e}}\frac{\eta}{\sqrt{2(G+R)t}} \tag{3.98}$$

In above expression A_0 and A_e are the optical area and the electrical area of the sensor respectively, t is the thickness of the semiconductor, G and R represent the generation and the recombination rates of charge carriers. From equation 3.98 it is evident that the best results are obtained for thin detector materials. It is also clear that the detectivity of the photon detector is proportional to $1/\sqrt{G}$. The generation rate G consists of two terms: thermal and optical corresponding to the background and the incident radiation respectively:

$$G = G_{th} + G_{op} \tag{3.99}$$

Thus, in order to obtain higher detectivities, possibly low values of G must be reached. Since, the generation rate G is proportional to the Boltzmann's distribution $\sim exp[-E_g/kT]$, where T is the temperature of the detector body and E_g is the energy band-gap of the detector material, the detector must be kept at low temperatures. Long cut-off wavelength detectors have to be cooled to lower temperatures than the short cut-off photon detectors [40].

For measurements presented in this thesis, a so called MCT, a mixture of mercury, cadmium and telluride, detector has been used. It belongs to the class of photoresistors i.e. photoconductive detectors. In photoresistors the incident radiation changes the electric conductance of the semiconductor. These changes are registered by electrical contacts coupled to the detecting material, as depicted in Figure 3.20. In photoconductive detectors a change in the conductance is connected with three kinds of excitations in semiconducting material. The first excitation mechanism occurs if the energy of the incident radiation E is higher than the energy band-gap E_g of the semiconducting material. In this case an free electron-hole pair is created. A long wavelength detectivity limit of such detectors is defined by:

$$\lambda_c = \frac{hc}{E_g} \tag{3.100}$$

The second excitation mechanism is connected with the doping of the detector material. The required excitation energy is adequately lower and the long wavelength cut-off is defined by the ionization energy E_i instead of E_g and lies at about 20 μm. This kind of the excitation process is the most popular for infrared detectors operating in mid-IR spectral range. The used MCT detector is a representative of this kind of photoconductive detectors. The third kind of the excitation, which is the excitation of free charge carriers is relatively seldom and can be observed only at low operating temperatures, T = 4K. More information about photoconductive detectors generally, MCT detectors and semiconducting materials for detectors is contained in [71, 72, 73, 74, 75, 76, 77, 78, 79, 80, 81, 82].

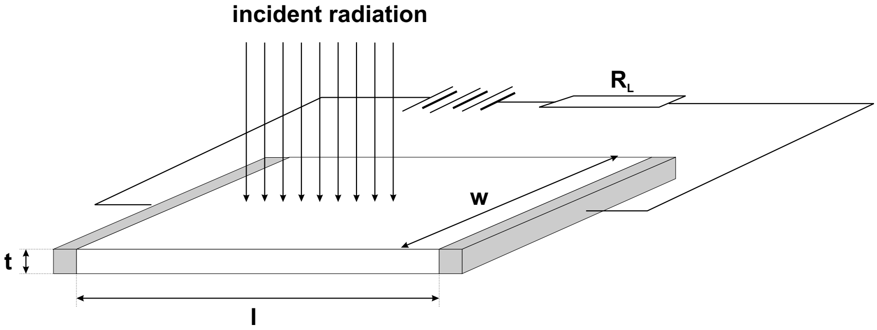

Figure 3.20: Construction of a photoconductive detector operating in a constant current mode [40].

In Figure 3.21 typical characteristics of an MCT detector are illustrated.

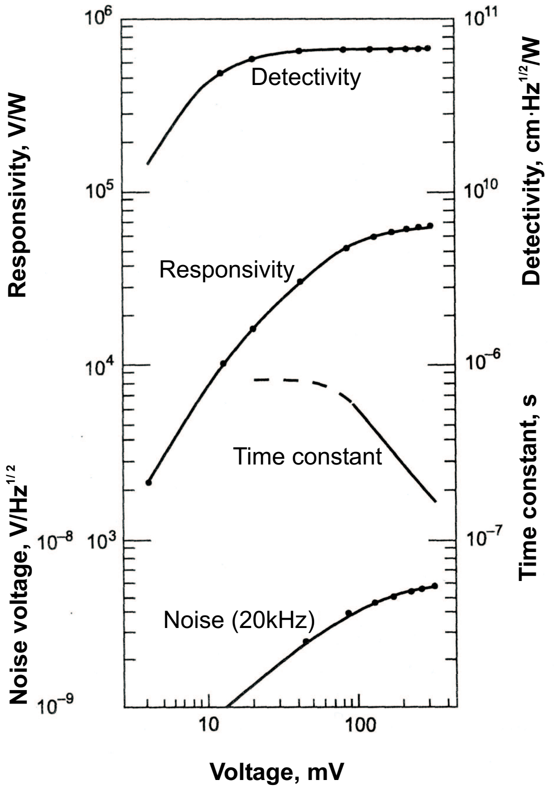

Figure 3.21: Characteristics of a photoconductive MCT detector measured at 12 μm [40].

3.3 Quantitative Analysis

3.3.1 Classical Chemometric Methods

Prior to the quantitative analysis of a sample, a *calibration* of the spectrometer has to be performed. Calibration refers to the collection and evaluation of a set of samples of a known composition and the creation of a statistical model allowing the prediction of the composition of an unknown sample.

In the subsection 3.1.2 the Beer-Lambert's law, in the form of equation 3.22, was derived. The validity of such a form of the Beer-Lambert's law is limited to a specific absorbing component at a specific wavelength of the spectrum. For the mixture of N components at single wavenumber, the Beer-Lambert's law must be expressed by:

$$A(\overline{\nu}) = \sum_{i=1}^{N} \varepsilon_i(\overline{\nu}) c_i l \tag{3.101}$$

The quantitative analysis is usually conducted at several wavenumbers simultaneously. In such a so called multicomponent analysis, the measured absorbances are collected in a matrix. The organization of the matrix depends on the statistical method of the calibration, which is later used. A more exact description of some basic statistical methods is presented below.

In MLR *(Multiple Linear Regression)* and PCR *(Partial Component Regression)* methods, each spectrum or its part build one column of the absorbance matrix, A. The absorbances of each component at one wavenumber build one row of the absorbance matrix.

$$A = \begin{pmatrix} A_{11} & A_{12} & A_{13} & ... & A_{1S} \\ A_{21} & A_{22} & A_{23} & ... & A_{2S} \\ A_{31} & A_{32} & A_{33} & ... & A_{3S} \\ A_{41} & A_{42} & A_{43} & ... & A_{4S} \\ ... & ... & ... & ... & ... \\ A_{W1} & A_{W2} & A_{W3} & ... & A_{WS} \end{pmatrix} \tag{3.102}$$

A_{WS} is the absorbance at W^{th} wavenumber of the sample S. Similarly to the absorbance matrix, the concentration matrix C is created. The columns of the matrix C are built from concentrations of each component of the sample.

$$C = \begin{pmatrix} C_{11} & C_{12} & C_{13} & ... & C_{1S} \\ C_{21} & C_{22} & C_{23} & ... & C_{2S} \\ C_{31} & C_{32} & C_{33} & ... & C_{3S} \\ C_{41} & C_{42} & C_{43} & ... & C_{4S} \\ ... & ... & ... & ... & ... \\ C_{C1} & C_{C2} & C_{C3} & ... & C_{CS} \end{pmatrix} \tag{3.103}$$

C_{CS} is the concentration of the C^{th} component of the sample S. Such an organization of the data is called *column-wise* organization.

The data for PLS *(Partial Least Squares)* are organized *row-wise*. This type of organization is obtained by calculation of the transpose of the matrices A and C.

The data sets of known concentrations used to perform the calibration are called *training sets*. A proper training set should:

- contain all expected components - components are understood as any sources of variation of the spectra; the constituents of the sample, the instrument drift, the temperature or the pressure.
- span concentration ranges of interest
- contain mutually independent samples

In order to check the quality of the conducted calibration, a so called *validation set* is required [83, 84, 51, 85, 86, 87, 88].

Classical Least-Squares

The CLS method is called the *K-matrix calibration* due to the form of the Beer-Lambert's law:

$$A = KC \tag{3.104}$$

In order to compute the calibration, the unknown matrix K has to be found. According to matrix algebra, first, the multiplication by C^T has to be conducted:

$$AC^T = KCC^T \tag{3.105}$$

The elimination of CC^T follows through the multiplication with its inverse:

$$AC^T[CC^T]^{-1} = K[CC^T][CC^T]^{-1} \tag{3.106}$$

Therefore, the K-matrix:

$$K = AC^T[CC^T]^{-1} \tag{3.107}$$

In order to predict the concentration of the unknown sample, the calculated K-matrix is used. The starting point of this calculation is the same as by the calibration:

$$A_{unk} = KC_{unk} \tag{3.108}$$

It should be reiterated, that the matrix A, contains the measured spectra. Therefore, the unknown variable is the matrix C. Following the same rules as by the K-matrix calculation the C-matrix is found:

$$C = [K^T K]^{-1} K^T A_{unk} \tag{3.109}$$

In order to be able to compute the inverse of $K^T K$, the K-matrix must consist of at least as many rows as columns. Since, it has one row for each wavelength and one column for each component, as many wavelengths as components in the sample are necessary. An additional disadvantage of this calibration method is its sensitivity to the accuracy of the determination of the concentration of each component [83, 84, 88].

Inverse Least-Squares

The *Inverse Least-Squares (ILS)* calibration is called the *P-matrix calibration*. It is performed from the inverse of the Beer-Lambert's law:

$$C = PA \tag{3.110}$$

The computing of the P-matrix and the concentration prediction, follows the same way as the K-matrix calculation. The ILS calibration does not require the knowledge of concentrations of all components present in the sample. Thus, the number of necessary calculations is significantly reduced. The ILS calibration delivers also somewhat better results than the CLS calibration. More information about these calibration methods can be found in [83, 84, 89, 90, 88].

3.3.2 Factor Spaces

In order to reduce further the amount of spectral data required for the calibration, a so called *factor analysis* instead of classical calibration methods can be applied.

A *factor space* is a special coordinate system, in which the data are mapped. If two component samples measured at three wavenumbers are considered, the results can be represented as in Figure 3.22.

The axes of the spanned plane contain pure component spectra. In the plane all mixed spectra are placed. One spectrum measured at arbitrarily many wavenumbers is represented by only one point. The problem of finding a new coordinate system for such data, is limited to the searching for *eigenvectors* of this data set. The found eigenvectors are called *factors* or *principal components Vc*. Before the factors Vc are found, some pretreatment of the A matrix is necessary, i.e. the A matrix must be squared:

$$D = A^T A \tag{3.111}$$

The first eigenvector must lie in the plane of the data. It is calculated so that the distances between the new axis and the data points are minimized. The next eigenvectors have to be orthogonal and mutually orthonormal to each other. This implies that the second vector also lies in the plane of the data. The found axes span the *basis space* of the data set. The example of the found eigenvectors for data set is also shown in Figure 3.22.

Principal Component Regression

The eigenvectors contain all the collected spectral data: both the desired information and the noise. Removing the noise is unequivocal with rejecting of some eigenvectors before the calibration process. The number n of significant factors is determined by validation functions such as: Malinowski imbedded error function, Malinowski IND function or Brown FRAC function. The spectral data collected in the A matrix must be now projected to the new coordinate system:

$$A_{proj} = Vc^T A \tag{3.112}$$

A_{proj} contains the spectral data projected on the factors. The further PCR calibration proceeds analog to the ILS calibration, with the calibration matrix F:

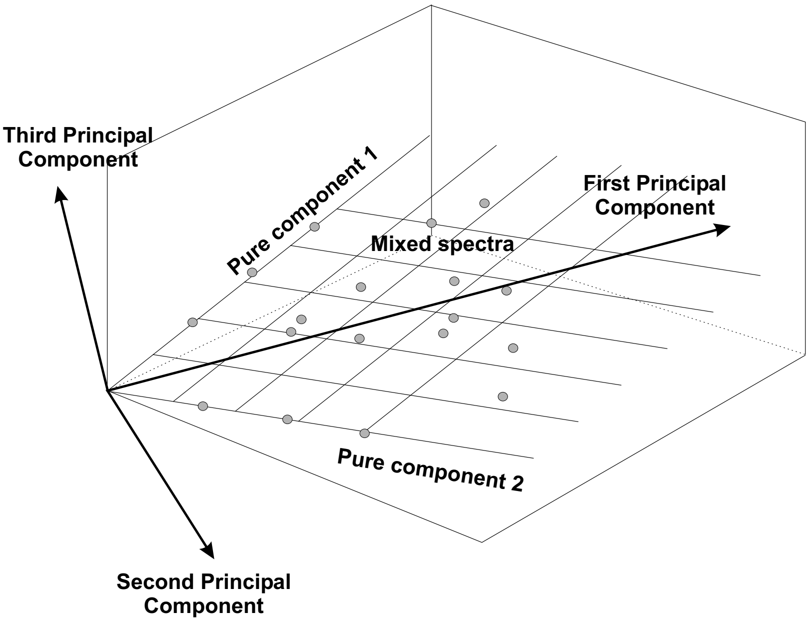

Figure 3.22: Example of three principle components [88].

$$C = FA_{proj} \tag{3.113}$$

The found calibration matrix F is equal to:

$$F = CA_{proj}^T [A_{proj} A_{proj}^T]^{-1} \tag{3.114}$$

The prediction of the concentration of the unknown sample follows as:

$$C_{unkn} = FVc^T A_{unkn} = F_{cal} A_{unkn} \tag{3.115}$$

Practical calibration can be presently performed by the use of specialized software such as Chemometrics Toolbox for MatLab. More information about the calibration of spectral data with the use of factor spaces are contained in [83, 84, 91, 92, 88].

4 Attenuated Total Reflectance Spectroscopy

4.1 Internal Reflection

In the presented thesis an *Attenuated Total Reflectance* (ATR) measurement technique, combined with infrared fibers, was used. The ATR technique enables FTIR-measurements of liquids without an otherwise indispensable sample preparation. For a measurement, it is sufficient and necessary for the sample to stay in a contact with the surface of an ATR crystal. In the current chapter the reader is introduced to the basics of the attenuated total reflectance and infrared fibers.

Understanding of the internal reflection is necessary for explaining of the phenomenon of attenuated total reflectance - ATR. For this purpose, the usual reflection at the surface of two media is explained below. An incident electromagnetic wave is described by:

$$\vec{E}_i = \vec{E}_{0i} \exp\left[j\left(\vec{k}_i \cdot \vec{r} - \omega_i t\right)\right] \qquad (4.116)$$

The index *i* indicates the incident wave and *j* is the complex number. At the surface of two media of refractive indices n_i and n_t the electromagnetic wave reflects and refracts. If $n_i > n_t$ a so called *Internal Reflection* takes place. On the contrary, if $n_i < n_t$ *External Reflection* occurs. The reflected part of the light is marked with the index *r* and the refracted part with the index *t*. The plane in which all three beams: incident, reflected and refracted are lying, is called the *incidence plane*. In Figure 4.23 the incident, reflected and transmitted (refracted) rays, as well as the incidence and reflection planes are illustrated [48].

Depending on the direction of the electric and magnetic field vectors with reference to the incidence plane, the parallel or perpendicular parts of the electromag-

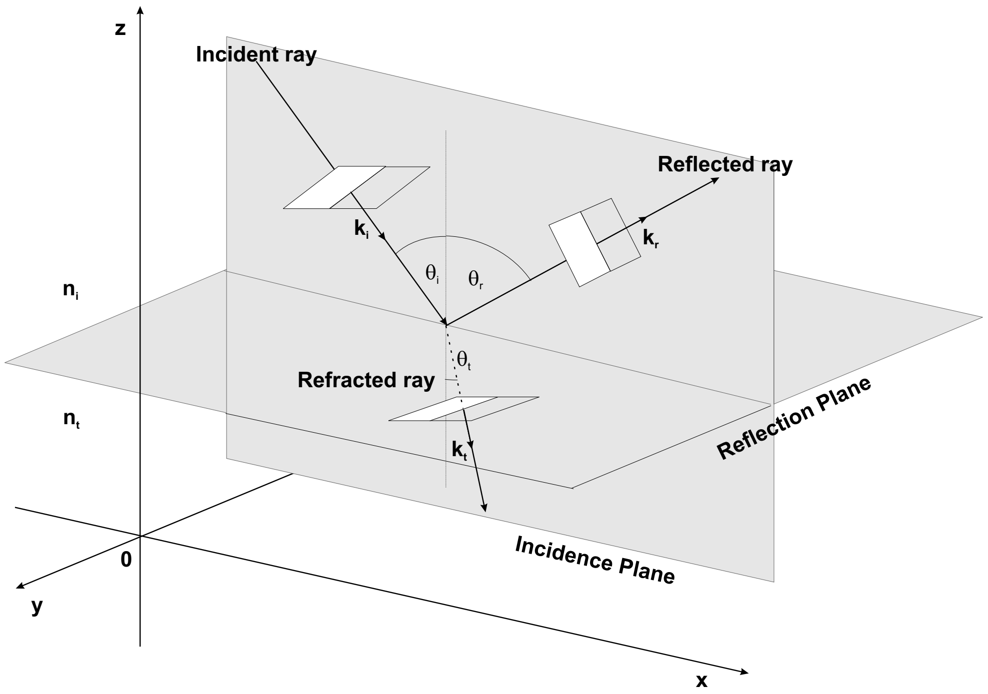

Figure 4.23: Reflection and refraction of the light at the surface of two media [48].

netic waves are considered. Considerations concerning the electric and magnetic fields are similar. Thus, below only behaviour of the electric field is presented. In Figure 4.24 example directions of the electric and magnetic field vectors, as well as wavevectors k, of the incident, reflected and refracted beams are shown.

At the place of reflection boundary conditions for the electromagnetic field have to be fulfilled. First of all, a continuum of the electric field components tangential to the reflection plane has to be reached:

$$\vec{E}_{\perp i} + \vec{E}_{\perp r} = \vec{E}_{\perp t} \tag{4.117}$$

The solution of above condition gives the well established reflection lows:

$$\theta_i = \theta_r \tag{4.118}$$

$$n_i sin\theta_i = n_t sin\theta_t \tag{4.119}$$

where θ_i is the incidence angle, θ_r is the reflection angle and θ_t is the refraction angle. n_i and n_t are refractive indices of the first (containing the incident beam)

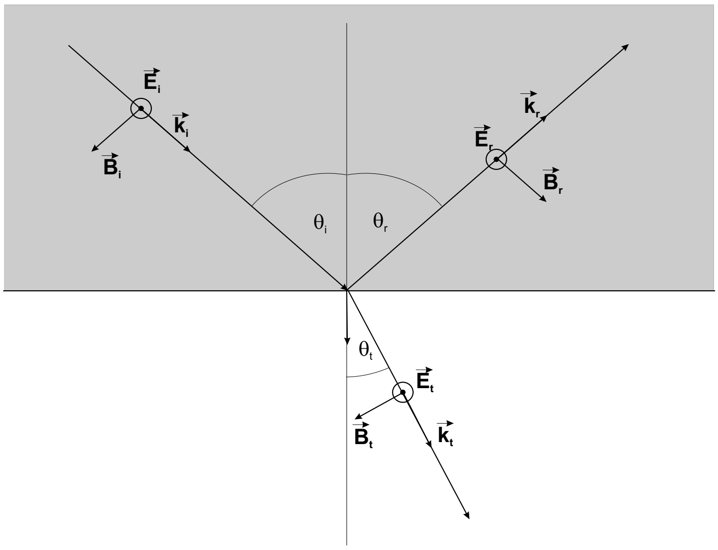

Figure 4.24: Directions of electric and magnetic field vectors of an electromagnetic wave at the place of reflection. The electric field is perpendicular to the incidence plane [48].

and second medium (containing the refracted beam), respectively. Considering the magnetic components of the electromagnetic wave and the relations between the magnetic and electric fields, the so called Fresnel Equations are derived. The Fresnel equations describe quantitative fractions of the reflected and transmitted light. For perpendicular components of the electric field these are expressed by:

$$r_\perp = \left(\frac{E_{0r}}{E_{0i}}\right)_\perp = \frac{\frac{n_i}{\mu_i}\cos\theta_i - \frac{n_t}{\mu_t}\cos\theta_t}{\frac{n_i}{\mu_i}\cos\theta_i + \frac{n_t}{\mu_t}\cos\theta_t} \tag{4.120}$$

$$t_\perp = \left(\frac{E_{0t}}{E_{0i}}\right)_\perp = \frac{2\frac{n_i}{\mu_i}\cos\theta_i}{\frac{n_i}{\mu_i}\cos\theta_i + \frac{n_t}{\mu_t}\cos\theta_t} \tag{4.121}$$

where r represents amplitude reflection coefficient and t represents amplitude transmission coefficient. For most existing dielectric materials $\mu_i \approx \mu_t \approx \mu_0$, causing independence of the equations 4.120 and 4.121 on the permeability μ. The Fresnel equations for parallel compounds of the electric field are:

$$r_{\|} = \left(\frac{E_{0r}}{E_{0i}}\right)_{\|} = \frac{n_t \cos\theta_i - n_i \cos\theta_t}{n_t \cos\theta_i + n_i \cos\theta_t} \tag{4.122}$$

$$t_{\|} = \left(\frac{E_{0t}}{E_{0i}}\right)_{\|} = \frac{2n_i \cos\theta_i}{n_i \cos\theta_t + n_t \cos\theta_i} \tag{4.123}$$

Quantities more adequate to the measured values of reflected and transmitted light intensities are *Reflectivity* - R and *Transmittance* - T. Both are defined as:

$$R = \frac{I_r}{I_i} = \left(\frac{E_{0r}}{E_{0i}}\right)^2 = r^2 \tag{4.124}$$

$$T = \frac{I_t}{I_i} = \frac{n_t \cos\theta_t}{n_i \cos\theta_i}\left(\frac{E_{0t}}{E_{0i}}\right)^2 = \frac{n_t \cos\theta_t}{n_i \cos\theta_i} t^2 \tag{4.125}$$

The total light intensity remains unchanged:

$$T + R = 1 \tag{4.126}$$

A special case of internal reflection is *Total Internal Reflection*, occurring when all incident light is completely reflected into the optically denser medium. It occurs, if the incidence angle θ_i exceeds the critical angle θ_c, defined as:

$$\theta_c = \arcsin\frac{n_t}{n_i} \tag{4.127}$$

In total internal reflection, apart from the reflected beam transporting the total light intensity, the refracted beam exists and spreads along the reflection plane. It is a so called *inhomogeneous electromagnetic wave*. Its existence can be proved, if the reflection coefficients $r_{\|}$ and $r_{\perp}$ are transformed to:

$$r_{\|} = \frac{n_{ti}^2 \cos\theta_i - \sqrt{n_{ti}^2 - \sin^2\theta_i}}{n_{ti}^2 \cos\theta_i + \sqrt{n_{ti}^2 - \sin^2\theta_i}} \tag{4.128}$$

$$r_{\perp} = \frac{\cos\theta_i - \sqrt{n_{ti}^2 - \sin^2\theta_i}}{\cos\theta_i + \sqrt{n_{ti}^2 - \sin^2\theta_i}} \tag{4.129}$$

For the total internal reflection $\theta_i > \theta_c \Rightarrow \sin\theta_i > n_{ti}$, $n_{ti} = n_t/n_i$ and the expression under the square root is negative. It implies that both coefficients $r_{\parallel}$ and $r_{\perp}$ are now complex quantities and the reflectivity R must be calculated as rr^*. The result of this calculation is the internally reflected light intensity [22, 48, 25].

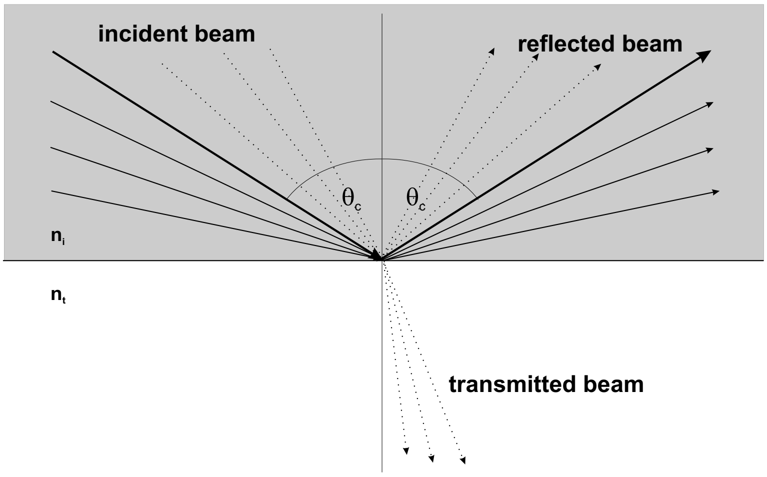

Figure 4.25: Incident, reflected and refracted beams travelling below $(\cdots)$ and over (—) the critical angle θ_c.

From Figure 4.25 it is evident that all the light travelling in the medium under angles larger than θ_c, is reflected back into the optically denser medium without the loss of intensity. Example parallel and perpendicular reflectivities R, calculated for $n_{ti} = 0.357$, are plotted in Figure 4.26. The calculated critical angle of this system is 36°.

In Figure 4.27 the phenomenon of the total internal reflection, observed in a ZnSe crystal, measured with HeNe laser (λ = 632 nm) is presented. The laser beam reflected inside the crystal is visible. Six internal reflections at one side surface of the crystal took place.

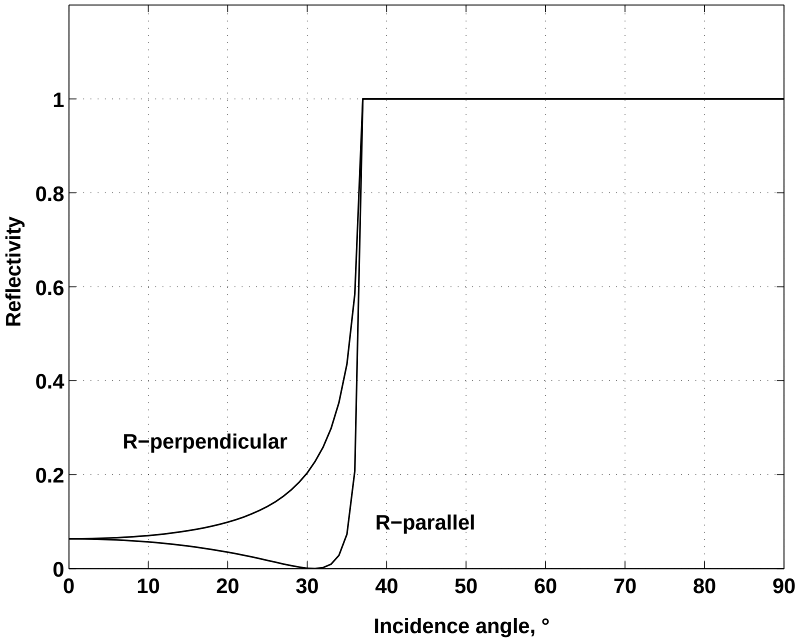

Figure 4.26: Parallel and perpendicular components of the reflectivity calculated at $n_{ti} = 0.357$, (ZnS crystal $(n_i) = 2.8$/air interface).

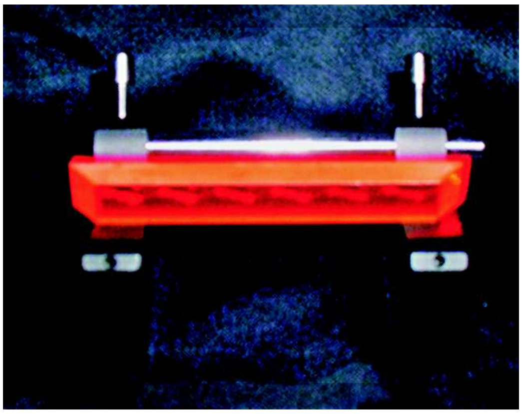

Figure 4.27: Internal total reflection measured in a ZnSe crystal with HeNe Laser $\lambda = 632$ nm.

4.2 Attenuated Total Reflectance

The phenomenon of Attenuated Total Reflection (ATR) has the same origin as the total internal reflection. The light in an optically denser medium travels under angles exceeding the critical angle θ_c and at each place of reflection the light is attenuated. The reason for this attenuation is complex refractive index $\hat{n}_t$ of the optically rarer medium:

$$\hat{n}_t = n(1 - i\kappa) \tag{4.130}$$

The coefficient κ describes the absorbtion properties of the substance and is equal to zero only for fully non-absorbing substances.

For the refracted electromagnetic wave:

$$\vec{E}_t = \vec{E}_{0t} \exp\left[j\left(\vec{k}_t \cdot \vec{r} - \omega_i t\right)\right] \tag{4.131}$$

the wavevector $\vec{k}_t$ comprises of two components $\vec{k}_{xt}$ and $\vec{k}_{zt}$, as depicted in Figure 4.23. Thus:

$$\vec{k}_t \cdot \vec{r} = k_{xt}x + k_{zt}z \tag{4.132}$$

If the Snellius law is applied, components k_{xt} and k_{zt} can be expressed by:

$$k_{xt} = \frac{k_t}{n_{ti}} \sin\theta_i \tag{4.133}$$

$$k_{zt} = \pm jk_t\sqrt{\frac{\sin^2\theta_i}{n_{ti}^2} - 1} = \pm j\beta \tag{4.134}$$

Thus, the refracted electric field can be written in a form of:

$$\vec{E}_t = \vec{E}_{0t} \exp\left(\pm\beta z\right) \exp\left[j\left(\frac{k_t}{n_{ti}} x \sin\theta_i - \omega_i t\right)\right] \tag{4.135}$$

A physically meaningful result is only obtained, when the expression has a minus in the exponent. It means that the penetration of the electric field exponentially decreases in the optically rarer medium [22, 23]. A more descriptive approach to this phenomenon explains the origin of the penetrating field with the use of extended diameter of the incident beam. Due to this, an interference of the incident and the reflected beam is seen. The result of this interference is a standing wave perpendicular to the reflection plane, as shown in Figure 4.28. An characteristic feature of this standing wave is the existence of a nonzero amplitude E_0 at the reflection place.

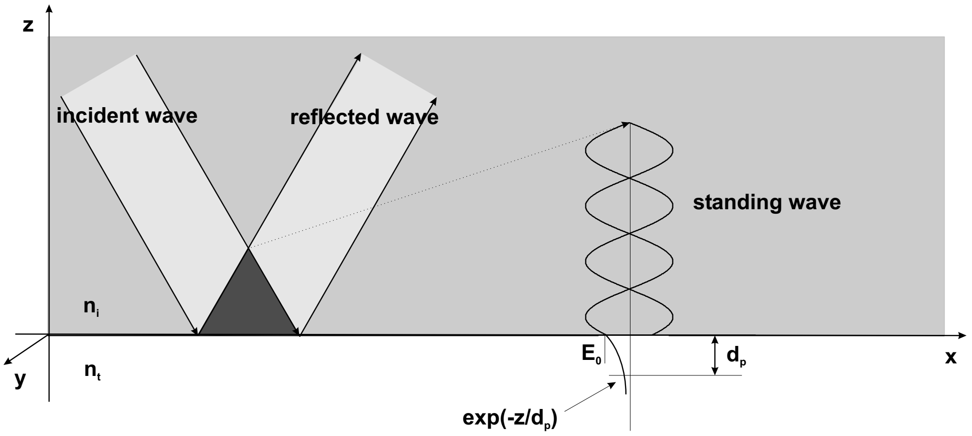

Figure 4.28: Standing wave in an internal reflection element (n_i) and the evanescent field arising in the optically rarer medium (n_t).

The standing wave possesses all three spatial components E_x, E_y and E_z of the electric field, on the contrary to the normal electromagnetic wave, which exhibits no components in the direction of the propagation. The components of the standing wave are expressed by:

$$E_{x0} = \frac{2\sqrt{\sin^2\theta_i - n_{ti}^2}\cos\theta_i}{\sqrt{1-n_{ti}^2}\sqrt{(1+n_{ti}^2)\sin^2\theta_i - n_{ti}^2}} \tag{4.136}$$

$$E_{y0} = \frac{2\cos\theta_i}{\sqrt{1-n_{ti}^2}} \tag{4.137}$$

$$E_{z0} = \frac{2\sin\theta_i\cos\theta_i}{\sqrt{1-n_{ti}^2}\sqrt{(1+n_{ti}^2)\sin^2\theta_i - n_{ti}^2}} \tag{4.138}$$

As mentioned previously, the boundary conditions at the interface of the two media demand that the tangential components of the electric field are continuous. Therefore, the parallel and perpendicular components of the electric field can be expressed as:

$$E_{\|} = \sqrt{|E_{x0}|^2 + |E_{z0}|^2} \tag{4.139}$$

$$E_{\perp} = E_{y0} \tag{4.140}$$

The electric field of the standing wave enters the rarer medium, where it undergoes the attenuation with the distance z, according to Figure 4.28:

$$E = E_0 \exp\left(\frac{-z}{d_p}\right) \tag{4.141}$$

where d_p represents the penetration depth and z is the distance from the reflection plane. The plot of simulated amplitude reflection coefficient r, depending on κ is shown in Figure 4.29. From Figure 4.29 it is evident that even for incidence angles higher than the critical angle calculated for the set crystal/air, as illustrated in Figure 4.26, no total internal reflection takes place.

The *penetration depth* d_p into the optically rarer medium is defined as the distance required for the electric field amplitude to fall to e^{-1} of its value at the interface of the two media. The penetration depth is expressed by:

$$d_p = \frac{\lambda}{2\pi n_i \sqrt{\sin^2\theta_i - n_{ti}^2}} \tag{4.142}$$

where λ is wavelength of the radiation in the vacuum and $n_{ti} = n_t/n_i$. The penetration depth, although being a quantity describing a physical phenomenon, is not very useful in spectroscopy. More important is the *effective thickness* d_e. The effective thickness means such a thickness of a measured sample, at which absorption bands measured with ATR technique are exact as strong as absorption bands measured in transmission. This condition can be written as:

$$\int_0^{d_e} I_1 \alpha' c dz = \int_{z_1}^{z_2} I_2 \alpha' c dz \tag{4.143}$$

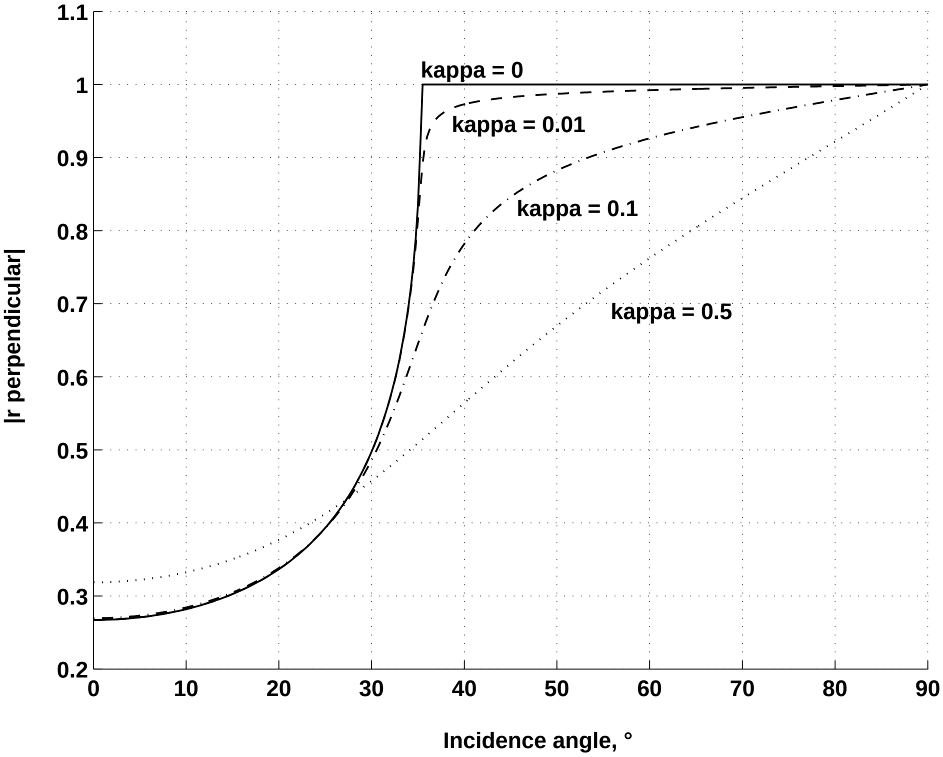

Figure 4.29: Dependance of the perpendicular amplitude reflection coefficient r on the absorption coefficient κ, calculated for $n_{ti} = 0.357$, $\theta_c = 36°$, (ZnS crystal $(n_i) = 2.8$/air interface).

where $(z_1 - z_2)$ is the thickness of the sample, $\alpha' = -\varepsilon ln(10)$, ε is the absorptivity (molar absorption coefficient) of the sample and c is the concentration of the sample. The solution of above condition delivers four expressions for effective thicknesses, depending on the light polarizations and the physical thickness of the sample. Analytic solutions are possible only under condition of low absorbing substances $\kappa << 0.1$. In this case the transmittance spectra measured in traditional infrared spectroscopy can be approximated with:

$$T = 1 - \alpha d \tag{4.144}$$

where α indicates the absorption coefficient and d represents the real thickness of the sample. For internal reflection measurements the reflectivity R, per N reflections, can be analogously written as:

$$R = 1 - N\alpha d_e \tag{4.145}$$

In general, a differentiation between bulk samples and thin film samples has to be made. A sample is considered to be in a form of a thin film, if its physical thickness is smaller than the penetration depth d_p of the electric field into the sample. For most of materials, penetration depths are of few micrometers. All samples having the thickness bigger than d_p are considered to be bulk materials. The effective thicknesses for thin films depending on light polarizations are expressed by:

$$d_{e\parallel} = \frac{4n_{ti} d \cos\theta_i [(1 + n_{at}^4)\sin^2\theta_i - n_{ai}^2]}{(1 - n_{ai}^2)[(1 + n_{ai}^2)\sin^2\theta_i - n_{ai}^2]} \tag{4.146}$$

$$d_{e\perp} = \frac{4n_{ti} d \cos\theta_i}{(1 - n_{ai}^2)} \tag{4.147}$$

where d is the thickness of the sample and θ_i is the incidence angle. It should be emphasized that the third medium with the refractive index n_a influences the effective thickness of the sample by $n_{at} = n_a/n_t$ and $n_{ai} = n_a/n_i$.

The corresponding expressions for bulk materials are:

$$d_{e\parallel} = \frac{\lambda n_{ti} \cos\theta_i (2\sin^2\theta_i - n_{ti}^2)}{n_i \pi (1 - n_{ti}^2)[(1 - n_{ti}^2)\sin^2\theta_i - n_{ti}^2]\sqrt{\sin^2\theta_i - n_{ti}^2}} \tag{4.148}$$

$$d_{e\perp} = \frac{\lambda n_{ti} \cos\theta_i}{n_i \pi (1 - n_{ti}^2)\sqrt{\sin^2\theta_i - n_{ai}^2}} \tag{4.149}$$

In the presented work, all measured samples are treated as bulk materials. Additionally, no light polarization has been used, due to the use of infrared fibers, which are unable to hold the polarization of the radiation [23, 24, 93, 94, 95, 96, 97].

4.3 Infrared Fibers

A great possibility for the broadening of application fields for infrared spectroscopy lies in a combination of ATR measurement technique with infrared fibers enabling access to the investigated substance. The fibers for infrared spectral range differ from typical fibers for visible spectral range in all aspects: the mechanical structure, stability, sensitivity and the price. In this section some basic knowledge about infrared fibers is presented. In principle, the performance of any fiber uses the phenomenon of the total internal reflection, described in previous sections.

The light inside a fiber is transmitted along a high refractive index core surrounded by a low refractive index cladding. The whole structure is secured by an additional jacket, as illustrated in Figure 4.30.

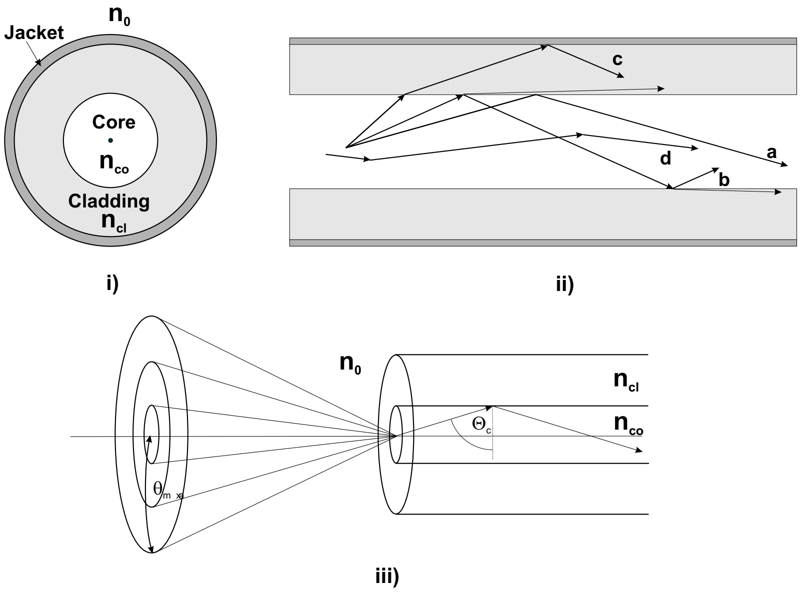

Figure 4.30: Performance of optical fibers: i) cross-section of the fiber showing its internal structure, ii) possible ray trays existing in the fiber: a-meridional ray, b-leaky ray, c-ray corresponding to the cladding mode and d-skew ray, iii) the visualization of the numerical aperture of the fiber [25].

With regard to the profile of the refractive index of the core, the fibers are classified into: *step-index fibers* and *gradient-index fibers*. The step-index fibers exhibit discontinuity of the refractive index at the core/cladding interface:

$$n(r) = \begin{cases} n_{co} & : \quad r < r_{core} \\ 0 & : \quad r \geq r_{core} \end{cases} \tag{4.150}$$

with n_{co} being a refractive index of the fiber core, r_{core} represents the radius of the core and r being the distance from the center of the fiber. In gradient-index fibers, the refractive index changes continually with the distance from the center of the core:

$$n(r) = \begin{cases} n_{co}\left[1 - \Delta\left(\frac{r}{r_{core}}\right)^{\alpha}\right] & : \quad r < r_{core} \\ n_{co}\left(1 - \Delta\right) & : \quad r \geq r_{core} \end{cases} \tag{4.151}$$

The above form of the refractive index is called α - profile. The Δ is the normalized core-cladding index difference:

$$\Delta = \frac{n_{co}^2 - n_{cl}^2}{2n_{cl}^2} \tag{4.152}$$

with n_{cl} being the refractive index of the cladding. Possible ways of the propagation of rays in a fiber are illustrated in Figure 4.30. Only *meridional rays*, reflected at the core/cladding interface, are totally transmitted. The other rays called *leaky*, *skew* and *cladding rays* undergo a partial attenuation. Leaky rays lose a part of their energy at each place of reflection. The cladding modes undergo refraction at the core-cladding interface and the total reflection at the cladding-jacket interface. Finally, the skew rays are transmitted inside the fiber although they do not follow the symmetry axis of the fiber.

In order to propagate any ray along the fiber, a general condition at the entrance of the fiber has to be fulfilled. The entrance angle of the ray must assure the reflection angle within the fiber being higher than the calculated critical angle θ_c, according to equation 4.127. The maximal accepted entrance angle Θ_{max}, defines one of the most important parameters of fibers, which is the *Numerical Aperture N.A.*:

$$N.A. = \sin\Theta_{max} \tag{4.153}$$

Considering mutual relationships between n_{co} and n_{cl} (Figure 4.30) the numerical aperture can be calculated according to:

$$N.A. = n_{co}\sqrt{1-\sin^2\theta_c} = \sqrt{n_{co}^2 - n_{cl}^2} \tag{4.154}$$

It has been already mentioned that not all introduced rays propagate inside of a fiber. The condition of the critical angle was the result of the ray optics. The wave nature of the light reveals in further limitation of the number of transmitted rays. The light inside a fiber must additionally satisfy a self-interference condition. The rays fulfilling this condition are called *modes* and are specified by solutions of a scalar wave equation:

$$\nabla^2\Psi(r,\theta,z) + k_0^2 n^2(r)\Psi(r,\theta,z) = 0 \tag{4.155}$$

where Ψ represents the wave function, k_0 is the vacuum wave vector, and *n(r)* is the radial profile of the refractive index.

Further separation of the above equation into three independent fractional equations with the use of assumption:

$$\Psi(r,\theta,z) = R(r)\Theta(\theta)Z(z) \tag{4.156}$$

delivers dependency on the radial variable *r*:

$$\frac{d^2R}{dr^2} + \frac{1}{r}\frac{dR}{dr} + \left(k_0^2 n^2(r) - \beta^2 - \frac{m^2}{r^2}\right) R = 0 \tag{4.157}$$

In the above equation R is the radial part of the wave function Ψ, k_0 is the vacuum wave vector, β represents the propagation constant, *n* is the refractive index and *m* is the azimuthal mode number. The above equation possesses analytical solutions only for isotropic cylindrical symmetry, such as in case of step index cylindrical fibers. In such case, the solutions for the core ($r < r_{core}$) are represented by Bessel functions of the first art *J*. For m = 0 they are expressed by:

$$R(r) = \frac{J_0\left(\sqrt{k_0^2 n_{co}^2 - \beta^2}\left(\frac{r}{r_{core}}\right)\right)}{J_0\left(\sqrt{k_0^2 n_{co}^2 - \beta^2}\right)} \tag{4.158}$$

The corresponding solutions for the cladding ($r \geq r_{core}$) are:

$$R(r) = \frac{K_0\left(\sqrt{\beta^2 - k_0^2 n_{cl}^2}(\frac{r}{r_{core}})\right)}{K_0\left(\sqrt{\beta^2 - k_0^2 n_{cl}^2}\right)} \tag{4.159}$$

with K_0 as the modified Bessel function.

The solution for the Z(z) is:

$$Z(z) = \exp(j\beta z) \tag{4.160}$$

Therefore, an exponential decrease of the light intensity along the direction of propagation occurs, dependant on the propagation constant β. The propagation constant can be a complex quantity. The real part of β is responsible for a phase shift on propagation. If it is normalized to the vacuum wave vector, an *effective refractive index*, N_{eff} for the mode is obtained:

$$N_{eff} = \frac{Re\{\beta\}}{k_0} \tag{4.161}$$

The imaginary part of β represents the attenuation α of the fiber. This is caused by fundamental scattering, absorption and scattering on impurities from the production process.

$$\alpha = 2Im\{\beta\} \tag{4.162}$$

The fibers for optical communication are mostly single-mode fibers characterized by small diameters. Multi-mode fibers have large cores and big numerical apertures. This enables transmission of broad spectra. In order to obtain a single mode fiber, the following condition has to be satisfied:

$$\frac{2\pi r_{core}}{\lambda}\sqrt{n_{co}^2 - n_{cl}^2} < 2.405 \tag{4.163}$$

More detailed description of physics of optical fibers is given in the literature [98, 99, 100, 101, 102, 103, 104, 25].

Infrared fibers belong mostly to the multi-mode fibers. The first infrared fibers were produced in the mid-1960's for needs of military and surgical applications.

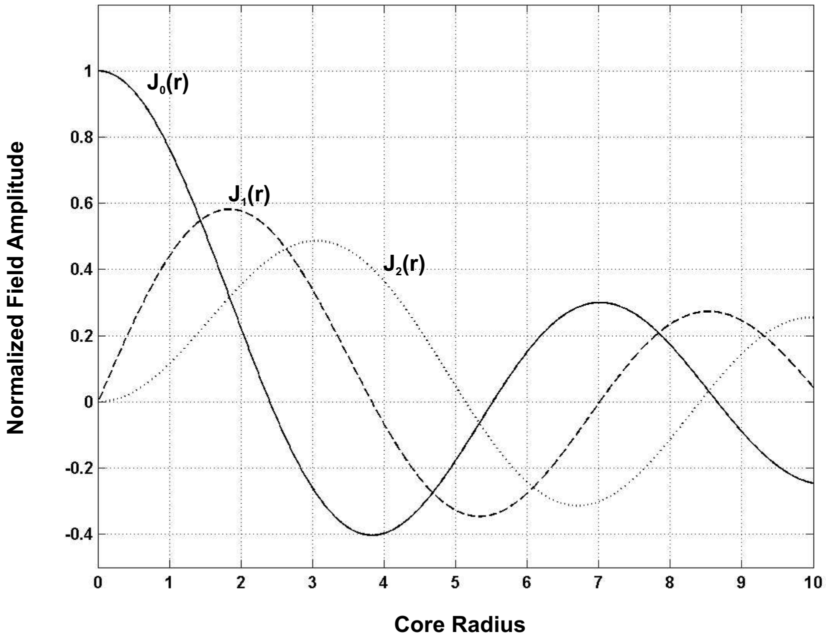

Figure 4.31: Bessel functions of the zero, first and second order.

Most infrared fibers are concentric in their shape and their lengths do not exceed few tens of centimeters. The length is limited by poor mechanical stability of the fibers, as well as strong light attenuations within them. The poor mechanical stability is a result of infrared transparency, which demands materials made up of heavy atoms with weak bonds between them. Due to this, typical operational times of IR-fibers are a few months. This, in addition to the price of thousands of Euros per meter, is a big disadvantage of infrared fibers. Because of all these reasons, application of IR-fibers is still limited to chemical sensing, thermometry and laser power delivery. In Table 4.6 typical representatives of three main groups of infrared fibers: glass, crystalline and hollow waveguides, are collected. None of them approaches the performance quality of typical silica fibers for visible applications.

Depending on the chemical composition, the transmission ranges and attenuations of single fibers vary strongly. In Figure 4.32. attenuations and transmission ranges of sample infrared fibers are plotted.

Table 4.6: Sample materials belonging to three main classes of IR-fibers [25].

Main Class	Subcategory	Examples
Glass	Heavy metal fluoride (HMFG)	$ZrF_4 - BaF_2 - LaF_3 - AlF_3 - NaF$
	Germanate	$GeO_2 - PbO$
	Chalcogenide	As_2S_3, AsGeTeSe
Crystal	Polycrystaline (PC)	AgBrCl
	Single crystal (SC)	Sapphire
Hollow	Metal/dielectric film	Hollow glass waveguide
	Refractive index < 1	Hollow sapphire at 10.6 μm

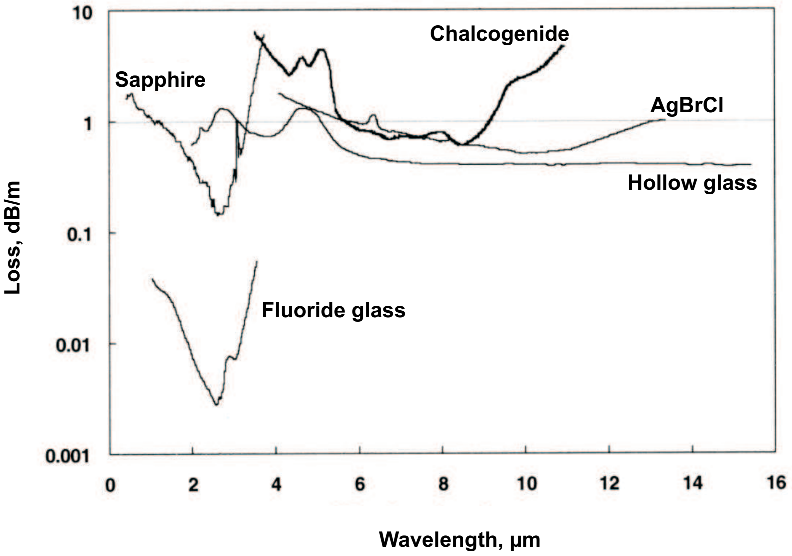

Figure 4.32: Spectral ranges and attenuations of infrared fiber samples [25].

In Table 4.7 main properties of infrared fibers are compared.

Measurements presented in this thesis were conducted with chalcogenide infrared fibers. Chalcogenide fibers are glass fibers having low softening temperatures. This limits their use at elevated temperatures. On the other hand chalcogenide glasses are more stable, durable and insensitive to moisture. They do not transmit very well in the visible spectral range and their refractive indices are relatively high. Additionally, the dependence of their refractive index on the temperature is large. These properties limit the use of chalcogenide glasses in laser delivery applications, but they are still optimal for evanescent field sensors such as ATR sensors. A general attribute of all chalcogenide fibers is strong infrared absorption originating from contaminants from production process such as: H_2O, OH^-, $S-H$ or Se. Due to this, these fibers are not proper for applications detecting at 2.78, 4.0, 4.6 and 6.3 cm^{-1}. The attenuation of sample chalcogenide fibers is also shown in Figure 4.32 [25]. The information about the construction of fiber probes for spectroscopy, fiber couplers, fiber mixers, fiber spectrometers and the ways of remote analysis by the use of infrared fibers are contained in [105, 26, 106].

Table 4.7: Selected properties of IR-fibers [25].

Property	**Glass**		
	Silica	**HMFG**	**Chalcogenide**
Glass transition or melting point, °C	1175	265	245
Thermal conductivity, W/m°C	1.38	0.628	0.2
Thermal expansion coefficient, 10^{-6}/°C	0.55	17.2	15
Young's Modulus, GPa	70	58.3	21.5
Density, g/cm^3	2.20	4.33	4.88
Refractive index	1.455	1.499	2.9
at (λ, μm)	(0.7)	(0.589)	(10.6)
dn/dT, 10^{-5}/°C	+1.2	-1.5	+10
at (λ, μm)	(1.06)	(1.06)	(10.6)
Transmission range, μm	0.24-2.0	0.25-4.0	4-11
Loss at 2,94 μm, dB/m	~800	0.08	5
Loss at 10,6 μm, dB/m	NA	NA	2
Property	**Crystal**		**Hollow**
	PC	**SC**	**Hollow Silica**
Glass transition or melting point, °C	412	2030	150 (usable T)
Thermal conductivity, W/m°C	1-1	36	1.38
Thermal expansion coefficient, 10^{-6}/°C	30	5	0.55
Young's Modulus, GPa	0.14	430	70
Density, g/cm^3	6.39	3.97	2.20
Refractive index	2.2	1.71	NA
at (λ, μm)	(10.6)	(3.0)	
dn/dT, 10^{-5}/°C	-1.5	+1.4	NA
at (λ, μm)	(10.6)	(1.06)	
Transmission range, μm	3-16	0.5-3.1	0.9-25
Loss at 2,94 μm, dB/m	3	0.4	0.5
Loss at 10,6 μm, dB/m	0.5	NA	0.4

5 Measurement Results

5.1 Experiment

The presented measurements were conducted with FTIR spectrometers, (Bruker, type IFS-66 and Thermo-Nicolet, type Avatar). A schematic of Bruker spectrometer has already been shown in Figure 3.9. The spectrometer was operating in mid-infrared spectral range. For this purpose, it has been equipped with a ceramic light source. The light source was of a spiral shape and a length of 10 cm. A special water cooling of the light source was necessary. The emitted light was limited on an aperture and further collimated by a set of mirrors. After the collimation, the beam was directed to the Michelson-Interferometer. The Michelson-Interferometer was constantly purged with dry air heated up to 40°C. This preserved a KBr beam-splitter from destruction by the humidity contained in the air, as well as provided a smooth as possible shift of the movable mirror on the air cushion. Further, the modulated light was directed to the sample compartment. In a basic version of IFS-66, a sample is put into the spectrometer and the signal is collected by one of two optional detectors. For purposes of online measurements of lubricants, the spectrometer has been additionally equipped with an external port, focusing the light at the entrance of infrared fibers, leading to an ATR-probe. This arrangement enabled direct access to external samples. The ATR fiber-optic probe was purchased from Remspec Corporation, which has been marketing fiber-probes since 1993 [29, 30, 31, 27]. A schematic of the spectrometer with the external fiber-optic port is illustrated in Figure 5.33.

The light from the spectrometer is directed to the external port by an additional mirror mounted before the sample compartment. The external port comprises a paraboloidal mirror focusing the beam onto the entrance of the fiber bundle. Generally, fiber bundles provide several times higher signal throughput than

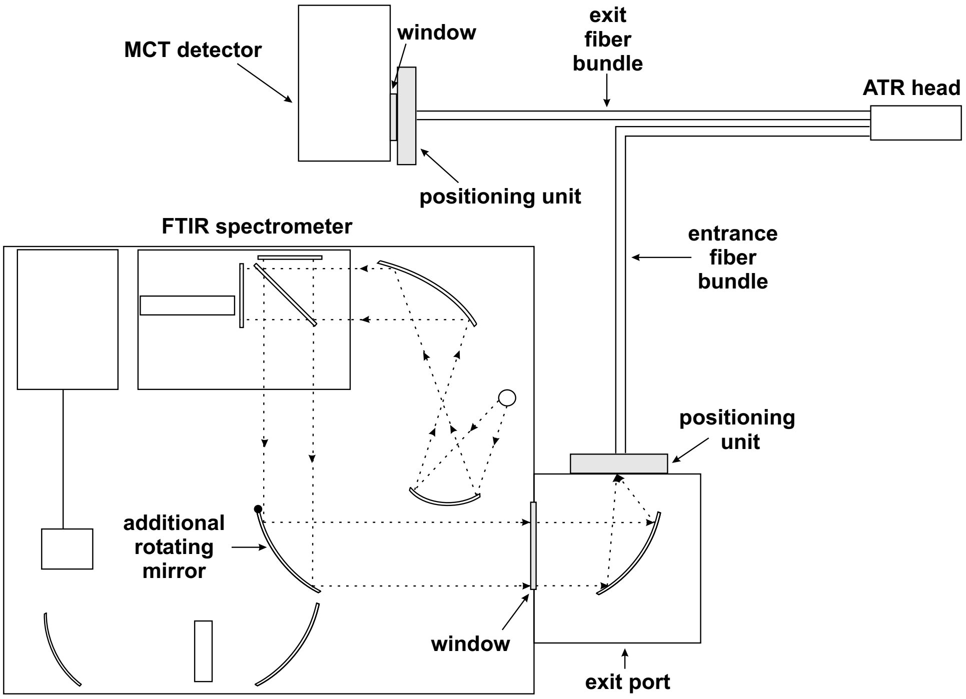

Figure 5.33: Schematic of the used measurement setup. IFS-66 FTIR spectrometer equipped with infrared fibers and an ATR-head.

throughput obtainable with single fibers. This is because of the small numerical aperture of single infrared fibers. The infrared fibers used were of chalcogenide type. Properties of chalcogenide glass fibers have been already described in section 4.3. The diameter of each fiber was 500 μm. Typical diameters of beams exiting spectrometers are 25-50 mm. Thus, focusing of the beam from the spectrometer onto the single fiber and simultaneously fulfilling the condition of numerical aperture is difficult. It causes high loses of the light intensity. On the contrary, a fiber bundle, demands only a focused light spot of the size of 2-3 mm. Additionally, the coupling of several single fibers with small diameters increased the mechanical stability and flexibility of the sensor head. Due to these facts, the used entrance fiber bundle consisted of seven single fibers spread accidentally in a glass cladding and enclosed in a metal jacket. The exact position of the focused light spot on the fiber bundle was found by the use of a 3D-positioning unit. Due to the strong attenuation of the light in the fibers, the length of the entrance fiber bundle was limited to 1 m. In this way, a sufficient light intensity at the detector was provided. A picture of a cross-section of the entrance fiber bundle is presented in Figure 5.34 b. The entrance fiber bundle leads to the ATR measurement head. The head consists of a ZnS crystal, in which the attenuation of the light, caused by the investigated sample, takes place. The attenuated light is further directed to the exit fiber bundle leading to an external MCT detector. Both entrance and exit fiber bundles were tightly coupled to the ATR-ZnS crystal. The coupling eliminated the necessity of additional antireflection coatings on the surface ZnS/fibers. The whole was enclosed in a stainless steel jacket. The jacket was specially designed, in order to preserve a sufficient cooling of the immersion probe. The special design of the ATR probe makes it appropriate for on-line investigations of chemical processes running under extreme conditions of temperature and pressure. Temperatures up to 150°C and pressures up to 7 bar can be applied. Nevertheless, in order to avoid melting the fiber-glass, the temperature of the fiber core must be kept below 50°C. This low temperature was guaranteed by a sufficient length of the ATR-crystal. ATR, mid-IR transparent, materials are good thermal insulators. Usually, with crystals of a few centimeters in length, a decrease of the temperature by 50°C is obtained. For certainty, an additional dry air or nitrogen cooling, of 140 l/min flow rates, was applied. The temperature inside of the cooling jacket was controlled by the use of a built-in thermocouple. A picture of the ATR crystal and the whole cooling jacket are presented in Figure 5.34 a and c, respectively [27]. The exit fiber bundle consists of twelve single fibers, due to the lower transmitted power of the light. Also, the length of the exit fiber bundle was shorter than the length of the entrance bundle. A proper position of the exit fiber bundle on the detector window, was found by the use of another 3D-positioning unit. The used fiber-optic probe can be easily adjusted to fiber-transmission or fiber-reflection measurements by exchange of the ATR-head.

The external detector module consists of a photoconductive Mercury Cadmium Telluride (MCT-HgCdTe) detector, a matched preamplifier and a power supply. An additional lens has been built into the detector window. The lens focuses the light exiting from the exit fiber bundle onto the detector element. It allows a smaller detector element to be used, as well as provides a better thermal isolation of the detector element from the surroundings. The detector signal is processed

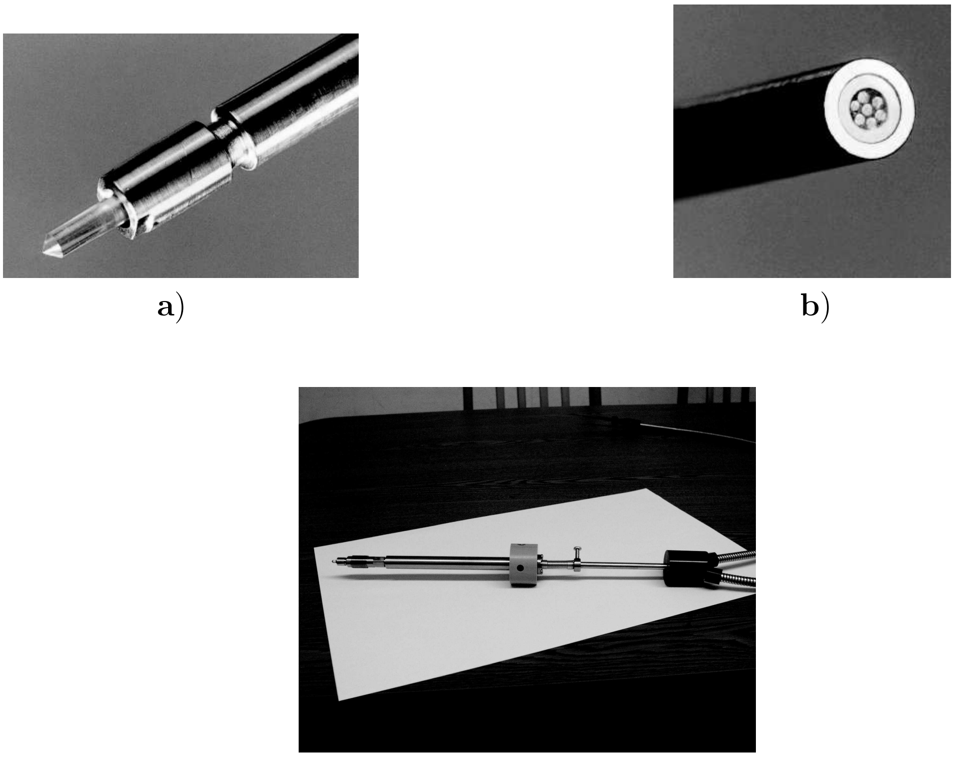

a) **b**)

c)

Figure 5.34: Components of the ATR-fiber-optic immersion probe: a) the head of the probe with the ZnS-ATR crystal, b) a cross-section of the entrance fiber bundle and c) the whole fiber optic probe.

by the electronic module of the spectrometer. The MCT detector requires cooling with liquid nitrogen. More or less stable operation of the detector module, sufficient for single measurements, is obtained one hour after it is switched on. In this time, the detector element must reach a thermal equilibrium and the electronics must warm up. The dewar for the liquid nitrogen had a 500 ml volume. The nominal holding time for the dewar was 12 hours, but in cases of long lasting, repeated measurements, the next filling should occur after 4-6 hours. It provides a reasonably constant temperature of the detector element.

The main parameters of the used MCT detector are listed below:

- Sensitive area: A = 0.25 mm^2
- Wavelength peak: $\lambda_p = 12.00\ \mu\text{m}$
- Detectivity: $D^*(\lambda_p, 10000, 1) \geq 4 \cdot 10^{10}$ $\text{cm}\sqrt{Hz}/\text{W}$

- Responsivity: R $\geq$ 5000 V/W
- Time constant: $\tau \sim 0.4$ μs
- Field of view: FOV = 60°

FTIR spectra of the light source collected with the fiber-optic probe differ from FTIR spectra collected in a traditional transmission measurement. In Figure 5.35 such two spectra collected with the IFS-66 spectrometer are presented for comparison. The upper plot has been recorded in transmission with a DTGS detector, in spectrometer purged with air, at 4 $\mathrm{cm^{-1}}$ resolution. The lower spectrum has been recorded with the MCT detector and the ATR fiber-optic probe, at 4 $\mathrm{cm^{-1}}$ resolution. In the lower fiber-optic spectrum a signal cut-off at longer wavelengths is observable. This feature is characteristic for chalcogenide glass fibers transmitting beyond 900 $\mathrm{cm^{-1}}$. The high wavelength cut-off of the used MCT detector has been adjusted to the cut-off of the fibers. An additional strong absorption at 2300 $\mathrm{cm^{-1}}$ originates from Se-H vibrations of the fibers, as mentioned in section 4.3. The hydrogen impurities originate from the production process of the fibers. Thus, chalcogenide fibers are not suitable for investigations of substances, whose spectral changes occur especially in this area. The influence of the response of the MCT detector on the spectrum is visible at high wavenumbers. A much stronger signal is measured in this area than with the DTGS detector. Additionally, variations of the signal, connected with insufficient vacuum in the dewar of the MCT detector, occur. In order to obtain spectra of good quality with an ATR-fiber-optic probe, some basic rules have to be followed. More scans than with traditional transmission measurements are necessary, due to the lower signal levels and a good contact between the surface of the ATR crystal and the probe has to be provided. Moreover, the position of the fibers should not be changed between the collection of background and sample spectra. The change in the position of the fibers influences the signal level due to microbending losses of the light intensity.

The ATR-head that was used is conically shaped. It operates as a cube corner reflector providing two bounces at the crystal/sample interface. The ATR-head, the light coupling between the spectrometer, the fibers and the ATR crystal are depicted in Figure 5.36. The light exiting the spectrometer is focused by a

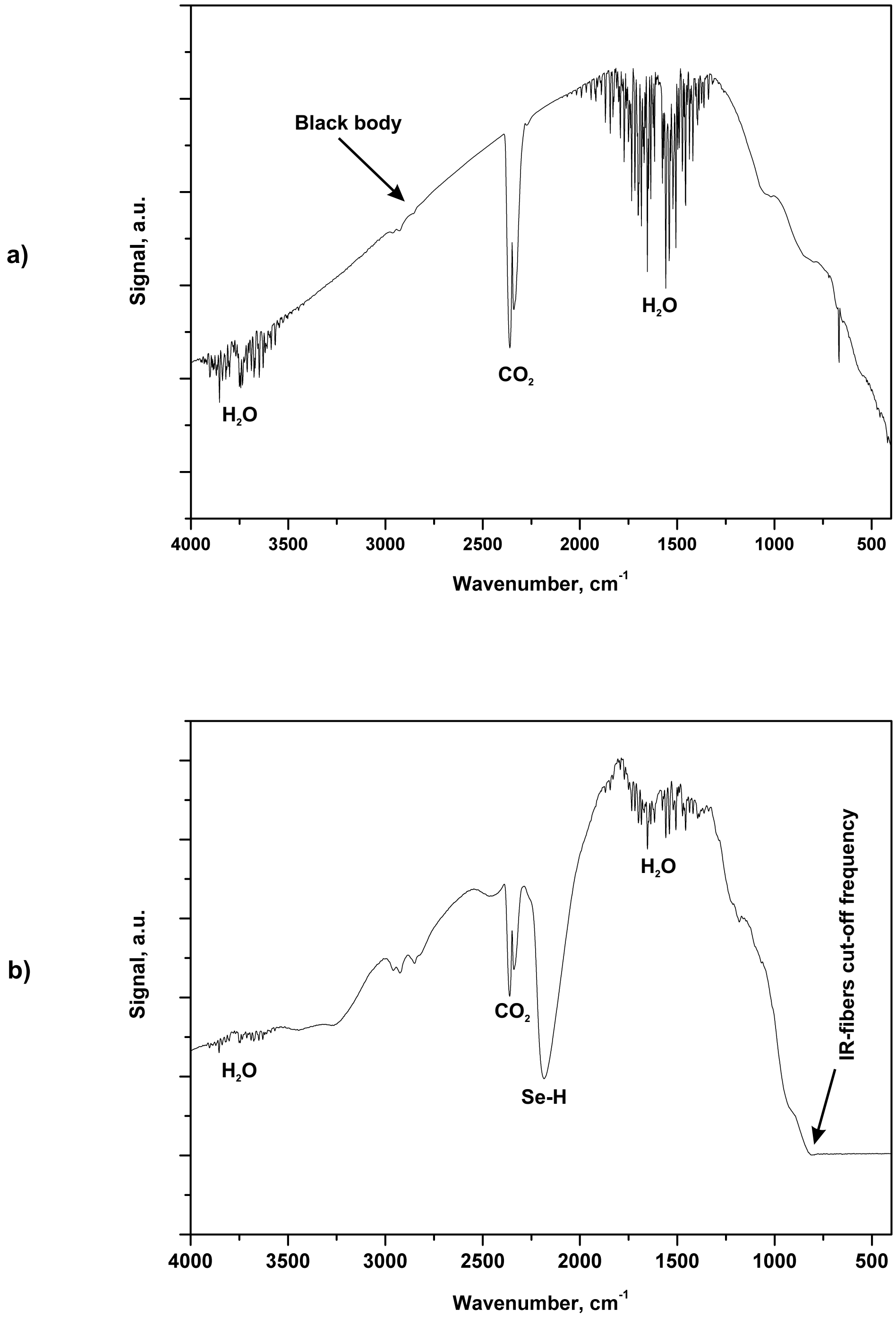

Figure 5.35: Comparison of FTIR spectra: a) recorded in transmission, b) recorded with infrared fibers. The fibers exhibit a cut-off frequency at 900 cm^{-1} and a strong Se-H absorption at 2300 cm^{-1}.

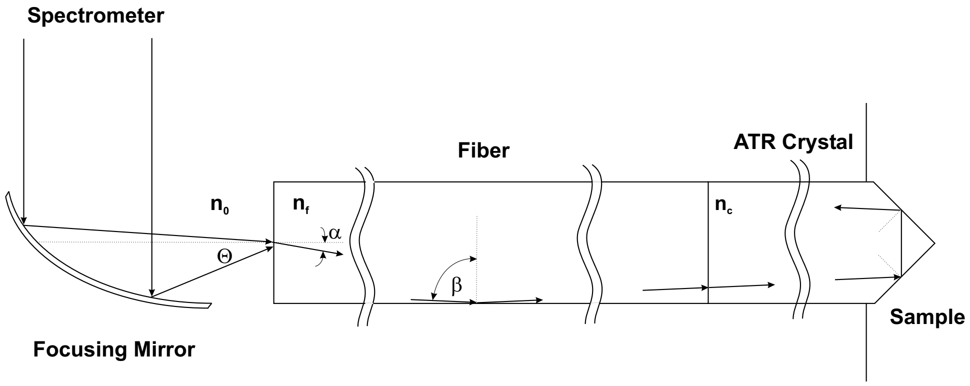

Figure 5.36: Schematic of the light coupling to the ATR-head. Only two reflections at the crystal/sample interface occur.

parabolic mirror at the entrance of the fiber bundle. The chalcogenide fibers have very high refractive index, $n_f = 2.8$, which remains almost constant in a wide wavelength range of infrared spectrum. Taking into consideration the reflective indices of the fiber core and the glass cladding, the acceptance angle of the fibers can be calculated. According to P. Melling, Remspec Corp., the acceptance angle of the used chalcogenide fibers is $\Theta = 40°$. This implies the reflection angle within fibers is higher than $\beta = 77°$. Due to negligible differences in refractive indices of chalcogenide fibers (2.8) and ZnS crystal (2.2-2.8, dependant on producers), little to no refraction of the light takes place on the surface fiber/ATR-crystal. Generally, reflection and refraction losses can be neglected under the condition of a tight contact between the fibers and the ATR-head. Due to this fact, it can be assumed that the light proceeds further in the crystal at a minimum angle 77°. Surfaces of the conical tip of the crystal are inclined at an angle of 45° to the rest of the crystal. This implies reflection angles at the surfaces of the tip smaller than 58°, but higher than 45°. Only the conical tip of the ATR-crystal stays in contact with the sample. Such a geometry provides only two reflections contributing to an infrared spectrum, as depicted in Figure 5.36. Nevertheless, measured absorbances are little larger than theoretical absorbances calculated for only two bounces. The reason for this is a wide range of angles, under which the light is transmitted inside of the fibers, as well as off-axis rays.

As mentioned in section 4.2, the strength of infrared absorption bands measured with ATR techniques depends on the relation between the refractive indices of the crystal and the sample. It influences the values of the penetration depth and the relative thicknesses of the system. Due to this fact, simulations of the effective thicknesses and the penetration depth for the used ZnS crystal and one of investigated lubricant samples have been conducted. Results of these simulations for relative effective thicknesses (d_e/d), parallel and perpendicular, calculated for thin film samples are plotted in Figure 5.37. Values of the relative effective thicknesses, corresponding to the plots, are collected in Table 5.8. As already mentioned, samples are considered to be in a form of thin films, if their thickness does not exceed a few wavelengths of the incident radiation. In the case of measurements carried out in mid-infrared spectral range, it means sample thicknesses in a range of micrometers. Due to the conical shape of the ZnS crystal, it was impossible to obtain a constant sample thickness of a few μm with this ATR-head in practice. Therefore, a further analysis has been conducted with samples in a form of bulk materials. Simulated relative effective thicknesses (d_e/λ_1) and the relative penetration depth (d_p/λ_1) for bulk materials are illustrated in Figure 5.38. Here λ_1 is the wavelength of the light within the ATR crystal. Corresponding values are listed in Table 5.9.

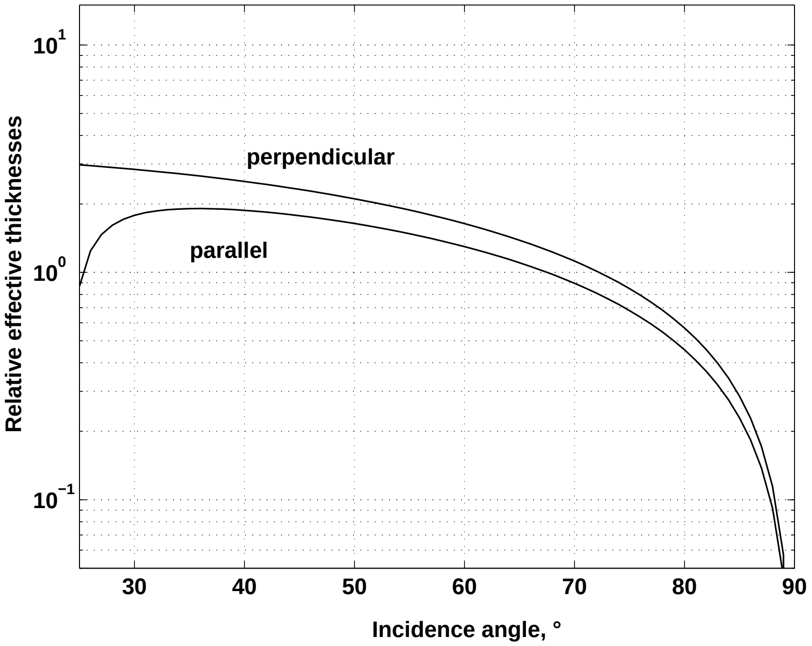

Figure 5.37: Parallel and perpendicular relative effective thicknesses (d_e/d) simulated for thin films. $n_{crystal} = 2.25$, $n_{oil} = 1.48$, $\lambda = 5.84$ μm, d = 2.596 μm - sample thickness.

Table 5.8: Relative effective thicknesses of thin film samples calculated for $n_{crystal} = 2.25$, $n_{oil} = 1.48$, $\lambda = 5.84$ μm, d = 2.596 μm - sample thickness.

Incidence angle, °	**Relative parallel effective thickness** $d_{e\|\|}/d$	**Relative perpendicular effective thickness** $d_{e\perp}/d$
30	1.782	2.839
35	1.907	2.686
40	1.875	2.512
45	1.777	2.318
50	1.641	2.108
55	1.479	1.881
60	1.298	1.639
65	1.103	1.386
70	0.896	1.121
75	0.679	0.849
80	0.457	0.569
85	0.229	0.286

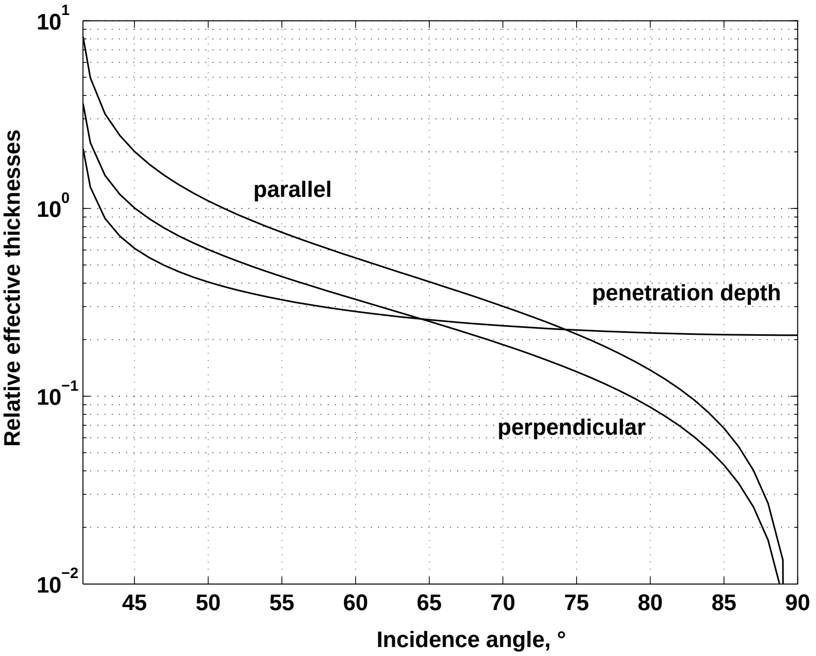

Figure 5.38: Parallel and perpendicular relative effective thicknesses (d_e/λ_1) and the penetration depth (d_p/λ_1) simulated for bulk materials. $n_{crystal} = 2.25$, $n_{oil} = 1.48$, $\lambda = 5.84$ μm.

Table 5.9: Relative effective thicknesses of bulk material samples and penetration depth calculated for $n_{crystal} = 2.25$, $n_{oil} = 1.48$, $\lambda = 5.84$ μm.

Incidence angle, °	**Relative parallel effective thickness** $d_{e\|\|}/\lambda_1$	**Relative perpendicular effective thickness** $d_{e\perp}/\lambda_1$	**Relative penetration depth** d_p/λ_1
45	2.011	1.006	0.613
50	1.097	0.604	0.405
55	0.746	0.434	0.326
60	0.545	0.328	0.283
65	0.407	0.250	0.255
70	0.301	0.188	0.237
75	0.214	0.135	0.255
80	0.138	0.087	0.217
85	0.067	0.043	0.213

From above, some general conclusions can be drawn:

- for the used measurement set-up the relative perpendicular effective thickness of thin films is higher than their relative parallel effective thickness. For samples in bulk materials form this relationship is the opposite.
- the measurement set-up does not differentiate between polarizations of the light i.e. the spectra are obtained as with the medium of average effective thickness in the range of reflection angles: 45°-58°. In this range the effective thicknesses of thin films are at a minimum, twice as big as corresponding thicknesses of bulk materials. That results in considerably weaker interaction between crystal and a sample and thus, weaker absorption bands in infrared spectra of bulk materials.
- for bulk materials at 45°: $d_{e\perp} = d_{e||}/2$

The influence of the effective thicknesses on FTIR spectra is demonstrated in Figure 5.39. From Figure 5.39 it is evident that the form of the sample does not influence the position of absorption bands, only their strength. In the spectrum of a bulk material sample, main hydrocarbon bands remain unchanged, but weaker spectral features, such as the one observable in the thin film spectrum in a range (1650-1700) cm^{-1}, are almost invisible. Due to this fact, on-line observation of the arising oxidation of lubricant samples, especially in its initial state, is expected to be difficult. A complete interpretation of spectra of lubricants is presented in section 5.3 of this chapter.

5.2 On-Line Aging Measurements

5.2.1 Measurement Set-up

In order to conduct on-line aging measurements, the aging process of different lubricants has been conducted. The lubricants were placed in a glass and heated to over 100°C. Exact aging conditions of particular samples are described in

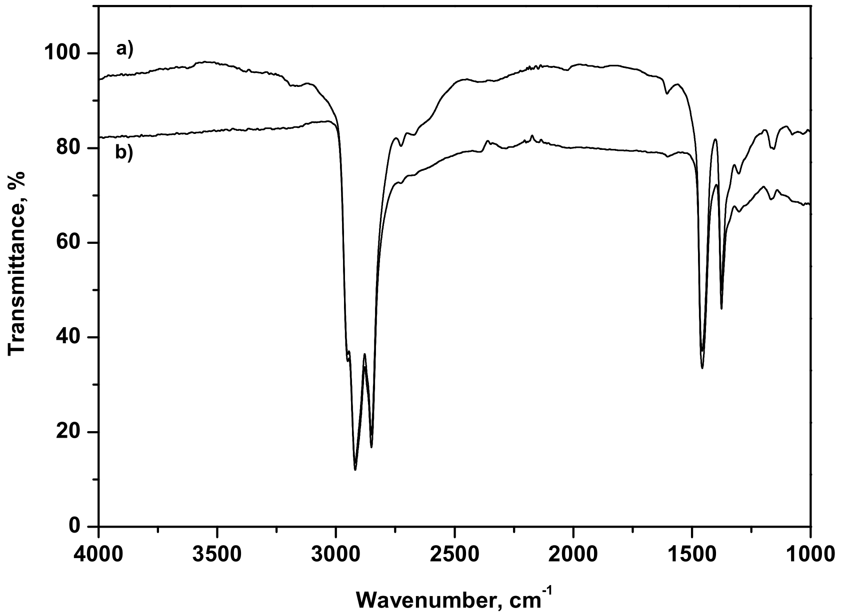

Figure 5.39: Sample transmittance spectra of a mineral oil measured for: a) thin film sample, b) bulk material sample.

section 5.3. The oxidation process was catalyzed by Cu and Fe powders, Sigma-Aldrich. Additionally, air at 1 bar, was constantly blown through the samples. The reaction times were on the order of months. During this period of time, a constant operation of the FTIR-spectrometer and the MCT detector had to be maintained. Therefore, laboratory conditions were constantly controlled. Stable operation of the MCT detector required a special system for automatic filling with liquid nitrogen. This developed system is described in the next subsection. Measurements were conducted with a specially written program working in the environment of OPUS, a software controlling the IFS-66 spectrometer - Bruker. The measurement software is described in subsection 5.2.3. In Figure 5.40, a picture of the constructed measurement set-up is shown. In the center of the picture, the IFS-66 spectrometer is shown. On its right side, the external port and the fibers have been placed. Behind the spectrometer, the glass containing oil samples with the immersed ATR-head and air connections is situated. On the right side, the specially adjusted MCT detector and the liquid nitrogen filling unit are situated.

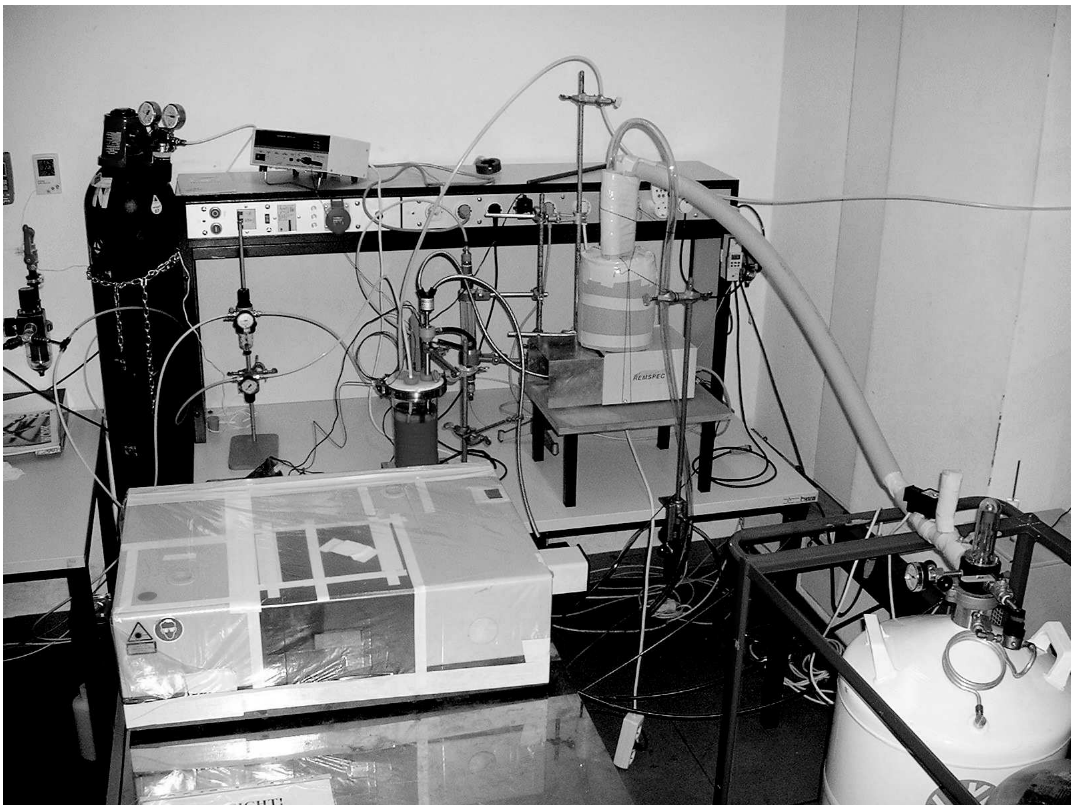

Figure 5.40: Measurement set-up used for on-line aging measurements. FTIR IFS-66 spectrometer equipped with infrared fibers and the ATR-head immersed in a boiling oil. On the right side, the cooling system of the MCT detector is situated.

5.2.2 Detector Stability

In order to conduct long-lasting measurements, the long-term stability of the MCT detector response had to be reached. As already mentioned, the detector body was sealed into a side sight 500 ml dewar of a holding time of 12 hours. The filling inlet of the dewar was 1 cm in diameter. Automatic filling of the detector dewar succeeded through a steel pipe placed in the inlet. In order to prevent high pressures form arising inside the detector, no gaskets at the inlet were used. The pipe was connected to a 35 l dewar through a 1,5 m long, PTFE (polytetraflouroethylene) tube. Connections and the pipes were thermally isolated. First, the time behaviour of the detector and its dewar were measured. For this purpose the hot detector was fully filled with the liquid nitrogen and the total signal was measured. The results are depicted in Figure 5.41. The detector signal becomes stable after about five hours since the initial filling. Therefore, evaluations of the efficiency of different automatic filling systems were always made 5 hours after the first filling.

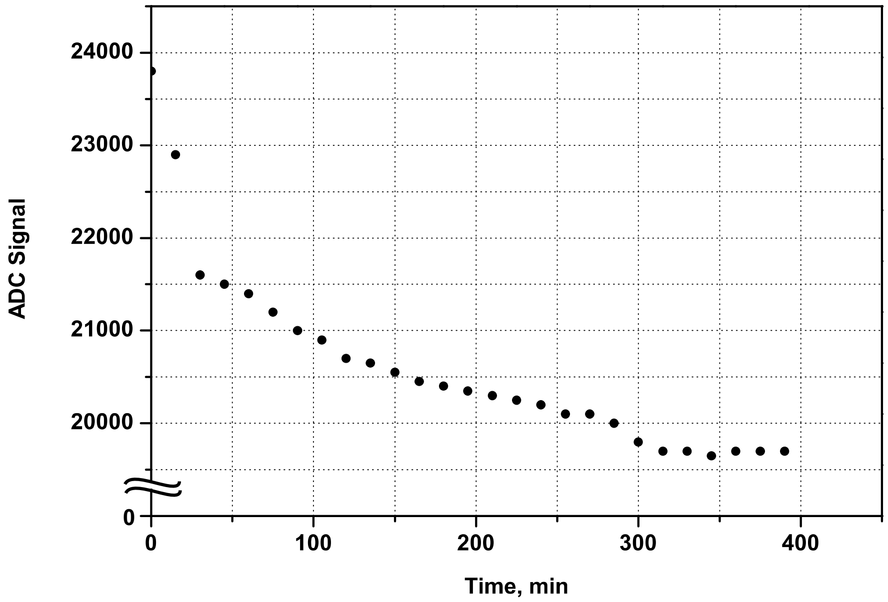

Figure 5.41: Cooling curve of the used MCT detector.

Two filling systems were investigated. The first was a two-diode filling-sensor offered by Cryo-Anlagenbau GmbH. Two light emitting diodes were immersed in the dewar at some distance from each other. A difference between power consumptions of the diodes, depending on their temperatures, served as an indicator of the level of the liquid nitrogen. The differential signal controlled the open/close function of the magnetic valve. This filling system is depicted in Figure 5.42. Two sensors with different distances between the diodes were investigated. If the distance between the diodes was 3.5 cm, the filling occurred cyclicly, every 30-40 s, with durations of 5-10 s. In this case the consumption of the liquid nitrogen was enormous. Therefore, the distance between the diodes was increased to 8 cm. In this case the filling occurred every few minutes for 20-90 s, one hour long. Afterwards, about one hour long break occurred. Due to small distances between the filling pipe and the diodes, limited by the diameter of the inlet, cooling of the diodes while the filling occurred. It caused irregular and small filling intervals.

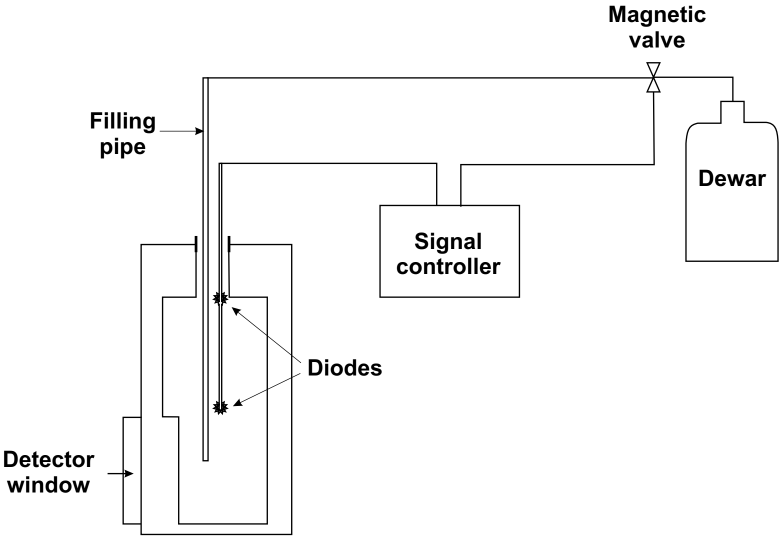

Figure 5.42: Two-diode liquid nitrogen filling system of Cryo-Anlagenbau GmbH.

In this set-up 35 l of liquid nitrogen were consumed in 16-17 hours. It means a weakly consumption of 365.5 l of the liquid nitrogen. This amount, though smaller than the one consumed by the first sensor, already requires special safety and ventilation systems. Costs of the liquid nitrogen and the necessary systems were too high to implement this filling system. It has to be, however, emphasized that this system works properly for detector dewars of bigger volumes and inlet diameters.

Next, the applicability of a time-relays was checked. It has been figured out that to fill the dewar to 2/3 of its volume, 1 min filling time was necessary. The time-relays was programmed to fill every 1, 2 or 3 hours, each time for 1 minute. In the case of hourly filling, the detector was quickly overfilled. In case of filling every three hours, after 23 hours all nitrogen from the detector evaporated and there was no signal measured. The most suitable filling interval was the filling every two hours. In this case, the detector was constantly cooled up to 30 hours with 35 l of the liquid nitrogen. That equates to half of the weekly consumption of the liquid nitrogen as compared with the above method or 196 l. Nevertheless, the consumption of the liquid nitrogen varies dependently on the ambient temperature. Fixed filling intervals therefore threaten to under-or overfill the detector and thereby destroy the infrared fibers coupled to the detector. Due to this fact, a PC-controlled filling system was developed. The goals of this system were:

- further reduction of the amount of the used liquid nitrogen
- preservation of a full safety while filling

A constant control over the filling process can be obtained by a direct use of the signal from the FTIR spectrometer. The signal was measured by a specially written program, in OPUS. The program for repeated long-term measurements is described in the next subsection. Interferograms collected with this program were sequently read into another LabView program communicating with a PCI card, National Instruments PCI-MIO-16E-4. The PCI card controlled the magnetic valve. In the program a maximum of each interferogram was found and compared with a set lower limit. If the measured maximum decreased under the set limit, the magnetic valve was opened. The duration of the filling process was fully adjustable. The set limit defined the shift of the base line in the FTIR spectrum and the amount of the consumed liquid nitrogen. For the best performance, a compromise between small changes of the measured maximum of the interferogram and long time intervals between the fillings had to be met. Eventually, changes in filling parameters could be conducted anytime without influencing conducted measurements. This solution reduced further the amount of the consumed liquid nitrogen and simultaneously preserved the maximum safety. A flowchart of the programmed procedures is shown in Figure 5.43. In Figure 5.44 example minimum and maximum transmission curves of the MCT detector, measured over seven days, are presented. The limit was set 2.5 % under the initial value of the maximum of the interferogram. From Figure 5.44 it is evident that with time, only a small shift of the transmission line, occurs. No other spectral changes, except of CO_2 absorptions, occur. Obtained long-term stability of the MCT detector was sufficient for long-term investigations of lubricants. With this set-up a further reduction of the amount of the weekly consumed liquid nitrogen to 59 l was obtained. The developed system fully fulfilled the set requirements.

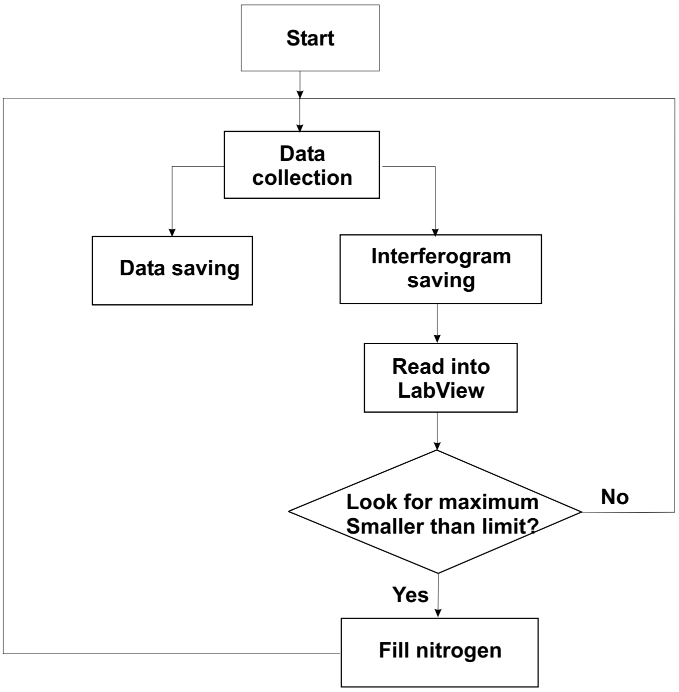

Figure 5.43: Flowchart of the filling control software.

5.2.3 Measurement Software

Basic measurements with IFS-66, as well as data processing are conducted in OPUS, Bruker. Due to various possible configurations of the FTIR-spectrometer and its couplings to external devices, before a measurement a precise configuration of the optical bench of the spectrometer and the electronics has to be defined in the software. The following parameters have to be set:

- spectral resolution
- spectral range
- measurement duration
- aperture
- measurement path
- detector
- mirror velocity
- acquisition data range
- acquisition mode
- low-pass filter

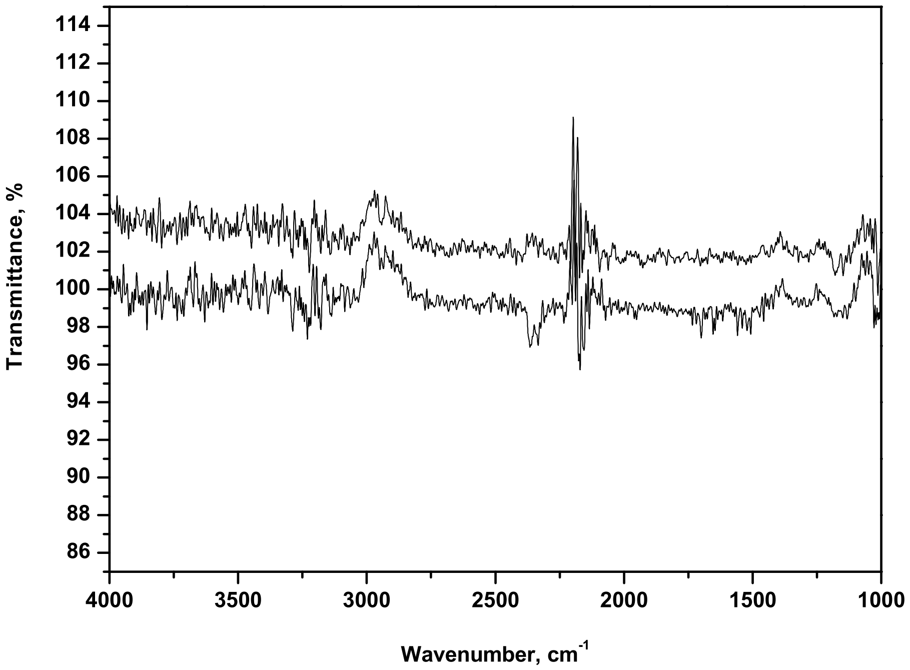

Figure 5.44: Minimum and maximum base line signal gained during seven days of a measurement with the PC controlled filling system.

- phase resolution
- phase correction method
- apodisation function
- zero filling factor

A choice of single components of measured and processed data, which should be available after a measurement, is also possible. Separate OPUS's functions are responsible for single and repeated measurements. In case of repeated measurements the amount of iterations N and the time interval between two single measurements Δt, have to be additionally set. The OPUS's function for repeated measurements exhibits, however, a series of disadvantages:

- the amount of measurements N, is limited to 1000
- the time interval between measurements Δt, is limited to 1000 s
- the data is not available before the end of the whole measurement
- OPUS cannot work parallel during one measurement

The first two points determine the duration and the time resolution of an investigated reaction. In case of conducted on-line measurements of lubricant aging the above limits of N and Δt, were too small. The necessary minimum measurement duration $N\Delta t$, was on the order of three months. By cases of such long-lasting measurements, the time interval had to be adjusted so as not to overload the hard disc of the PC and simultaneously not to lose the time resolution of the reaction. Time intervals of 20 min were chosen. Longer time intervals would not influence the time resolution of the measurement, due to very low initial reaction rates, but could influence the operation of the liquid nitrogen filling system. The inaccessibility of measurement results until the end of the whole repeated measurement threatened a waste of time, in cases of improper parameter settings influencing the results, or in cases of possible disturbances occurring during the measurement, which would make measurements useless. Due to these facts, a special program for repeated measurements providing enough duration, resolution and safety has been written.

In order to adjust the measurement process to any application, OPUS offers a possibility of writing programs in OPUS'own macro programming language, or in Microsofts VBScript. The OPUS macro system, consists of an editor, a debugger and a converter to translate macros written with OPUS-OS/2. OPUS possess a set of already programmed macros for basic operations on the data, which can be used for building more complicated functions. The advantage of the OPUS macro language is its simplicity in communication with the spectrometer. The communication with the spectrometer is controlled by a row of parameters, which have to be properly defined if the measurement should be controlled by an external program. A proper definition of these parameters makes external programming extremely difficult. On the contrary, in OPUS'own macros the parameters are already predefined. Therefore, controlling of measurements with the use of internal OPUS's macros is recommended. Nevertheless, a disadvantage of OPUS's macros is still the inaccessibility of the data, until the end of the measurement. Additionally, OPUS is blocked as long as macro is running. Therefore, a better solution is a combination of OPUS's macros with each other by interfacing with Microsoft's Scripting Engine, which is able to process several scripting languages. As a result, several programming languages can be used in combination with OPUS. Currently, VBScript is the most commonly used language, but Java Script can also be used. There are no limitations to the design of the user's interface, which is constructed with the help of Microsoft Forms. As usual, a Form is constructed interactively. A combination of OPUS's internal macros and VBScripts enables realization of parallel measurements and data processing, as well as an immediate access to the measured data during the measurement.

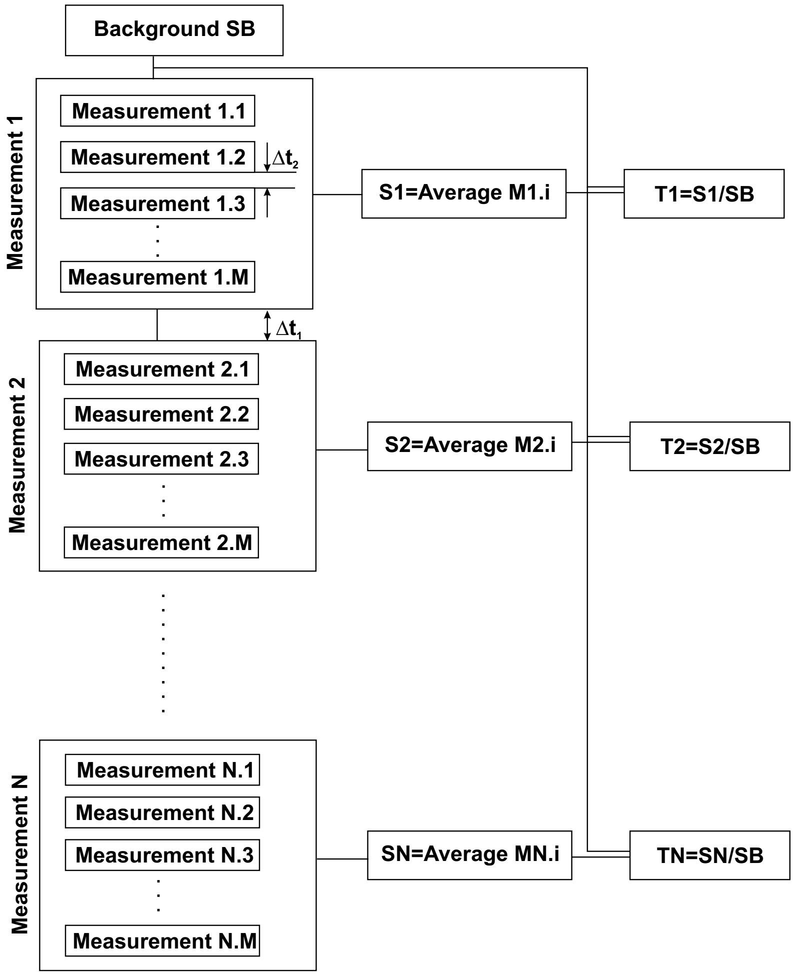

Figure 5.45: Structure of the program for long-lasting repeated measurements. S - spectrum, T - transmittance.

The program for repeated measurements as written is characterized by four parameters: a) number of main repetitions N, b) time interval between the main repetitions Δt_1, c) number of repetitions within one main measurement M and d)

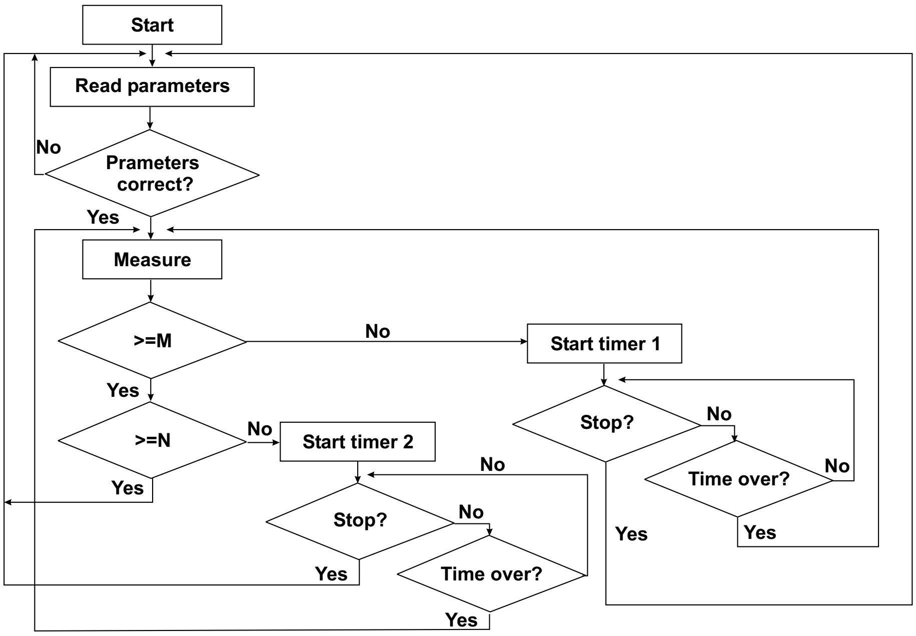

Figure 5.46: Flowchart of the Visual Basic/OPUS macros program for a control of long-lasting repeated measurements.

time interval between the minor repetitions Δt_2. Measurement results collected during each major repetition are averaged in order to increase SNR and eliminate possible disturbances originating for example from filling of the detector. The main repetition parameters N and Δt_1, correspond to the parameters set in OPUS's repeated measurement macro. Measurements follow the same way as standard FTIR transmittance measurements. At first a background spectrum, SB, is recorded. It serves to calculate transmittance spectra, T, after each single sample spectrum measurement, S. The program fulfills following functions: a) read and check parameters: N, M, Δt_1, Δt_2, b) conduct the measurement (one background and N sample spectra), c) calculate transmittances, d) stop the measurement and finally e) save the data. The configuration of the optical bench and the electronics of the spectrometer is predefined in OPUS's macros called out in the main VBScript. The data is saved in two separate folders. One folder contains the data available during the measurement. This data can be parallel processed freely. The second folder contains the original data, which is not available before the end of the measurement. The structure of the program is shown in Figure 5.45.

5.2.4 Temperature Correction

On-line interpretation and qualification of the aging process of lubricants demands comparison of spectra of aged lubricants recorded at elevated temperatures with spectra of fresh lubricants recorded at ambient temperature. Such spectra differ due to:

- a change of the emissivity of the sample
- a change in the refractive indices of both: the oil and the ATR crystal

In the presented thesis only the temperature dependant emissivity of samples has been considered. A total power, (spectral radiance) $L_{eD}(\overline{\nu})$, measured at the detector can be, for an emitting body, expressed by a sum of the transmitted power $L_{eT}(\overline{\nu})$ and the power emitted by the sample $L_{e\eta}(\overline{\nu})$:

$$L_{eD}(\overline{\nu}) = L_{eT}(\overline{\nu}) + L_{e\eta}(\overline{\nu}) \tag{5.164}$$

Transmitted spectral radiant power $\Phi_{eT}(\overline{\nu})$ can be calculated from:

$$T(\overline{\nu}) = \frac{I_T(\overline{\nu})}{I_0(\overline{\nu})} \cong \frac{\Phi_{eT}(\overline{\nu})}{\Phi_{e0}(\overline{\nu})} \cong \frac{L_{eT}(\overline{\nu})}{L_{e0}(\overline{\nu})} \tag{5.165}$$

where $T(\overline{\nu})$ is a transmittance of the sample according to 3.18. The emitted spectral radiant power is proportional to a geometrical coefficient κ, a spectral emission coefficient η and the spectral radiant power of a black body of the temperature T, $\Phi_{BB}(T, \overline{\nu})$ according to:

$$\Phi_{e\eta}(T, \overline{\nu}) = \kappa\eta\Phi_{BB}(T, \overline{\nu}) \tag{5.166}$$

Thus, the emitted spectral radiance $L_{e\eta}(T, \overline{\nu})$, calculated according to 3.29, is:

$$L_{e\eta}(T, \overline{\nu}) = \eta L_{BB}(T, \overline{\nu}) \tag{5.167}$$

With that, spectrum measured at the detector at the temperature T_i can be therewith expressed by:

$$L_{eD}(T_i,\overline{\nu}) = T(T_i,\overline{\nu})L_{e0}(T_i,\overline{\nu}) + \eta(\overline{\nu})L_{BB}(T_i,\overline{\nu}) \tag{5.168}$$

The emission coefficient $\eta(\overline{\nu})$ can be further determined by subtraction of spectra measured at two different temperatures T_1 and T_2, under condition of constant transmittances of the sample, $T(T_1,\overline{\nu}) = T(T_2,\overline{\nu})$:

$$\eta(\overline{\nu}) = \frac{L_{eD}(T_1,\overline{\nu}) - L_{eD}(T_2,\overline{\nu})}{L_{BB}(T_1,\overline{\nu}) - L_{BB}(T_2,\overline{\nu})} \tag{5.169}$$

Thus, under assumption that the transmittance $T_{meas}(T_i,\overline{\nu})$ measured at the temperature T_i is given by:

$$T_{meas}(T_i,\overline{\nu}) = \frac{L_{eD}(T_i,\overline{\nu})}{L_{e0}(T_i,\overline{\nu})} \tag{5.170}$$

the corrected transmission spectrum $T_{corr}(\overline{\nu})$ can be calculated according to:

$$T_{corr}(\overline{\nu}) = T_{meas}(T_i,\overline{\nu}) - \eta(\overline{\nu})\frac{L_{BB}(T_i,\overline{\nu})}{L_{e0}(T_i,\overline{\nu})} \tag{5.171}$$

A sample of measured and corrected spectra is shown in Figure 5.47. The measured sample was a GR-XP oil, which is a typical representative of industrial transmission oils used in stationary equipment. This is a mineral based oil containing small amounts of additives. The spectra were recorded at 6 cm^{-1} resolution and with 30 sample and background scans. In the upper plot, uncorrected spectra of the same sample recorded at a) 120°C and b) 40°C are presented. The background shift of the a) curve is of about 10 % of transmittance and at the low wavenumber edge, some distortion caused by the emissivity of the black body, is noticeable. In the lower plot, the same spectra after the temperature correction to 40°C are presented. In order to obtain the best matching of the spectra, the expression 5.171 must be corrected for an experimental factor of m.

$$T_{corr}(\overline{\nu}) = T_{meas}(T_i,\overline{\nu}) - m\eta(\overline{\nu})\frac{L_{BB}(T_i,\overline{\nu})}{L_{e0}(T_i,\overline{\nu})} \tag{5.172}$$

The best results have been obtained for m=0.85.

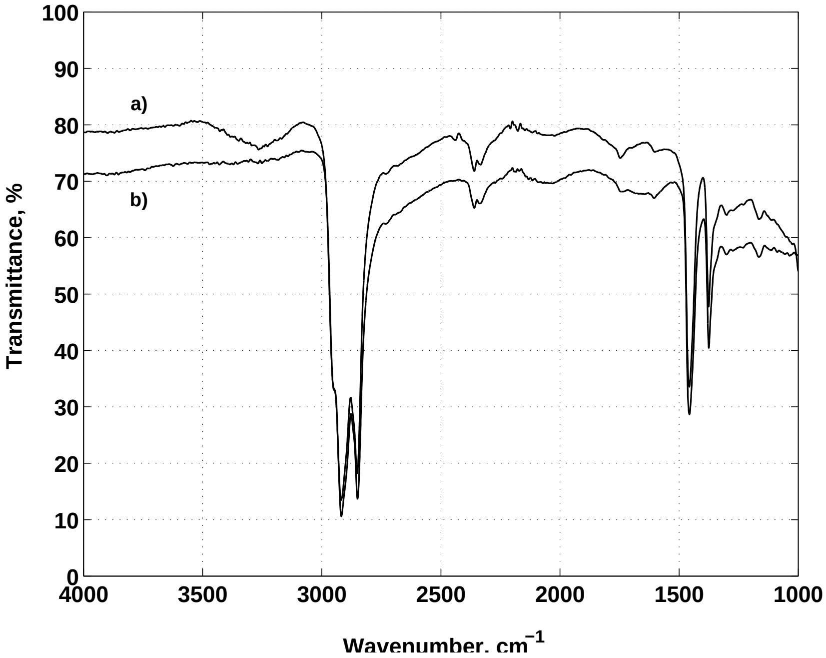

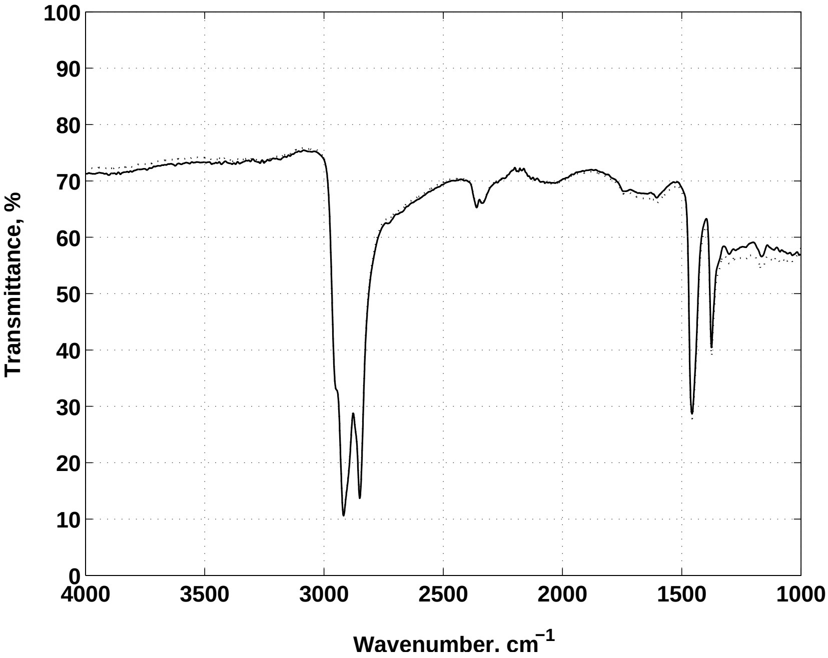

Figure 5.47: Upper plot presents the spectra of a GRXP oil measured at: a) 120°C and b) 40°C. Lower plot presents the same spectra, but the spectrum of the hot lubricant has been temperature corrected, m = 0.85.

5.2.5 Crystal Aging

The aging of lubricants and its on-line monitoring was conducted as already described. The ATR-head was immersed in hot samples and repeated measurements were conducted. A few hours after beginning the measurements, dependant on the aging temperature, a decrease of the signal level was observed, as illustrated in Figure 5.48. Usually, such a signal decrease is caused by a lack of the liquid nitrogen in the MCT detector. Another possible reason could be a change of spectral properties of the ZnS crystal under the reaction conditions. In order to investigate these eventual changes, an EDX analysis (Energy Dispersive XRF → X-Ray Fluorescence Analysis) of the crystal, has been conducted at the Institute of Hydrochemistry and Chemical Balneology (IWC) of the Technische Universität München. Obtained EDX spectra are shown in Figure 5.49 [107].

In XRF measurements, a primary X-Ray beam strikes a sample and excites a secondary X-Ray beam. The secondary beam is characteristic for the chemical composition of the sample. This is known as the phenomenon of *fluorescence*. The emitted wavelength depends on the chemical composition of the sample and the registered intensity on the concentration of particular atoms in the sample. XRF spectrometers are classified, with regard to their construction, as wavelength dispersive and energy dispersive spectrometers. In spectrometers of the first type the spectral resolution is obtained through diffraction of the resultant ray on a crystal. In energy dispersive spectrometers the spectral resolution is obtained directly through detector of a high energy resolution [107].

In Figure 5.49 a), an EDX spectrum of a new ZnS crystal is presented. Except for Ag traces, originating from other examinations of the crystal, clear strong peaks of Zn and S are observable. In the lower plot 5.49 b), an EDX spectrum of the damaged ZnS crystal is shown. In this case, the total number of counts decreased. This is due to the fact that the EDX technique investigates only the surface of the material up to 0.1 mm depth. In this area, the concentration of Zn and S decreased as atoms of Ni, P, Fe and Cu covered the surface. The presence of these atoms is responsible for introduced non-transparency of the crystal. Cu and Fe atoms were added as catalysts to the lubricant at the beginning of

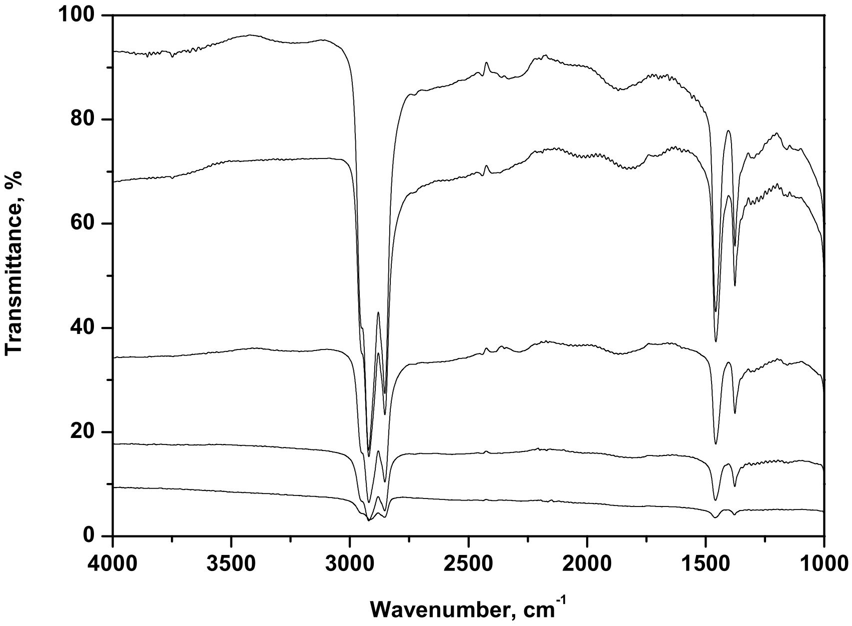

Figure 5.48: Decrease of the measured signal observed after 5 hours of on-line observation of the lubricant aging. Temperature of the reaction T = 120°C.

the aging process. Fe and Ni are constituents of the metal shaft of the ATR probe made of stainless steel. The P originates from the decomposition of ZDDP (Zinc Dialkyl Dithiophosphate) anti-wear additives being constituents of the investigated oil. Above results allow the claim, that the used ATR-probe can be used only for high temperature investigations of processes of high reaction rates. Long-lasting thermal exposures lead to the damage of the ZnS crystal being almost the most inert among all infrared materials. One solution of the problem with the ZnS crystal, could be a use of diamond ATR-crystal. Nevertheless, this material exhibits lower spectral sensitivity than ZnS crystal, due to lower values of penetration depths and effective thicknesses. Thus, more reflections on the crystal/sample, (new measurement geometry), interface would be necessary to obtain comparable signals. A second disadvantage of diamond is its strong infrared absorption occurring at 2000 cm^{-1} due to C-C vibrations of the tetrahedral diamond structure. At least, a fact that diamond is an expensive material should be taken into consideration.

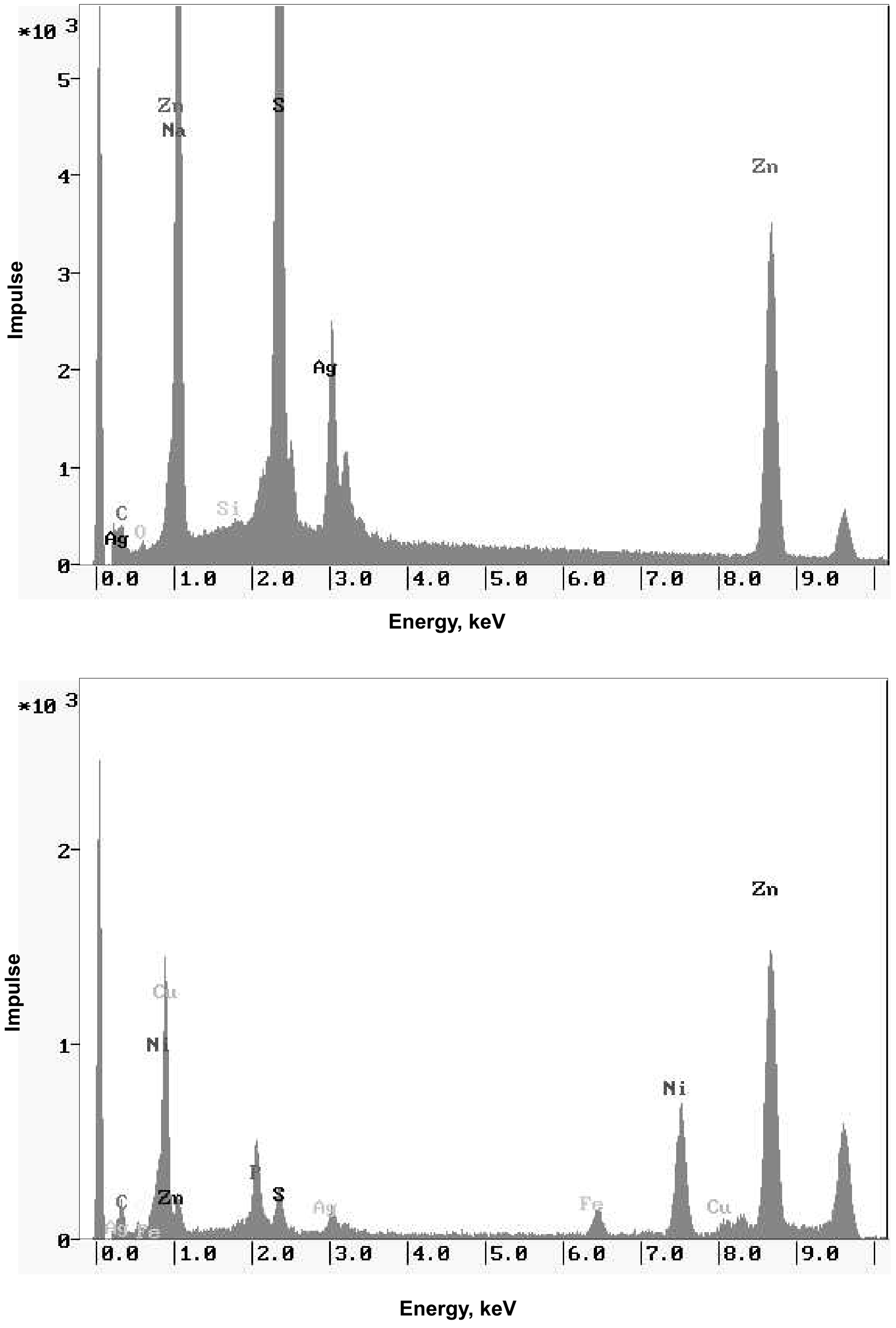

Figure 5.49: Comparison of EDX spectra: a) of a clean ZnS crystal (before on-line aging measurements), b) recorded after the decrease of the signal (after 5 hours of oil aging at 120°C).

5.3 Fresh and Aged Lubricants

5.3.1 Static Measurements

In order to check the sensitivity of the fiber-optic probe, four lubricating oils delivered by the Institute for Machine Elements, Gear Research Center of the Technische Universität München, have been static examined. The samples were measured in both transmission and using the ATR-technique. The oils were: mineral MTF (MTF-Manual Transmission Fluid), mineral PAO-ATF (PAO-Polyalphaolefine, ATF-Automatic Transmission Fluid), PG-CLP (PG-Polyglycol, CLP- a class of mineral oils with improved corrosion, aging and wear resistance) and PAO-Ester (AXLE) oil. Each oil sample was aged at 130°C, over 160 hours for the MTF oil and over 300 hours for the rest of the samples. The cold fresh and old oils were then investigated. Transmittance spectra were recorded with Thermo-Nicolet AVATAR FTIR spectrometer, at 4 cm^{-1} resolution, in (4000-400) cm^{-1} spectral range and with 30 background and sample scans. The spectra are plotted in Figures 5.50-5.53.

MTF oil is a fully natural mineral lubricant used in manual gearboxes for automotive applications. Its natural hydrocarbon structure is revealed by a strong absorption band in the area (2800-3000) cm^{-1} comprising of C-H asymmetric stretch and C-H symmetric stretch of CH_2 and CH_3 molecules. Due to a large sample thickness, these bands are strong and overlay. A second group of absorption bands, which can be assigned to the alkane chains are bands lying at 1377 cm^{-1} and 1456 cm^{-1}. They originate from CH_3 umbrella bends, CH_2 scissors, CH vibrational modes of short alkanes and a small amount of branched polymeric chains. The next relatively strong band occurs at 722 cm^{-1} with CH_2 rocking of longer alkane chains. Such chemical structure exhibit only high refined, thermal stable mineral oils. The MTF oil also contains trace amounts of antioxidants in the form of amine salt form compounds. They contribute to the broad band at (2800-3000) cm^{-1} and can be identified as separate bands at 1605 cm^{-1}, 1156 cm^{-1} and 818 cm^{-1}. And last, anti-wear additives in a form of esters are found. Their presence is evident at 1731 cm^{-1} in C=O stretching, in peaks of

C-C-O and O-C-C stretch at 1304 cm^{-1}, at 1166 cm^{-1} and lower wavenumbers, respectively. Despite the presence of absorption bands MTF oil contains only small amounts of esters. The chemical structure of the MTF oil limits its usefulness to applications with low loads and operating temperatures typically not exceeding 130°C [108, 109, 110, 111, 112, 38].

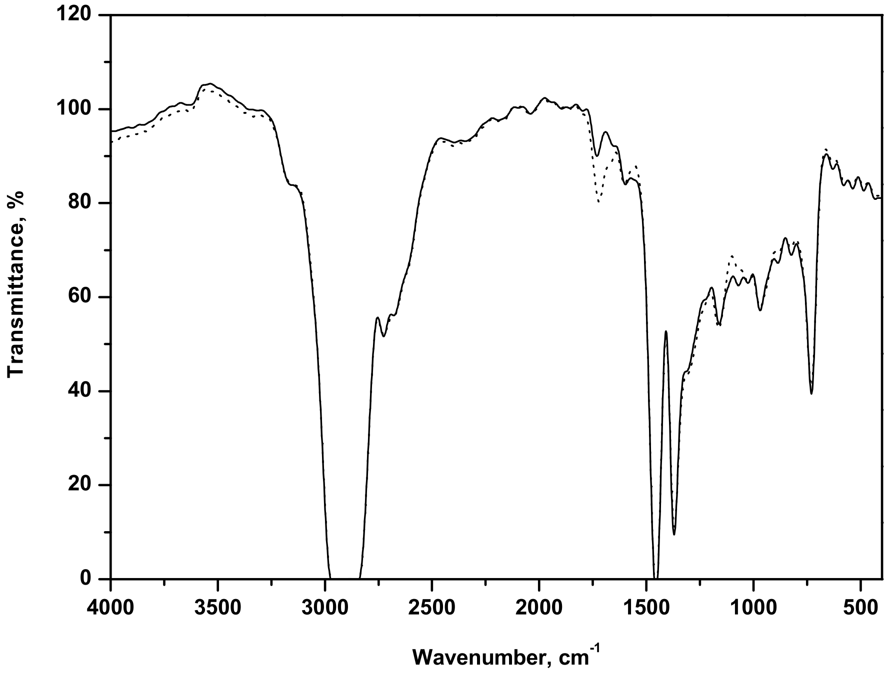

Figure 5.50: Comparison of transmittance spectra of MTF oil recorded with Thermo-Nicolet FTIR spectrometer: — fresh, ··· old (after 160 hours of aging at 130°C). Resolution $\Delta\overline{\nu} = 4$ cm^{-1}, sample thickness: fresh - 107.04 μm, old - 106.42 μm.

Spectra of the ATF oil are presented in Figure 5.51. This lubricant is a mixture of a fully synthetic polyalphaolefine (PAO) - 35 % and a mineral oil - 65 %. Due to this fact, its infrared spectrum differs only slightly from the spectrum of the MTF oil. The differences are visible in stronger bands from the additives, of which concentrations in ATF oils are usually higher. This enables the use of ATF lubricants at higher temperatures than pure mineral oils [108, 109, 110, 111, 112, 38].

In Figure 5.52 spectra of fully synthetic PAO-Ester oil (AXLE) developed for au-

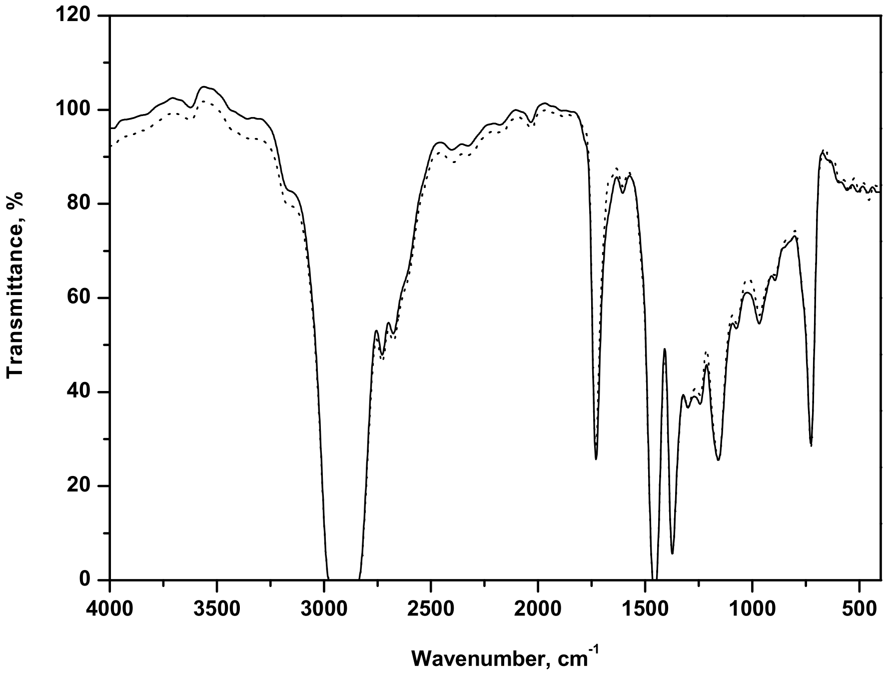

Figure 5.51: Comparison of transmittance spectra of ATF oil recorded with Thermo-Nicolet FTIR spectrometer: — fresh, ··· old (after 300 hours of aging at 130°C). Resolution $\Delta\overline{\nu} = 4$ cm^{-1}, sample thickness: fresh - 113.67 μm, old - 114.65 μm.

tomotive gears are shown. As mentioned previously, spectral features of polyalphaolefins are similar to these of mineral oils. Therefore, the well known hydrocarbon bands, together with strong ester and amine salt compounds bands at 1740 cm^{-1}, 1245 cm^{-1}, 1165 cm^{-1} and 1091 cm^{-1}, are observed. This oil exhibits a further improvement of lubricating properties in comparison to the MTF and the ATF oil. That is due to the saturated structure of the hydrocarbon chain, as well as, higher concentrations of additives [108, 109, 110, 111, 112, 38].

The last investigated sample was the PG-CLP oil. It is a polyglycol based oil developed for heavy load industrial applications. Its spectra, shown in Figure 5.53, differ from the spectra of the other samples. With this oil, the minimum obtainable sample thickness was still too large and therefore basic absorption bands are too strong. Additionally, strong, broad OH bands originating from polyglycol at 3500 cm^{-1} and 1100 cm^{-1} are visible. They cover other spectral features in the area (1500-1000) cm^{-1}. The typical hydrocar-

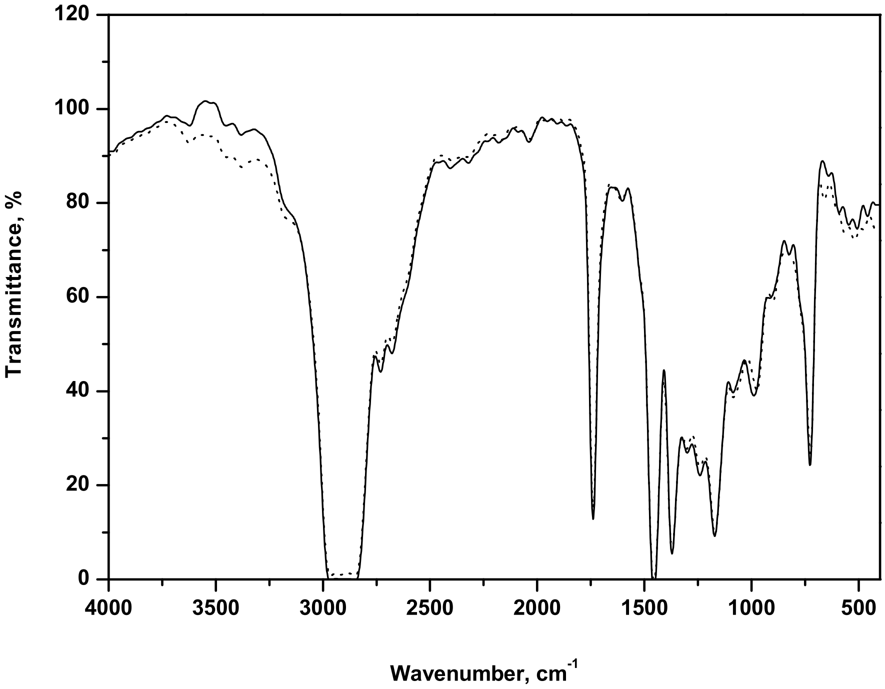

Figure 5.52: Comparison of transmittance spectra of PAO-Ester oil recorded with Thermo-Nicolet FTIR spectrometer: — fresh, ··· old (after 300 hours of aging at 130°C). Resolution $\Delta\overline{\nu} = 4$ cm^{-1}, sample thickness: fresh - 114.00 μm, old - 115.49 μm.

bon vibrations occur at standard wavenumbers. Nevertheless, the ratio between the intensities of these bands has changed. The peak at 1453 cm^{-1} is low indicating trace contents of simple alkane chains. Additionally, ethers, ketones, sulfur and phosphorus compounds, which are Extreme-Pressure (EP) additives, have been found. They contribute to the strong polyglycol band in the area (1300-800) cm^{-1} with S-O$_2$ asymmetric stretch at 1372 cm^{-1}, 1343 cm^{-1} and 1087 cm^{-1}. The minor peaks originate from esters, as anti-wear additives and anti-oxidants [108, 109, 110, 111, 112, 38].

It is hard to state and classify the deterioration of the investigated oil samples directly from comparison of the transmittance spectra. For this purpose, so called *subtraction spectra* have to be calculated. First, transmittance spectra have to be converted into absorbance spectra, which are then subtracted. In Figure 5.54 subtraction spectra of all four oil samples are plotted for comparison.

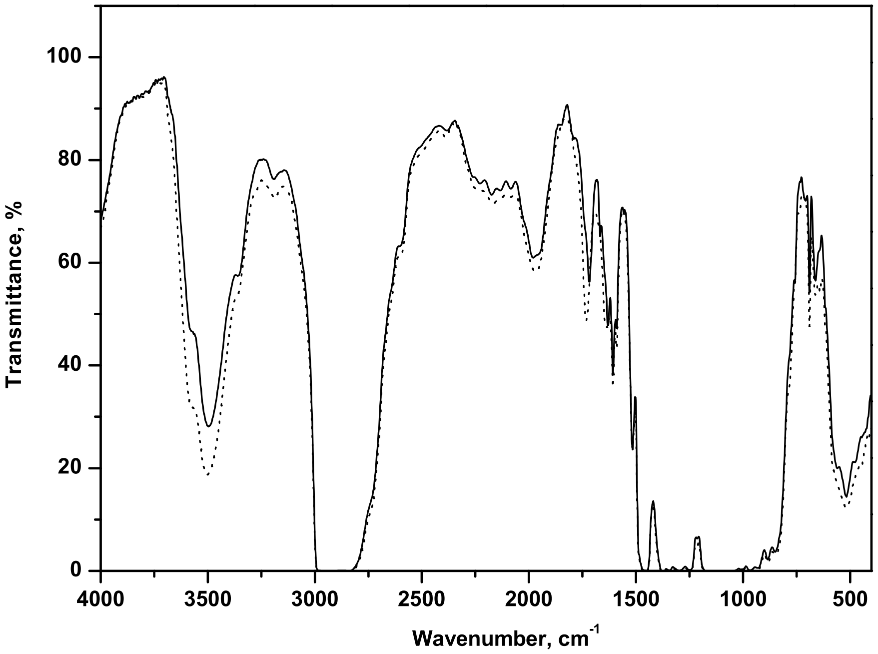

Figure 5.53: Comparison of transmittance spectra of PG-CLP oil recorded with Thermo-Nicolet FTIR spectrometer: — fresh, ··· old (after 300 hours of aging at 130°C). Resolution $\Delta\overline{\nu} = 4$ cm^{-1}, sample thickness: fresh - 111.26 μm, old - 126.04 μm.

The spectra are shifted in y-direction for better clarity. At higher wavenumbers (4000-3000) cm^{-1}, no structural change of the lubricants is made apparent, except in the PG-CLP oil. Strong, sharp lines, in the area of basic hydrocarbon vibrations, arise from slight variations of sample thicknesses of all fresh and old lubricants. For the same reason, a negative artificial band, in the spectrum of the PAO-Ester oil, occurred at 1717 cm^{-1}. For quantitative interpretation, a calibration of sample thicknesses is necessary, before calculation of subtraction spectra. In the subtraction spectrum of the MTF oil, a growth of the oxidation peak at 1712 cm^{-1} is observed. It overlays a minor peak at 1625 cm^{-1}. The products of the oxidation identified on the basis of the C=O stretching, are aldehydes and ketones. A row of negative bands at 1449 cm^{-1}, 1374 cm^{-1} and 1362 cm^{-1} imply the disposition of short alkane chains of the basic oil. The other small negative peaks at 1111 cm^{-1} and lower, arise from the consumption of anti-oxidative amines. As the structure of the ATF oil resembles that of the MTF oil, similar oxidative changes are expected. The subtraction spectrum of the ATF oil exhibits an oxidation peak at 1717 cm^{-1} and a better separated peak 1675 cm^{-1}. The peak at 1675 cm^{-1} is caused by higher concentrations of ketones with aromatic rings. There are no clear negative peaks of alkane decomposition in the area (1500-1200) cm^{-1}, due to the mostly saturated structure of the base oil and its better thermal stability. The visible negative peak in the spectrum of the PAO-Ester oil originates, as already mentioned, from different sample thicknesses. Therefore no oxidative changes of this sample could be observed. Lastly, the subtraction spectrum of the PG-CLP oil is, as usual, characterized by C=O stretch of aldehydes and ketones at 1727 cm^{-1}. Additionally, a decomposition of the polyglycol is visible as a growing band at 3500 cm^{-1}. In the case of this oil this decomposition is a better sign of the aging than the oxidation peaks. It has been noticed that for all four lubricants the spectral area between 1730 cm^{-1} and 1710 cm^{-1} is a common range indicating oxidation changes. Observation of this area should therefore be enough for the determination state of aging of a lubricant. In order to check the sensitivity of the fiber-optic probe, the same samples were measured with the ATR fiber-optic-probe.

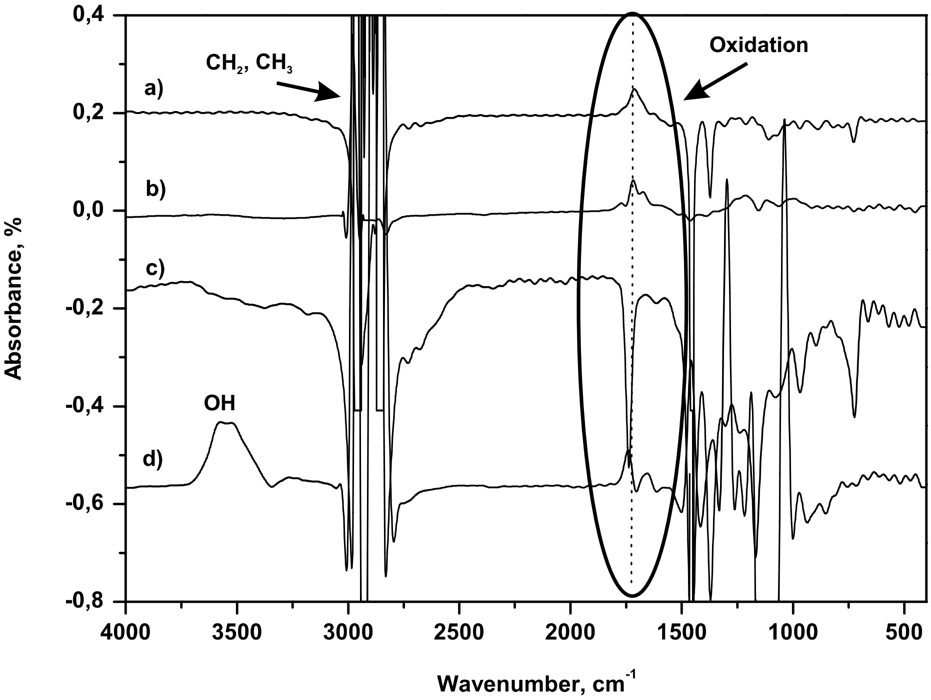

Figure 5.54: Comparison of subtraction spectra of: a) MTF, b) ATF, c) PAO-Ester and d) PG-CLP oils recorded with Thermo-Nicolet FTIR spectrometer.

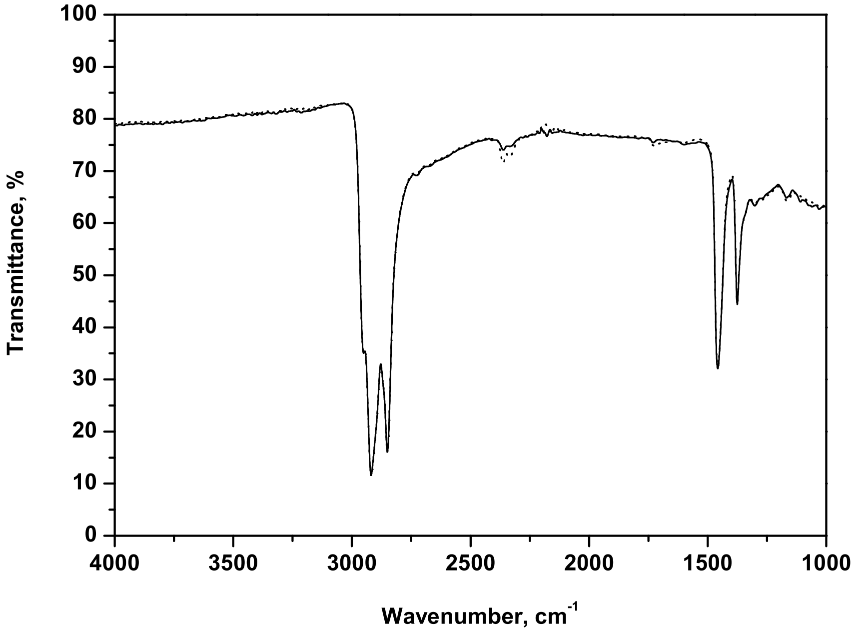

Figure 5.55: Comparison of ATR-fiber spectra of MTF oil recorded with Bruker FTIR spectrometer: — fresh, ··· old (after 160 hours of aging at 130°C). Resolution $\Delta\overline{\nu} = 6$ cm^{-1}.

The ATR spectra were recorded with a Bruker IFS-66 FTIR spectrometer, as described in section 5.2, at 6 cm^{-1} resolution, with 100 background and sample scans and using the Blackmann-Harris apodisation function. The spectral range of the measurement set-up was limited by the fibers to (4000-1000) cm^{-1}. Background spectra were measured in air. The measured spectra, presented in Figures 5.55-5.58 are similar to the transmittance spectra presented above. The absorption bands are however significantly weaker and oxidative changes of the samples are almost invisible. Therefore, similar to transmission measurements, fiber-subtraction spectra have been calculated.

Fiber-subtraction spectra are plotted in Figure 5.59. They are shifted in y-direction for better clarity. The fiber-subtraction spectra exhibit very small disturbances in the area of main hydrocarbon chains, in comparison to the transmittance spectra, due to the almost constant effective thickness for fresh and old oil samples at measurement angles. The problem of the sample thickness is thereby eliminated. The remaining small disturbances originate from slight

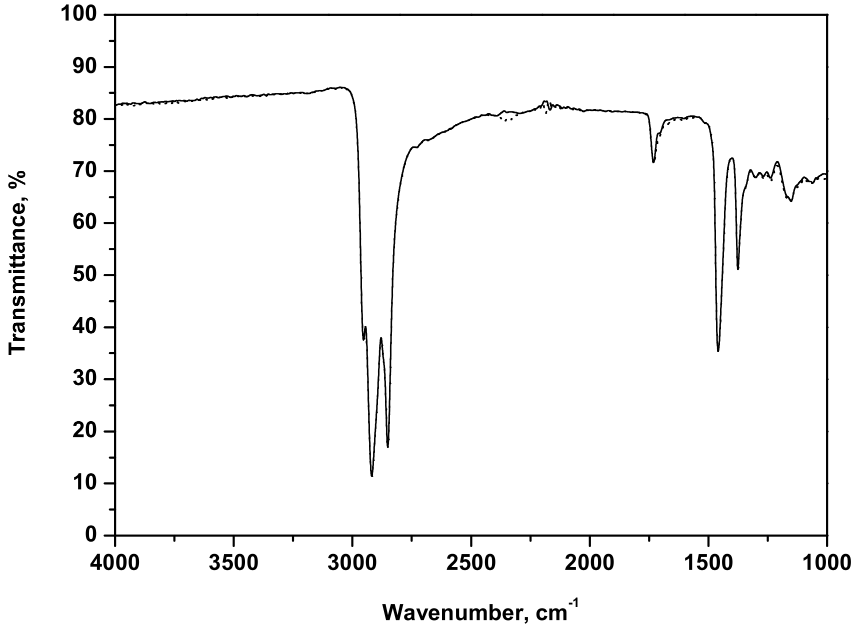

Figure 5.56: Comparison of ATR-fiber spectra of ATF oil recorded with Bruker FTIR spectrometer: — fresh, ··· old (after 300 hours of aging at 130°C). Resolution $\Delta\overline{\nu} = 6$ cm^{-1}.

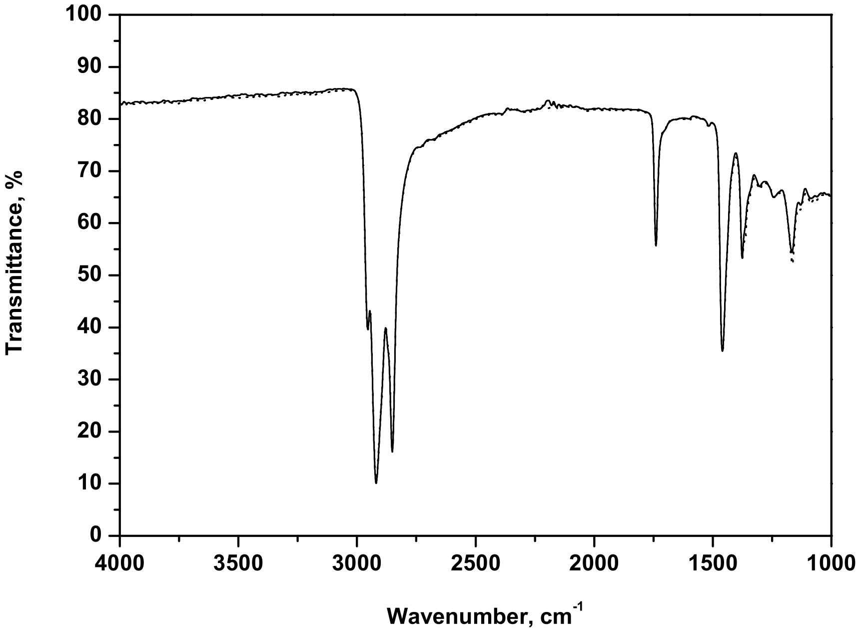

Figure 5.57: Comparison of ATR-fiber spectra of PAO-Ester oil recorded with Bruker FTIR spectrometer: — fresh, ··· old (after 300 hours of aging at 130°C). Resolution $\Delta\overline{\nu} = 6$ cm^{-1}.

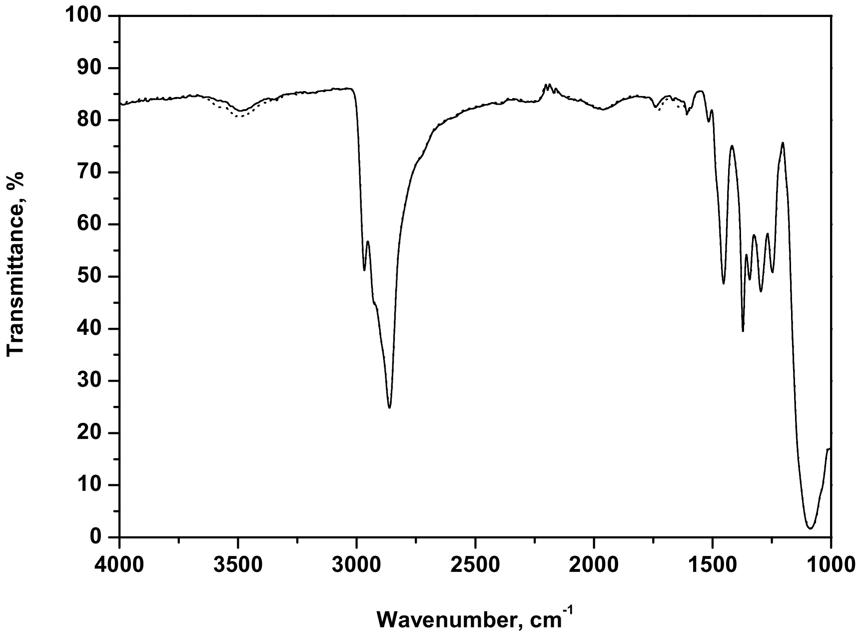

Figure 5.58: Comparison of ATR-fiber spectra of PG-CLP oil recorded with Bruker FTIR spectrometer: — fresh, ··· old (after 300 hours of aging at 130°C). Resolution $\Delta\overline{\nu} = 6$ cm^{-1}.

changes of refractive indices of the samples. Two bands at 2361 cm^{-1} and 2335 cm^{-1} originate from different CO_2 concentrations in the atmosphere of the spectrometer between the measurements. In the area of (2200-2000) cm^{-1}, strong peaks, originating from Se-H vibrations of the fibers, occur. All fiber spectra exhibit lower SNR values and lower amplitudes of the oxidation peaks than the corresponding standard FTIR-subtraction spectra, but their existence is still evident.

Amplitudes of the oxidation peaks obtained in transmittance measurements are much higher, but as already mentioned obtaining a good quality subtraction spectrum from transmittance measurements demands a calibration of the sample thickness. The values obtained in fiber-optic subtraction spectra are lower, but as depicted in Figure 5.59, identification of the oxidation process is unquestionable. It should be once again pointed out that this kind of measurement does not demand any sample preparation and the disturbances originating from unequal sample thicknesses are eliminated.

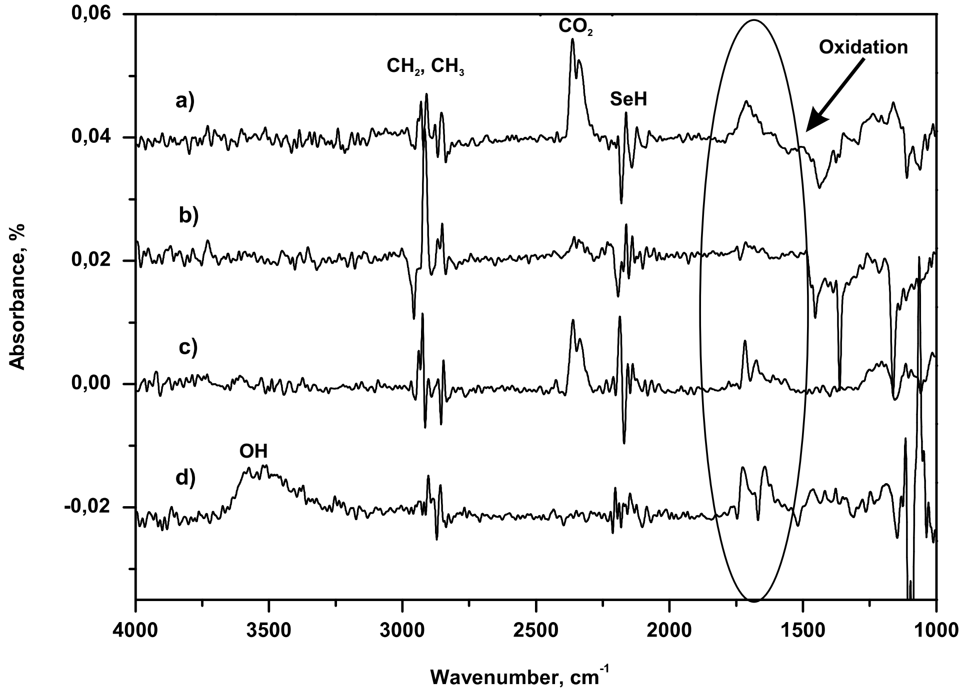

Figure 5.59: Comparison of ATR-fiber-subtraction spectra of: a) MTF, b) PAO-Ester, c) ATF and d) PG-CLP oils recorded with Bruker FTIR spectrometer. Resolution $\Delta\overline{\nu} = 6$ cm^{-1}, 100 scans.

It has been proven that the ATR fiber-optic FTIR measurements have sufficient sensitivity to detect an already aged lubricant. In order to find out how advanced deterioration of an oil can be readily identified, two fresh lubricants were aged in the laboratory. The samples were cooled down before measurements, in order to protect the ATR crystal. The lubricants were delivered by Deutsche Shell GmbH, which also conducted a standard laboratory analysis of the samples for comparison.

5.3.2 Aging Monitoring

The first sample was Shell Cassida Oil, type EHF 5700/2. It was a hydraulic oil enriched with detergents, HLPD - according to DIN 51524-2. One liter of the oil was aged at 120°C, in the set-up presented in Figure 5.40. The reaction was catalyzed by Fe and Cu particles, Sigma-Aldrich. Once per week ten grams of each metal powder were added to the oil. A total deterioration was observed after

Table 5.10: Change of selected properties of Cassida oil, Deutsche Shell GmbH.

Time, days	Kinematic Viscosity at 100°C, mm^2/s	Kinematic Viscosity at 40°C, mm^2/s	Total Acid Number, mgKOH/g
fresh oil	6.750	45.81	0.23
21	7.038	49.32	0.33
35	7.137	51.02	0.52
50	7.179	62.30	0.82
73	7.942	60.99	1.31
84	8.912	62.36	2.60

Time, days	Dielectric Constant	Refractive Index
fresh oil	-	-
21	2.22	1.4782
35	2.23	1.4768
50	-	1.4749
73	2.26	1.4790
84	2.32	1.4776

85 days of aging. In Table 5.10 results of standard laboratory tests, conducted at Deutsche Shell GmbH, are collected. Both kinematic viscosities, measured at 40°C and 100°C, increased about 36 % and 32 %, respectively. The kinematic viscosity at 40°C exhibited a bigger change earlier than the kinematic viscosity at 100°C. Similarly, the Total Acid Number and the dielectric constant increased. A conventional limit of the usefulness of an oil is reached when the TAN reaches the value of 2. This is the case of the last Cassida sample. Changes in the refractive index have not shown any regularity. The above results must be complimented with infrared spectra for a definite characterization.

Infrared spectra were measured both in transmission and with ATR-fiber-optic setup. In both cases, collected transmittance spectra were converted to absorbance spectra. Subsequently a baseline correction of the spectra was conducted. The Rubberband correction method with 250 correction points was applied. Then the resultant spectra were normalized to the range (0-100) %. The resultant absorbance spectra, in the area (1900-1500) cm^{-1}, are presented in Figures 5.60 and 5.61. The spectra do not exhibit any significant change for the

Table 5.11: Values of amplitudes and areas of the oxidation peak of Cassida oil calculated from its subtraction spectra.

Reaction time, days	**Peak amplitude, transm. at 1716 cm^{-1},** %	**Peak area, transm. in [1785-1653] cm^{-1},** $\% \cdot cm^{-1}$
21	0.181	13.541
45	0.464	26.360
73	2.500	139.564
84	15.593	797.858
Reaction time, days	**Peak amplitude, fibers at 1715 cm^{-1},** %	**Peak area, fibers in [1799-1649] cm^{-1},** $\% \cdot cm^{-1}$
21	0.168	11.251
45	0.441	23.243
73	0.724	39.221
84	1.512	82.032

samples aged 21, 35 and 50 days. From the 73 day old oil sample on, a rapid growth of the oxidation peak occurred. This result agrees with the results of laboratory analysis, which were carried out at Deutsche Shell GmbH [113]. According to Deutsche Shell GmbH, the sample aged for 73 days, already exhibits strong oxidative changes and the oil aged for 84 days should already have been exchanged. In order to conduct a quantitative comparison of transmission and ATR-fiber-optic measurement techniques, subtraction spectra have been calculated. Values of amplitudes and areas of the oxidation peak for both measurement techniques are listed in Table 5.11. Integration limits for both types of subtraction spectra are slightly different, but they were chosen according to the shape of the oxidation peak. The differences are negligible and do not influence the results. From Table 5.11 it is evident that standard transmittance measurements are about 11 times more sensitive than the ATR-fiber-optic measurements for Cassida oil.

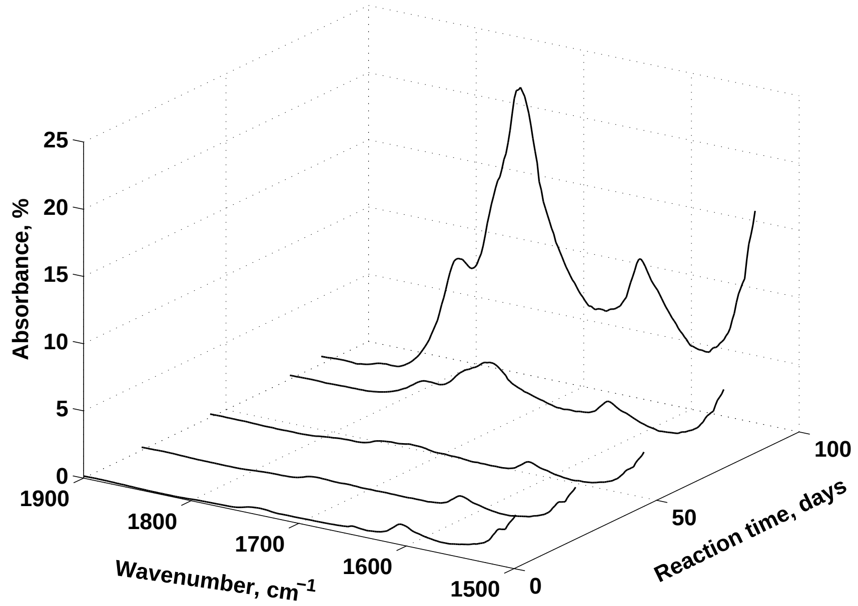

Figure 5.60: Growing oxidation peak in absorbance spectra of Cassida oil, recorded with Thermo-Nicolet FTIR spectrometer. Resolution $\Delta\overline{\nu} = 4$ cm^{-1}, 30 scans.

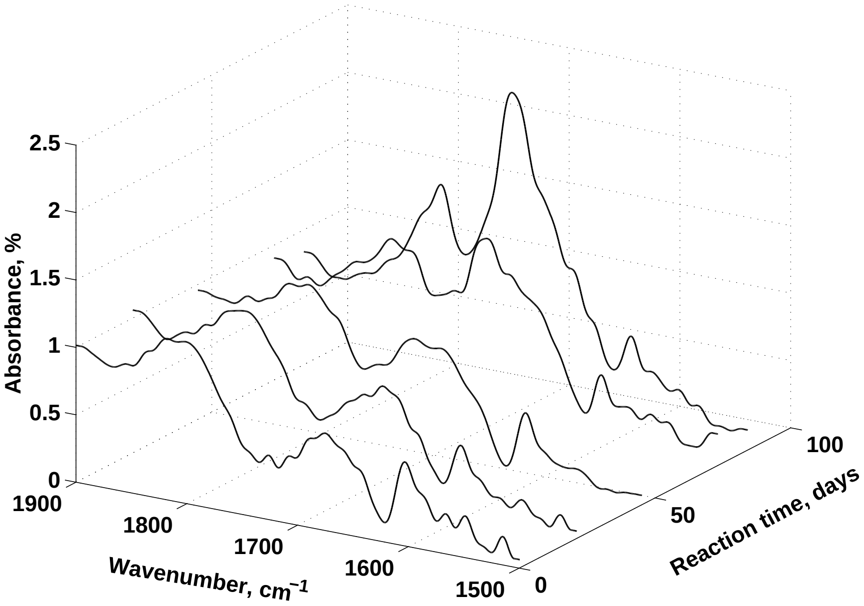

Figure 5.61: Growing oxidation peak in absorbance spectra of Cassida oil, recorded with Bruker FTIR spectrometer equipped with ATR-head and fibers. Resolution $\Delta\overline{\nu} = 4$ cm^{-1}, 100 scans.

The second sample was Shell Tellus Oil of the same type - EHF 5700/2. The oil was aged at 125°C. The reaction was catalyzed by Fe and Cu particles in the way previously described. The total deterioration was observed after only 66 days of aging, what was caused by higher temperature. In Table 5.12 results of standard laboratory tests carried out at Deutsche Shell GmbH are summarized. The kinematic viscosity at 100°C, the dielectric constant and the refractive index exhibit similar initial values as the Cassida oil and the changes caused by the oxidation are also comparable with changes of the Cassida oil. The initial value of the TAN is twice as high as for Cassida oil. In the case of Tellus oil also the refractive index has shown a regular change. The infrared spectra of Tellus oil were prepared in the same way as in the case of the Cassida oil, plotted in Figures 5.62 and 5.63. Values of the oxidation peak are listed in Table 5.13. The spectra exhibit no change for samples up to the 56th day of aging. That indicates a better stability in the operational life of the Tellus oil. Nevertheless, after crossing a stability limit, the Tellus oil undergoes a more rapid deterioration than the Cassida oil. In the Case of the Tellus oil the standard transmission measurement exhibited over 3 times better sensitivity than the ATR-fiber-optic measurement.

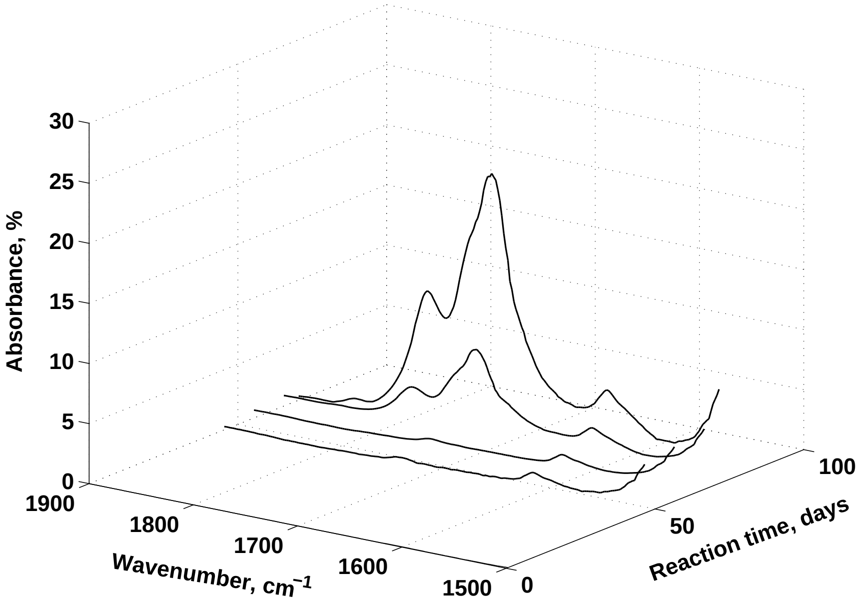

Figure 5.62: Growing oxidation peak in absorbance spectra of Tellus oil, recorded with Thermo-Nicolet FTIR spectrometer. Resolution $\Delta\overline{\nu} = 4$ cm^{-1}, 30 scans.

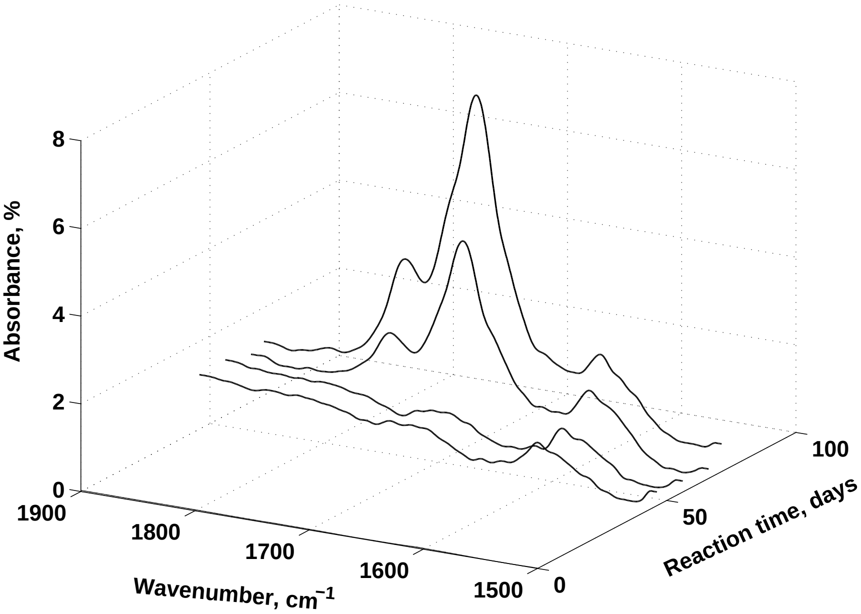

Figure 5.63: Growing oxidation peak in absorbance spectra of Tellus oil, recorded with Bruker FTIR spectrometer equipped with ATR-head and fibers. Resolution $\Delta\overline{\nu} = 4$ cm^{-1}, 100 scans.

Table 5.12: Change of selected properties of Shell Tellus oil, Deutsche Shell GmbH.

Time, days	**Kinematic Viscosity at 100°C, mm^2/s**	**Kinematic Viscosity at 40°C, mm^2/s**	**Total Acid Number, mgKOH/g**
fresh oil	6.754	45.78	0.42
46	6.866	46.88	0.45
56	6.829	47.08	0.46
66	7.563	54.74	2.66
71	8.613	65.73	5.72

Time, days	**Dielectric Constant**	**Refractive Index**
fresh oil	2.22	1.4781
46	2.23	1.4780
56	2.22	1.4782
66	-	1.4790
71	2.55	1.4798

In Figure 5.64 a course of the oxidation process, for transmittance spectra of both Cassida and Tellus oil, is plotted for comparison. It shows that the oxidation process in lubricants runs exponentially with time. As fit to the data, the parameters of the exponential function in the form of:

$$y = y_0 + a \cdot exp\left[\frac{(x - x_0)}{b}\right] \tag{5.173}$$

are for Cassida oil: y_0 = 0.313, x_0 = $7{\cdot}10^{-7}$, a = $5.52{\cdot}10^{-6}$, b = 5.663 and for Tellus oil y_0 = -0.015, x_0 = $5{\cdot}10^{-5}$, a = $1.14{\cdot}10^{-7}$, b = 3.76. Errors of the estimation of the fitting parameters are negligible. Judging from both the transmittance and the ATR-fiber spectra, the exchange-time of the oil can be estimated. In case of the Tellus oil the exchange should take place after about 60 days of aging. In case of the Cassida oil this should be done after about 75 days of aging. It must be emphasized that the reaction conditions were extremely hard for the investigated oils in order to accelerate the degradation process, and the oxidation process in the real operating environment would take much longer. The illustrated strong time dependence of oxidation indicates the difficulty of this estimation and the

Table 5.13: Values of amplitudes and areas of the oxidation peak of Tellus oil calculated from its subtraction spectra.

Reaction time, days	**Peak amplitude, transm. at 1716 cm^{-1},** %	**Peak area, transm. in [1807-1650] cm^{-1},** $\% \cdot cm^{-1}$
46	0.063	0.661
56	0.236	6.244
66	4.784	271.704
71	18.063	1146.330

Reaction time, days	**Peak amplitude, fibers at 1715 cm^{-1},** %	**Peak area, fibers in [1807-1650] cm^{-1},** $\% \cdot cm^{-1}$
46	0.097	3.055
56	0.096	1.634
66	3.202	183.502
71	5.640	342.660

necessity of the increased frequency of laboratory analysis of lubricants. In the cases of both oils Cassida and Tellus, for the first samples measured slight changes in all parameters were too uncertain basis for taking up a decision about the exchange of the oils. As well in case of infrared spectra, first spectral changes, which could be unquestionably identified corresponded to already advanced oxidation. It implies a necessity of an immediate exchange of the lubricants. Such immediate reaction can be undertaken only when measurements are carried out on-line.

The conducted measurements proved a sufficient sensitivity of FTIR-ATR-fiber-optic set-up as applied to on-line monitoring of the deterioration process of lubricants. The sensitivity of the set-up was comparable with the sensitivity of typical transmission measurements and another analysis methods. Nevertheless, only significant deterioration of samples can be detected.

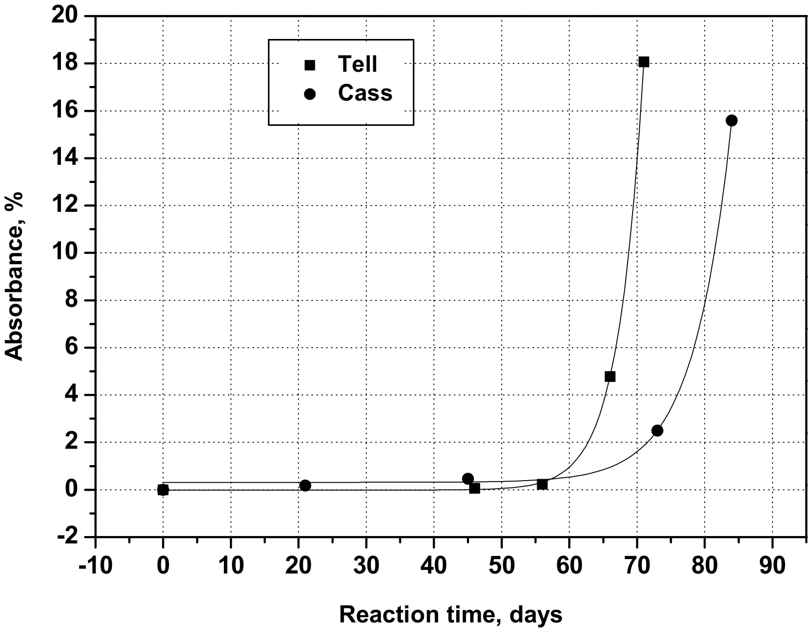

Figure 5.64: Time dependance of the oxidation process of the Cassida and Tellus oil according to transmittance subtraction spectra.

6 ATR Sensor

6.1 Principle of Operation

Measurements presented in the last chapter have proved the adequacy of the FTIR-ATR-fiber-optic measurement technique to on-line monitoring of the aging process of lubricants. Nevertheless, the application of the set-up used in the presented thesis in industrial conditions is unpractical due to:

- the price of FTIR spectrometers
- the sensitivity of FTIR spectrometers to mechanical vibrations
- the price of IR-fibers
- poor mechanical stability of IR-fibers
- limited lengths of IR-fibers
- the liquid nitrogen cooling of MCT detectors

Due to these facts, research on development of a robust and a well-priced ATR-IR sensor for on-line monitoring of aging of industrial lubricants have been conducted. In Figure 6.65 a functional structure of the developed sensor is depicted. The sensor consists of:

- a PC equipped with PCI card
- software
- electronics
- optical bench

A detailed description of above components is presented in the next subsections. The sensor is controlled by a specially written program in GUIDE (Graphical User Interface Development Environment) of MatLab, which controls supply voltages of the optical bench, processes and visualizes collected data. The setting of power supplies of the light source, the motor and the detector of the sensor, as well as data collection follows in a PCI card. A National Instruments PCI-MIO-16E-4 was used.

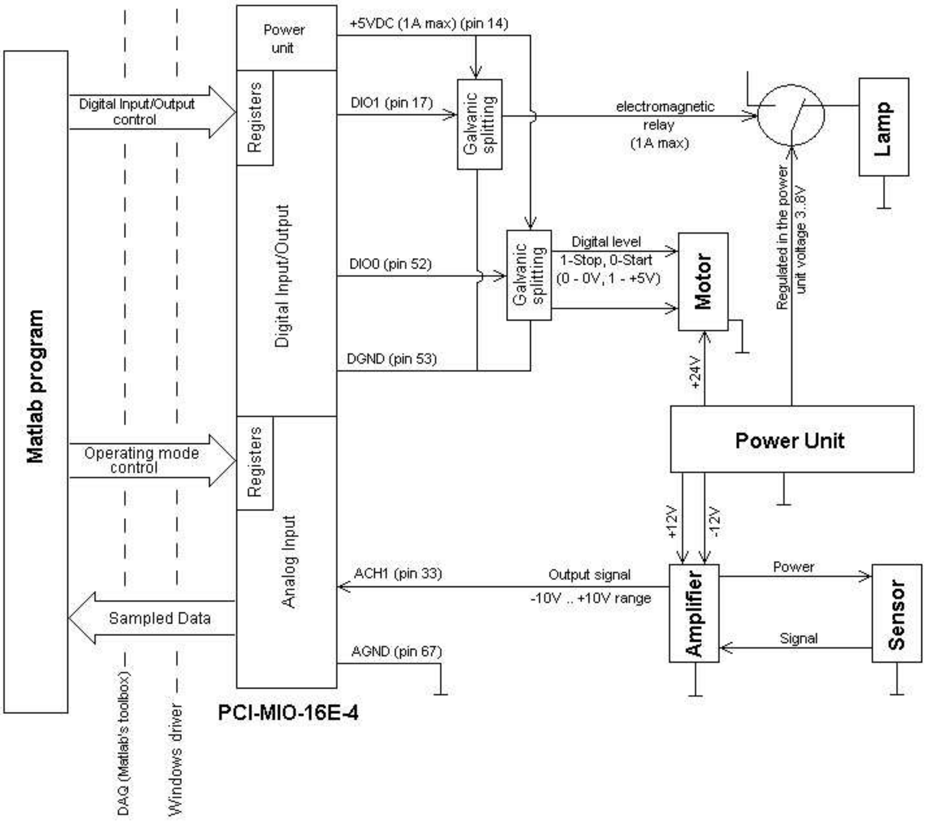

Figure 6.65: Functional structure of the ATR-sensor.

6.1.1 Optical Bench

The optical bench of the developed sensor consists of a simple infrared light source, two collimating mirrors, an ATR crystal, a specially designed filter-chopper and a simple one-element pyroelectric detector. A size and a price of the sensor was the criterion determining the components, which were chosen. A schematic of the optical bench of the sensor is depicted in Figure 6.66 and a picture of the constructed prototype of the optical bench is shown in Figure 6.67.

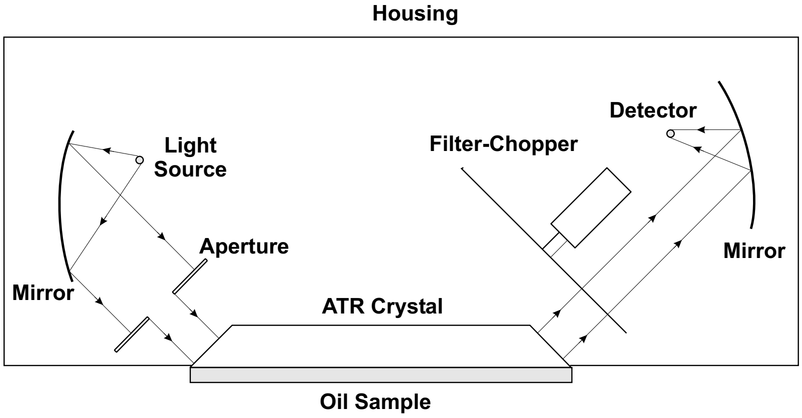

Figure 6.66: Schematic of the developed ATR sensor.

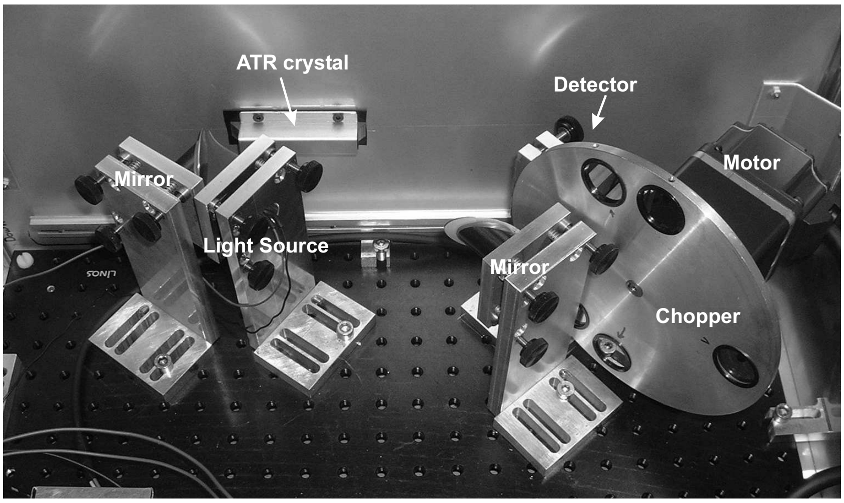

Figure 6.67: Picture of the optical bench of the developed ATR sensor.

A Simple, low-power, infrared light source from Ion Optics, has been used. Contrary to typical spectroscopical light sources, the light source used, was a tungsten filament of a total length of 1 cm and operated at (600-800)°C. Such a light source do not require any additional cooling. The light source emitted a divergent beam, which was collimated and directed to the ATR-crystal by a paraboloidal, aluminium mirror providing a 1 cm diameter of the final beam. The ATR crystal has been purchased from Crystal GmbH. It was made of ZnSe, which exhibits similar optical properties to ZnS crystal, which has been previously used in FTIR-ATR-fiber-optic measurements. The refractive index of the crystal n_c was 2.43.

This provides comparable effective thicknesses to the thicknesses simulated in chapter 5 and with that comparable signals as these obtained with ZnS crystal. The crystal was trapezoidally shaped with dimensions (72mm x 10 mm x 6 mm) and exhibited a total of ten internal reflections on both side-surfaces. Only five reflections contributed to the measured signal, due to the fact that only one side of the crystal was in a contact with a sample. After passing through the crystal, the attenuated light was further directed to the filter-chopper. Behind the filter-chopper a second paraboloidal mirror was placed. It focused the beam on the active area of the pyroelectric detector. Two functions of the filter-chopper are: firstly, the modulation of the light, which is necessary due to the kind of the detector used and secondly, the determination of the investigated wavelengths. As mentioned in chapter 5, pyroelectric detectors, which are sensitive only to AC components of radiation, require an additional modulation of the light. This is usually obtained by a pulsed operation of light sources or by the use of choppers. In the developed sensor, the light source operates in constant voltage mode and signals are modulated by the filter-chopper. The second function of the filter-chopper was fulfilled by the use of narrow-band infrared filters transmitting at 5.00 μm (2000 cm^{-1}) and 5.84 μm (1712 cm^{-1}), L.O.T Oriel. The definition of a narrow-band infrared filter comprises filters with FWHHs of maximum 5 % of the nominal wavelength. The filters transmitting at 5.84 μm delivered the signal corresponding to the oxidation peaks in FTIR spectra. The absolute value of the oxidation signal was gained after its comparison with a reference signal collected with the use of filters transmitting at 5.00 μm. At this wavelength no spectral changes of lubricants occur. Transmittances of the filters were on the order of (60-80) %. The sample transmittances of the chosen narrow-band infrared filters and a sample transmittance spectrum of a lubricant measured with a Thermo-Nicolet FTIR spectrometer are illustrated in Figure 6.68. From Figure 6.68 it is evident that the transmittance of the filter delivering the reference signal is much higher than the transmittance of the other filter.

The novel feature of the filter-chopper was the arrangement of the filters in the chopper wheel. Both kind of filters were used simultaneously; three filters transmitting at 5.84 μm and two transmitting at 5.00 μm. The spatial distribution

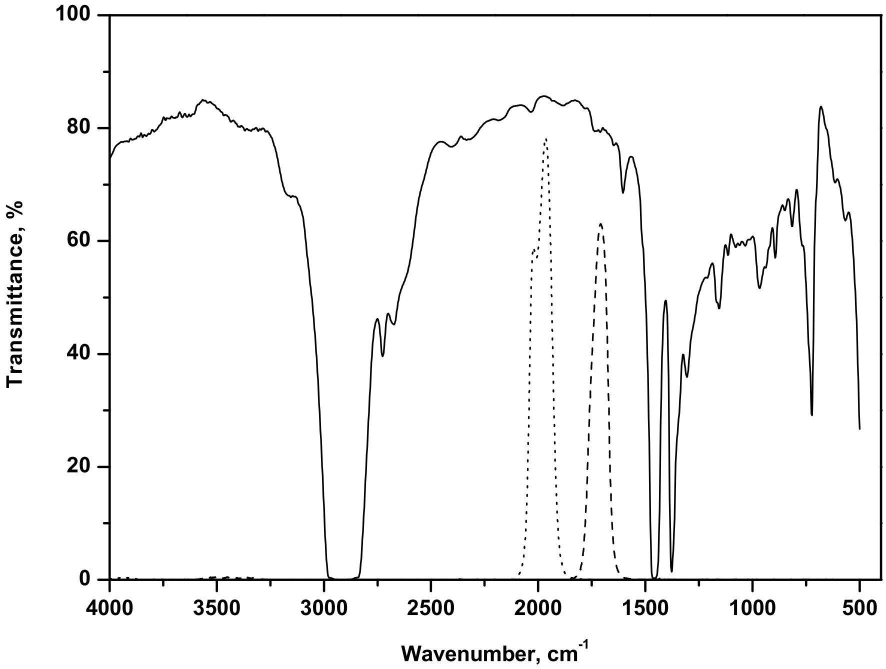

Figure 6.68: Spectrum of a sample oil and used narrow-band infrared filters transmitting at $\lambda_1 = 5.00$ μm (2000 cm^{-1}) - reference and $\lambda_2 = 5.84$ μm (1712 cm^{-1}) - oxidation.

of filters in the chopper wheel enabled collection of reference and sample signals within one measurement cycle. Usually, the collection of both signals demands one of following:

- two separate measurements, each at only one wavelength of interest
- two measurement paths with fixed filters
- special pyroelectric detectors with once for all sealed beam-splitter and filters

None of above solutions provides errorfree measurements. In the fist case, two separate measurements must be compared, while measurement conditions do not remain unchanged. Additionally, the exchange of the filter between the measurements introduces significant errors. In the second case, the construction of two perfectly similar measurement paths is almost impossible and the costs of the equipment are doubled. The best solution providing the best measurement accuracy is the last one. The detectors are, however, more expensive due to the built in beam-splitter and the filters. The built in optics also reduces the field of application of such detectors. The developed filter chopper eliminates possible sources of measurement errors due to the fact, that reference and sample signals are collected simultaneously. Thus, both signals contain the same, easily removable noise. An advantage is also the necessity of only one measurement path and the use of a simple pyroelectric detector. Additionally, the filters in the filter-chopper are flexibly mounted and their exchange is any time possible. Thus, the sensor can be easily adapted to investigations of other fluids in industrial conditions. That broadens significantly the field of application of the developed ATR-sensor. A schematic of the filter-chopper and the induced modulation of the signal is shown in Figure 6.69. As already mentioned, two filters, F1 delivering the reference signal S1 (at 5.00 μm) and three filters F2 delivering the oxidation signal S2 (at 5.84 μm) were not uniformly arranged in the chopper-wheel. The spatial distribution of the filters provided different frequencies for signals S1 and S2, as shown in Figure 6.69. The difference in the amplitudes of signals S1 and S2 originate from different transmittances of the infrared filters used, as illustrated in Figure 6.68, as well as from the radiant distribution according to Planck's radiation law at the temperature of operation.

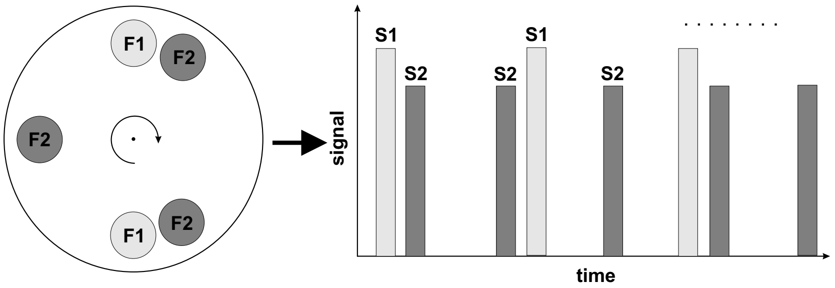

Figure 6.69: Schematic of the designed filter-chopper with distinguished filters F1 and F2, and the course of the modulated signal containing components S1 and S2 corresponding to the filters F1 and F2, respectively.

A spectral information is won from the measured signal through a calculation of a power spectrum of the measured signal. According to Fourier Theorem, each signal *f(x)* can be expressed in a form of Fourier Series:

$$f(x) = \frac{a_0}{2} + \sum_{n=1}^{\infty} a_n \cos nx + \sum_{n=1}^{\infty} b_n \sin nx \tag{6.174}$$

where coefficients a_0, a_n and b_n are related to the given function *f(x)* by integrals:

$$a_n = \frac{1}{\pi}\int_0^{2\pi} f(t)\cos ntdt \tag{6.175}$$

$$b_n = \frac{1}{\pi}\int_0^{2\pi} f(t)\sin ntdt \tag{6.176}$$

Thus, the determination of frequency components of a signal *f(x)* follows through the calculation of the Fourier Transform of this signal. According to the linearity theorem, if a measured signal *f(x)* is a sum of two other *g(x), h(x)* the Fourier Transform of *f(x)* is given by:

$$F(\omega) = \mathcal{F}\,(f(x)) = \mathcal{F}\,(mg(x) + nh(x)) = mG(\omega) + nH(\omega) \tag{6.177}$$

where $F(\omega)$ is a Fourier Transform of the total signal, $G(\omega), H(\omega)$ are the Fourier Transforms of components $g(x)$ and $h(x)$, respectively and *m, n* are optional coefficients. Thus, the components *g(x), h(x)* are distinguishable in the fourier spectrum of the signal $f(x)$.

The spatial distribution of the infrared filters in the developed filter-chopper provides different frequencies of single signals S1 and S2. These frequencies are chosen so that if the chopper wheel rotates with the frequency $\omega = 2\pi f_0$, then the main component of the signal S1 occurs in the fourier spectrum at the frequency $f_{01} = 2f_0$ and the main component of the second signal occurs at the frequency $f_{02} = 3f_0$. Additionally, the spatial arrangement of the filters provides that in the frequency range (0,3f_0) no higher harmonics of the signal S1 occur. In this way clear first components of each signal S1 and S2 are observable. In the frequency range above 3f_0 the higher harmonics of the signals S1 and S2 can overlay, but their observation is unnecessary. In order to interpret the results, the ratio of amplitudes of the main components $A(f_{01})$ and $A(f_{02})$ is calculated. Aging of lubricants reveals in an increase of this ratio as the second component $A(f_{02})$ decreases. The decrease of the second component is connected with the increase of the oxidation peak and with that a decrease of the total light intensity measured at 5.84 μm. In practice valuable information about a signal is shown by its *Power*

Spectrum PS, which is calculated from a Fourier Transform according to:

$$PS = \frac{F(\omega)F^{*}(\omega)}{N} = \frac{|F(\omega)|^{2}}{N} \qquad , W \tag{6.178}$$

where N is the number of transformation points. In some cases a *Power Spectral Density PSD* is also calculated:

$$PSD = \frac{PS}{f_s} \qquad , W/Hz \tag{6.179}$$

PSD is thus a power spectrum normalized to the sampling frequency f_s. An example of a measured signal and its power spectral density are presented in Figure 6.70. From Figure 6.70 a) it is evident that measured signals are low frequent, which is characteristic for pyroelectric detectors. Thus, relatively long measurement durations in comparison to FTIR measurements are necessary. In Figure 6.70 b) first components of the signals S1 → F1 and S2 → F2 are marked. It is visible that these components are clearly separated and can be surely identified.

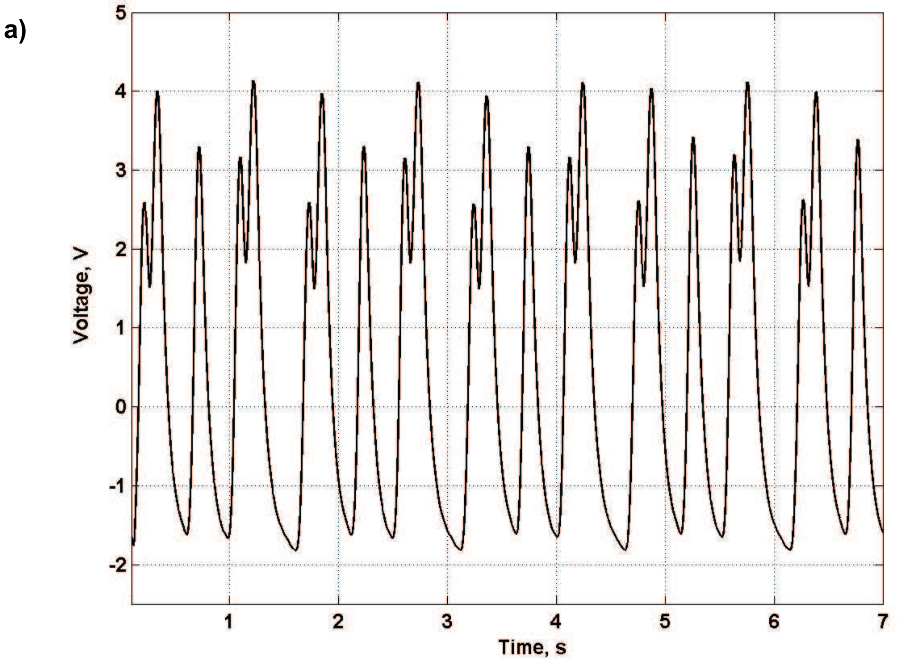

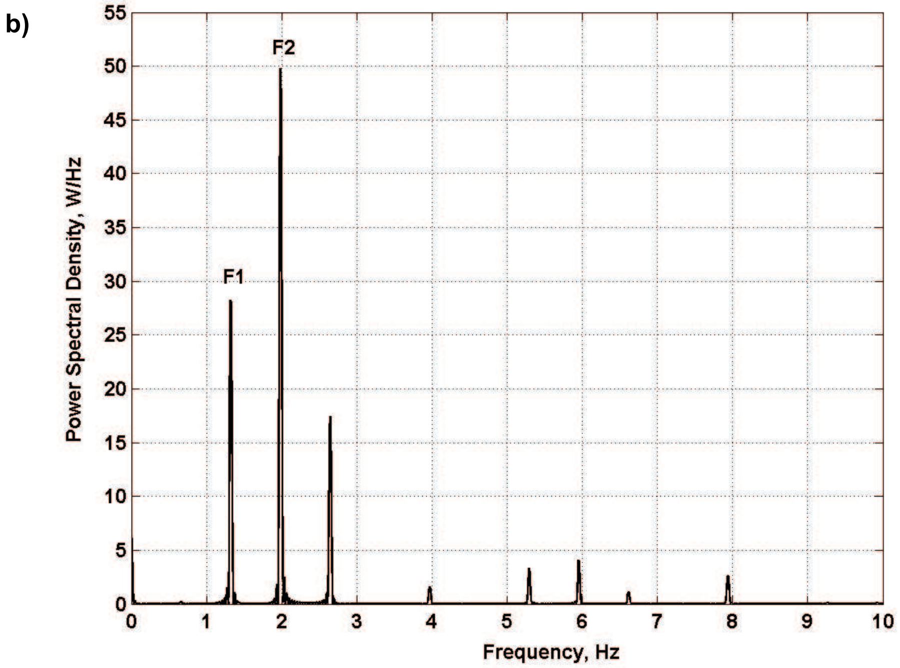

Figure 6.70: Example of the modulated signal a) and its power spectral density b). $f_0 = 0.665$ Hz, $f_{01} = 1.33$ Hz and $f_{02} = 1.995$ Hz.

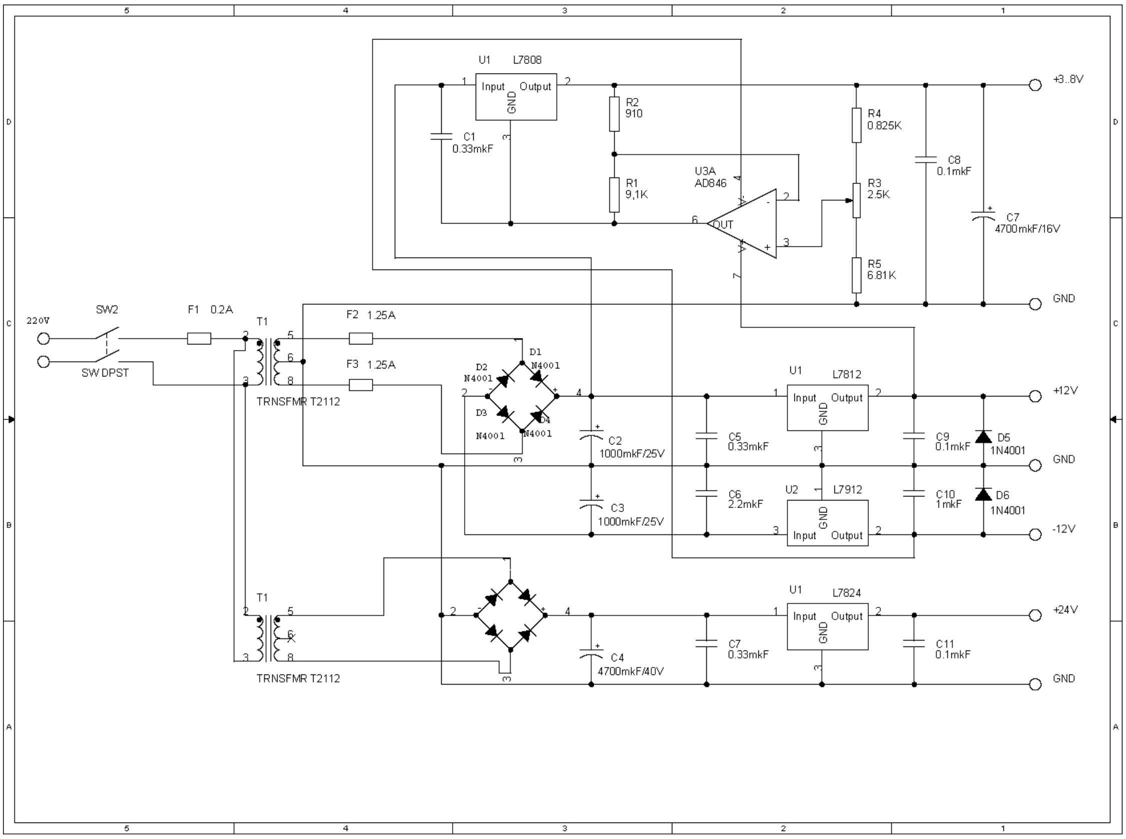

Figure 6.71: Power supply of the developed ATR sensor.

6.1.2 Signal Conditioning

The whole sensor is supplied with a standard 220 V AC net voltage. This supplies the light source, the detector, the motor of the filter-chopper and the signal conditioning unit. All above listed components require different, low DC voltages. These are provided by a power supply unit converting 220 V AC to required low DC voltages. This power supply unit is depicted in Figure 6.71. It is a circuit based on transformers and full-wave rectifiers providing sufficiently constant DC voltages. 24 V DC is necessary to supply the motor of the filter-chopper, the signal conditioning unit requires a ± 12 V DC supply voltage and the light source require maximum 4 V DC.

Two small infrared radiators, Ion Optics, were tried as light sources. The NL8NLC radiator is a simple tungsten filament enclosed in a TO-8 windowless package providing emission angles of up to 40°. The package of the second radiator, ReflectIR, possesses additional built in reflectors collimating the output radiation in order to reduce the emission angles to 15°. Smaller emission angles simplify the adjustment of the remaining optical components of the sensor. Both radiators are enclosed in windowless packagings. The radiators are specially designed in order to provide a high emissivity at low operating temperatures, (600-800)°C. They are connected in series with a 3.3 Ω balast resistance and supplied with 3.6 V DC in the case of ReflectIR and 4 V DC in the case of NL8LNC. The supply voltages provide a sufficient emissivity of the light sources at minimum temperature i.e. provide long operation. The particular supply voltages were established in FTIR measurements with Thermo-Nicolet spectrometer. The function of the balast resistance is to convert a constant voltage (CV) drive into a constant power (CP) drive and with that to provide constant emissivity over a wide range of supply voltages. A load resistance of the ReflectIR radiator is 3.5 Ω and a load resistance of the NL8LNC is 3.2 Ω. That implies power consumptions of 0.897 W and 1.212 W for ReflectIR and NL8LNC, respectively. Because of the pre-collimated output of the ReflectIR radiator, higher signal levels have been obtained with this light source. Due to this fact, and because of the lower power consumption, below presented measurements have been conducted with this radiator.

The signal is collected by a single-element pyroelectric detector, type LT-I Q2, DIAS Angewandte Sensorik GmbH. The sensitive element of the detector was made of $LiTaO_3$ and covered by antireflection coatings increasing the efficiency of the detector. The detector was sealed in a TO-39 housing with a germanium window. The nominal parameters of the detector are:

- Responsivity: R > 250 V/W, (40 times smaller than for MCT detector)
- Noise Voltage: $V_n < 80$ nV/$\sqrt{Hz}$
- Detectivity: $D^* > 8{\cdot}10^8$ cm$\sqrt{Hz}$/W, ($4{\cdot}10^{10}$ cm$\sqrt{Hz}$/W for MCT detector)
- sensitive area: A = 4 mm^2

The sensitivity and the detectivity of the used detector are much lower than the corresponding parameters of the MCT detector used in previously presented

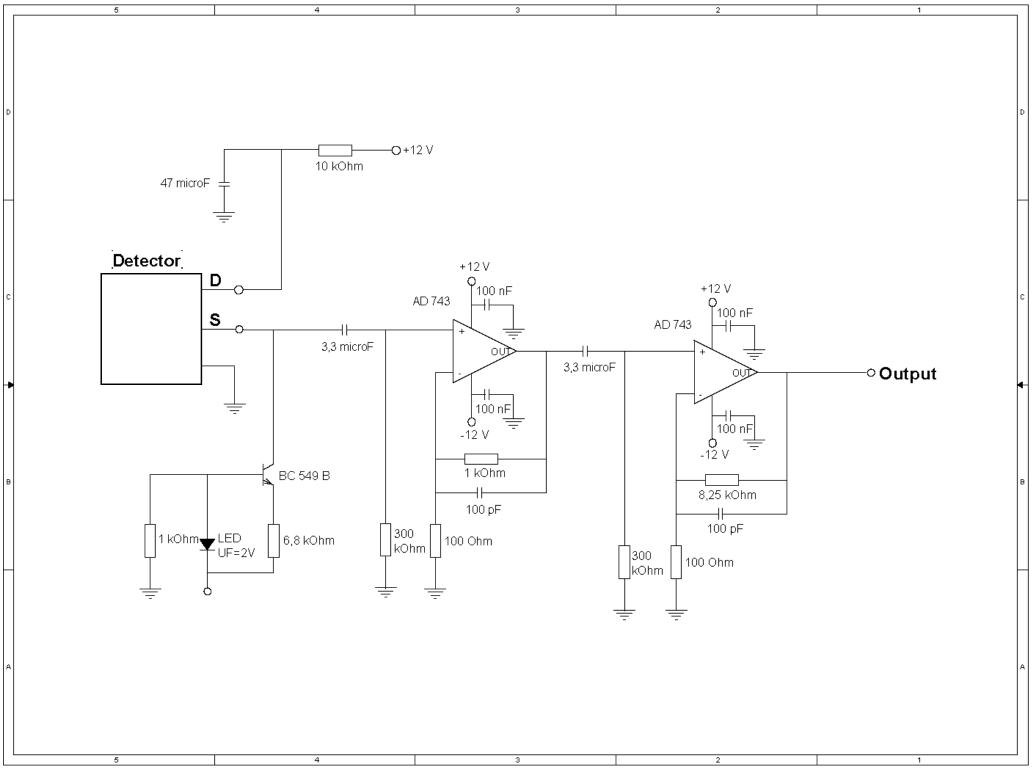

Figure 6.72: Signal conditioning unit of the developed ATR sensor.

spectroscopic measurements, chapter 5. The detector possesses a built in FET-transistor providing high and stable signals at the output of the packaging. The detector was operated in voltage mode. The signal is gained at the source of the FET. Directly behind the detector a simple current source is placed consisting of a bipolar transistor and an LED providing stable working conditions of the next amplifying stage. The amplification of the signal is obtained with the use of two low noise operational amplifiers AD743 designed especially for low-noise infrared sensing applications. The amplifiers are connected in a non-inverting mode. The total gain of the circuit is 825 and the passband of the circuit is (1-10000) Hz. At low frequencies it is limited by a high pass filter eliminating the DC offset of the signal and at high frequencies by a capacitor in the feedback loop of the amplifiers. The signal is further processed by a National Instruments PCI card, PCI-MIO-16E-4. The amplifying circuit of the detector is shown in Figure 6.72.

6.1.3 Measurement Software

As already mentioned, the sensor is controlled by a program written in the GUIDE (Graphical User Interface Development Environment) of MatLab. GUIDE enables creating graphical interfaces simplifying a control of measurements. Behind the user panel of the program, a standard MatLab file containing the actual program code is hidden. A user panel of the written program is shown in Figure 6.73. The program communicates with the PCI card, setting the power supplies of the optical bench and controlling the measurement. In the parameter section of the program, measurement parameters such as: sampling rate, peak detection level, noise level and the measurement duration are set. First, the program sets the supply voltages of the light source, the motor and the electronics. A measurement begins after a one minute delay, which is necessary to obtain constant working conditions of the detector and the electronic circuit. Next, a background signal without the light source is collected. The background signal varies with the temperature of the light source, the temperature of the sample and the temperature inside of the housing of the sensor. These temperature variations influence the accuracy of the measurement and require an additional correction. The correction algorithm uses the values of PSD of a background collected before BB and after BA a sample measurement:

$$\left(\frac{A(f_{01})}{A(f_{02})}\right)_{corr} = \frac{2A(f_{01}) - BB(f_{01}) - BA(f_{01})}{2A(f_{02}) - BB(f_{02}) - BA(f_{02})} \tag{6.180}$$

The measured signal, its power spectrum and the ratio of the amplitudes are visualized in the central part of the user panel of the program. The exact values of peak amplitudes are displayed in the lower part of the user panel. A maximum of seven single measurements can be made. Each form of the signal can be separately saved or magnified in the central window. The program also enables processing of data collected with other devices as long as it is saved in standard ASCII format.

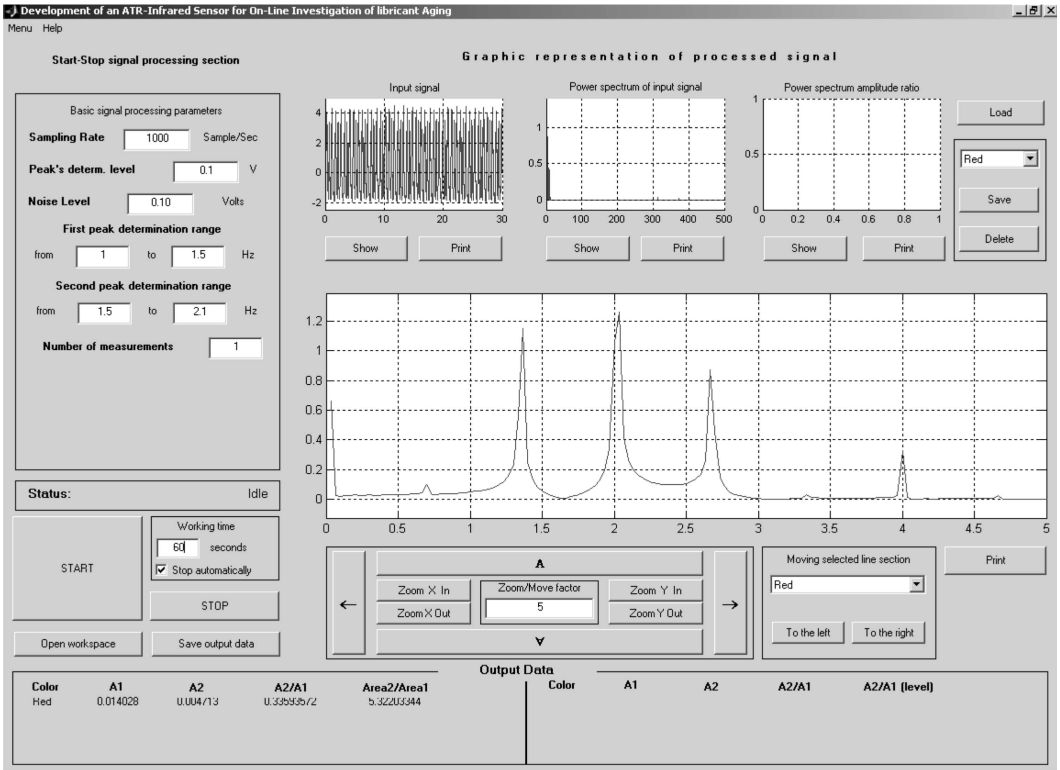
Development of an ATR-Infrared Sensor for On-Line Investigation of libricant Aging

Start-Stop signal processing section

Basic signal processing parameters

Sampling Rate 1000 Sample/Sec

Peak's determ. level 0.1 V

Noise Level 0.10 Volts

First peak determination range

from 1 to 1.5 Hz

Second peak determination range

from 1.5 to 2.1 Hz

Number of measurements 1

Status: Idle

Working time

60 seconds

☑ Stop automatically

Zoom/Move factor 5

Moving selected line section

Red

Output Data

Color	A1	A2	A2/A1	Area2/Area1
Red	0.014028	0.004713	0.33593572	5.32203344

Color	A1	A2	A2/A1	A2/A1 (level)

Figure 6.73: User panel.

6.2 Measurement Results

The measurements have been conducted with the same oil samples as the static and on-line spectroscopic investigations described in the previous chapter: MTF, ATF, CLP, PAO-Ester (AXLE), Cassida and finally Tellus oil. The measurement parameters were: a delay of 60 s, a measurement duration of 60 s, a sampling rate of 1000, a chopping frequency of $f_0 = 0.665$ Hz, the number of transformation points 200000. Three measurement durations were checked: 30 s, 60 s and 120 s. For all of them no difference in the accuracy of measurements has been observed. Thus, if faster measurements are necessary the measurement duration can be shortened. The frequency of the filter-chopper was chosen to obtain visibly separate components S1 and S2 in the time signal. Increase of the frequency up to about 4 Hz does not influence the results due to the fact, that the detector responsivity in the low frequency range is constant. Above 4 Hz a slight decrease of the detector responsivity is observed. The low frequency of the filter-chopper defines the duration of a single measurement. The measurements have shown, that it is impossible to judge the condition of the oil from such a single measurement. A series of repeated measurements must be conducted and averaged. That corresponds to averaging of single scans in FTIR spectroscopy. For the investigated oils, 35 measurements of both fresh and aged oil were always conducted. It corresponds to 30 scans in measurements conducted with Thermo-Nicolet FTIR spectrometer and 100 scans in measurements carried out with ATR-fiber-optic probe, which were presented in the last chapter. The number of single measurements and the duration of the measurement determine the duration of the whole process. This is on the order of tens of minutes, which is significantly longer than duration of any FTIR measurement. Nevertheless, for industrial application such measurement durations are more than sufficient.

The final measurements were conducted in laboratory. The samples were brought to the sensor and exchanged between measurements. First, fresh oil samples were placed at the surface of the ATR-crystal and the signal was measured. Afterwards, the crystal was cleaned and aged oil samples were placed. In all measurements, the background correction was made using the algorithm 6.180. The background correction eliminated the measurement outliers caused by different temperatures of the environment between measurements. The effect of the background correction is illustrated in Figure 6.74. In Figure 6.74 a) a plot of uncorrected signal measured for the MTF oil is shown and in Figure 6.74 b) its corrected version. The final results are plotted in Figures 6.75-6.77. They agree entirely with the results obtained with both FTIR spectrometers. The MTF and CLP oils exhibit a progressed state of oxidation, which is directly seen from the curves. As mentioned previously, a final conclusions can be drown after comparison of the mean values of a measurement series and its standard deviations. The mean values and standard deviations for MTF and CLP oils are listed in Table 6.14. In both cases the difference in mean values of fresh and aged oils is bigger than the standard deviation of a measurement series. For ATF and AXLE oils this is not observed. These results were to expect after FTIR measurements, though in the case of ATF oil its slight degradation were observed in FTIR subtraction spectra.

In Figures 6.78 and 6.79 the measurement results for Tellus and Cassida oil sam-

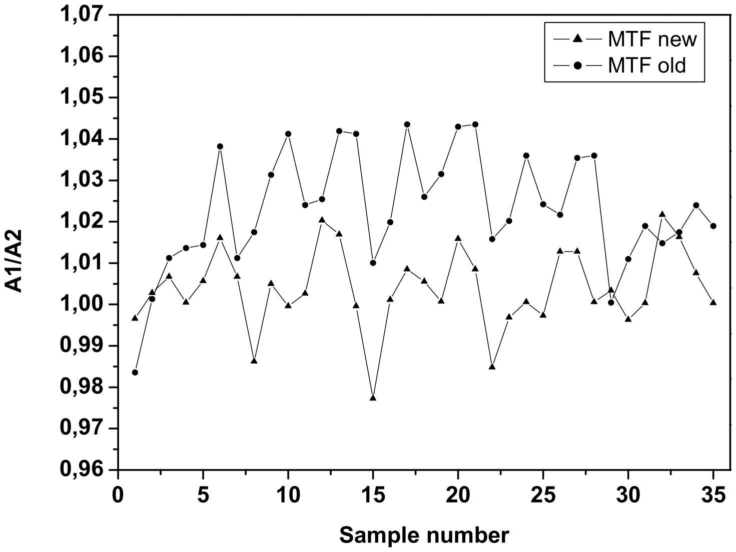

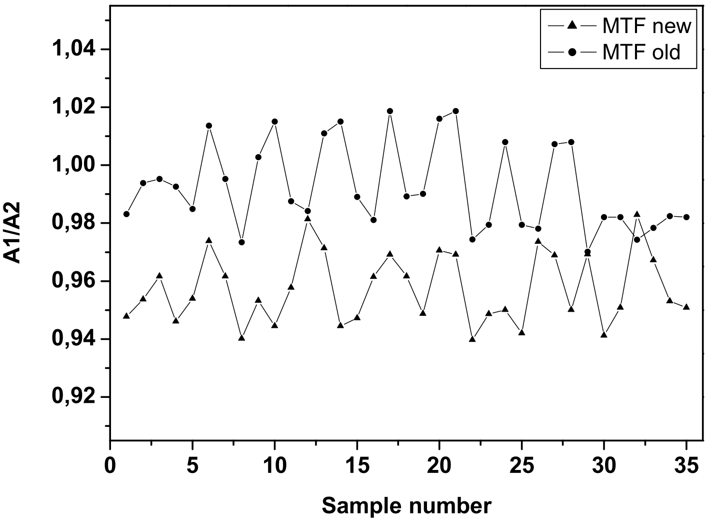

Figure 6.74: The effect of the background correction of the signal measured for the MTF oil. The upper plot illustrates the uncorrected signal. The lower plot illustrates the signal after the background correction.

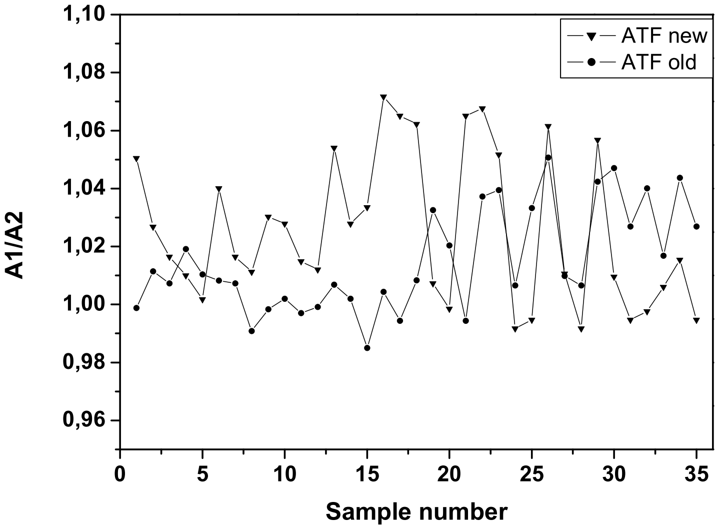

Figure 6.75: Signal measured for fresh and aged ATF oil.

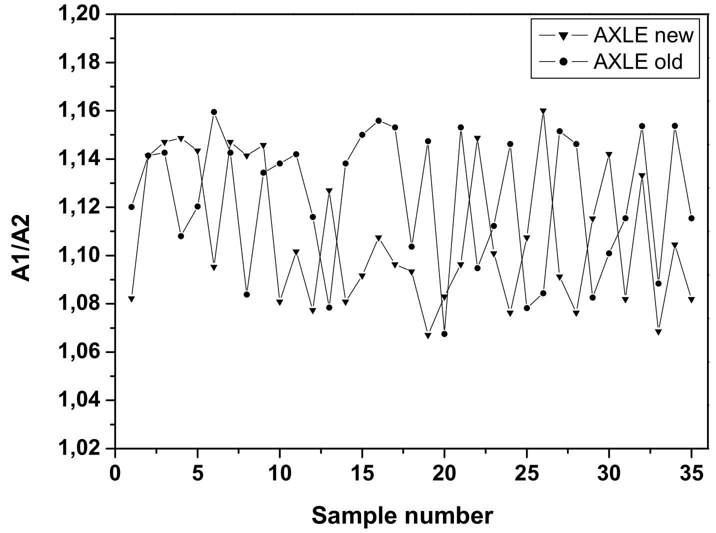

Figure 6.76: Signal measured for fresh and aged AXLE oil.

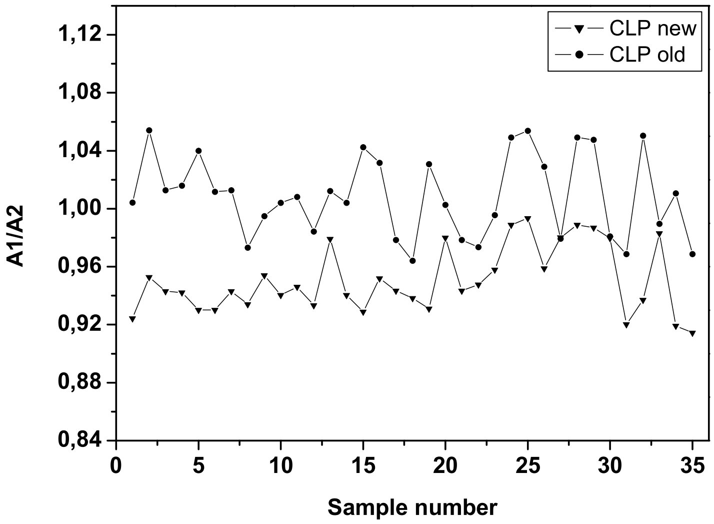

Figure 6.77: Signal measured for fresh and aged CLP oil.

ples are plotted. Each point on the plot is an average from 7 single measurements. Also these results agree with results obtained from spectroscopic measurements. The Tellus oil exhibited stronger degradation already for the sample aged 66 days. In Figure 6.78 the signals measured for the fresh, 46, 56 and 66 days old Tellus oil are shown. Similarly to FTIR-ATR-fiber-optic investigations Tellus oil does not exhibit any qualitative change for inclusively 56 days old sample. The signal change for the 66 days old sample is however, significant and with that the deterioration of this lubricant identified. In the case of Cassida oil the fiber-subtraction spectra have not exhibited strong degradation even for 84 days aged sample. This is proven by the sensor results, which exhibit very slight difference of the signal for the 84 days old oil sample. Nevertheless, comparing the mean values and standard deviations of the measurement series, even in this case the differentiation between the fresh and the aged oil can be made. Thus, the sensitivity of the developed ATR-sensor compares with the sensitivity of the FTIR-ATR-fiber-optic set-up.

The above presented measurements proved the applicability of ATR techniques to on-line infrared investigation of the aging of lubricants. The developed sensor delivered comparable information with FTIR-ATR-fiber-optic measurements.

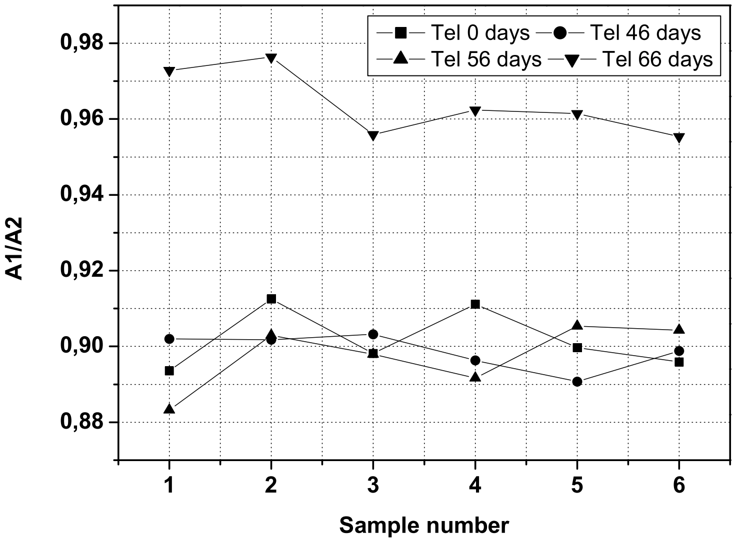

Figure 6.78: Signal measured for fresh and aged Tellus oil.

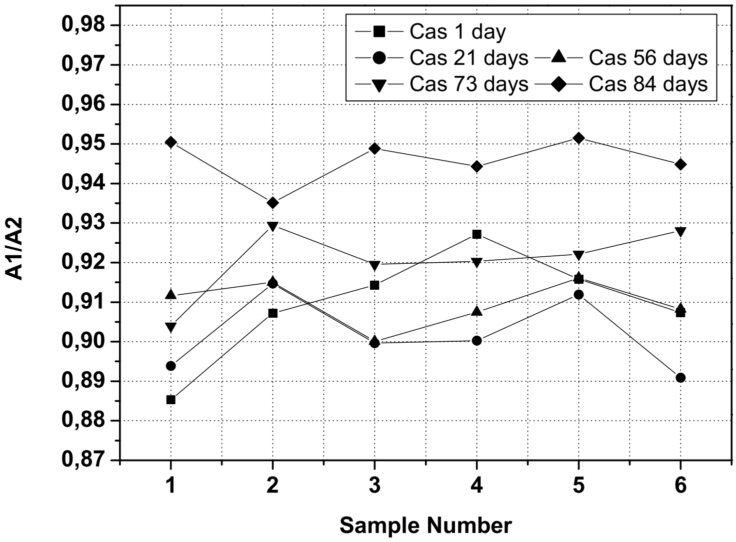

Figure 6.79: Signal measured for fresh and aged Cassida oil.

Table 6.14: Mean values and standard deviations of signal amplitude ratios A1/A2 measured with the ATR sensor.

Sample	**MTF**	**ATF**	**CLP**	**AXLE**
Mean A1/A2 (fresh)	0.95738	1.02538	0.95047	1.10813
Std. dev. (fresh)	0.01214	0.02572	0.02280	0.02858
Mean A1/A2 (old)	0.99246	1.01501	1.00874	1.12344
Std. dev. (old)	0.01499	0.01795	0.02808	0.02790
$\lvert\Delta(Mean)\rvert$	0.03508	0.01037	0.05827	0.01531

Table 6.15: Mean values and standard deviations of signal amplitude ratios A1/A2 measured with the ATR sensor for Tellus and Cassida oil.

Cassida			**Tellus**		
Age	**Mean A1/A2**	**Std. dev.**	**Age**	**Mean A1/A2**	**Std. dev.**
0	0.90953	0.01392	0	0.90184	0.00804
21	0.90188	0.00957	46	0.89881	0.00469
50	0.90976	0.00589	56	0.89757	0.00866
73	0.92059	0.00911	66	0.96407	0.00872
84	0.94585	0.00599	-	-	

Nevertheless, the measurement accuracy should be further improved. One option to increase the accuracy is the application of a stronger light source to deliver higher signals. Additionally, measurements with hot oils samples and the compensation for the temperature of the samples must be made. Finally, the sensor must be checked in industrial conditions.

7 Conclusions

The aim of the presented thesis was to test the applicability of the adaptation of infrared measurement techniques to on-line oil aging monitoring. As mentioned in the introduction, the monitoring of the quality of used lubricants is presently carried out in commercial laboratories. This analysis is connected with a series of disadvantages among which the most important are the lengthy time intervals between the analyses threatening with expensive failures of devices. Therefore the on-line analysis of lubricants comprising several measurements, with one of those being infrared spectroscopy, is necessary. This analysis must however deal with the problems of the instable measurement conditions for example temperature, strong vibrations and an industrial environment. Access to the lubricant samples while in use can be provided by infrared fibers. Therefore, it was first necessary to check the applicability of standard FTIR spectrometers equipped with modern chalcogenide glass fibers and ATR crystals. Advantages of this measurement set-up are the commercial availability of all components, the high sensitivity of the set-up, the wide infrared spectral range enabling observation of complex chemical changes of samples and the duration of the measurement. As the wide spectral range and the short duration of the measurement are undoubtedly positive features, the sufficient sensitivity and the long-time stability of the set-up were not obvious and needed to be proved. The sensitivity of the FTIR spectrometer was limited by the chalcogenide glass fibers and the ATR ZnS crystal, where a strong attenuation of the light took place. This resulted in very small signals demanding the use of an extremely sensitive MCT liquid nitrogen cooled detector. This type of detector cooling presents a serious obstacle for an industrial application of the set-up, but it can be overcome by the use of Peltier-cooled MCT detectors. This type of cooling delivers somewhat higher operating temperatures, which adversely effect the sensors. Whether or not the remaining sensitivity is adequate must be investigated. The sensitivity of the used FTIR-ATR-fiber-optic set-up has been evaluated on four lubricant samples. The samples were measured with the standard FTIR-transmission technique and subtraction curves have been calculated. The results of FTIR-ATR-fiber-optic investigations have been prepared in the same way and the subtraction spectra compared with the spectra obtained in transmission measurements. Although the observed spectral changes were quantitatively smaller, the qualitative information agreed fully with the standard transmission measurements. The commercial availability of the components of the FTIR-ATR-fiber-optic set-up also has a disadvantage in the form of the price. The components, which were used have cost 140,000 Euro. With case of such high prices, only a long time stability of components can justify their use. This stability can however, not be guaranteed, due to the mechanical instability of the chalcogenide fibers and the sensitivity of the FTIR spectrometer to mechanical vibrations. Moreover, the vibrations of the set-up during a measurement can also introduce additional spectral noise destroying the sensitivity of the set-up. Another unexpected problem occurred in a form of the thermal instability of the ZnS ATR crystal making extended reaction monitoring impossible. The proposed diamond crystal, being chemically inert, is a solution for this problem, but its use is connected with additional cost and decreased spectral sensitivity. For all these reasons it has been stated, that an FTIR-ATR-fiber-optic set-up is applicable for extremely sensitive on-line investigations taking place in laboratory conditions. For industrial applications, a more robust and cheaper solution must be found. This solution is the developed ATR-sensor. The sensor consists of a minimum of optical components and a minimum of moving parts. That improves its mechanical stability and allows the operation in industrial conditions. The price of the sensor does not exceed 5,000 Euro, which is an obvious advantage in comparison to the FTIR-ATR-fiber-optic set-up. The novel filter-chopper enables reference and sample signals to be simultaneously collected providing low noise levels and faster measurements. Some disadvantages of the sensor are the measured spectral range (actually limited to one wavelength), the duration of the measurement and the decreased sensitivity when compared to standard FTIR transmission measurements. The sensitivity of the sensor is comparable with this of the FTIR-ATR-fiber-optic set-up. In the case of the sensor, the sensitivity is determined by the responsivity of the detector and the transmittances of the infrared filters, which transmit only (60-80) % of the total radiation. The intensity of the measured signal is partially compensated by larger number of internal reflections in the ATR crystal than in the case of the FTIR-ATR-fiber-optic set-up. The investigated wavelength is defined by the use of narrow-band infrared filters, which limit the applicability of the sensor to the investigation of a specifically strictly defined deterioration process. On the other hand, a simple exchange of the filters enables the use of the sensor in each application, where fluids in industrial conditions are monitored. The duration of the measurement is also defined by the pyroelectric detector. Pyroelectric detectors being most sensitive in a low frequency range, demand the duration of a measurement on the order of tens of seconds. Therefore, similar to FTIR measurements an average from at least 30 measurements is necessary in order to obtain reliable results. That implies total measurement durations on the order of tens of minutes. For industrial conditions this is still more than sufficient. The performance of the constructed prototype was checked on the same lubricants samples as the FTIR-ATR-fiber-optic set-up and the obtained results are more than satisfactory. With both set-ups deteriorated lubricant samples were clearly identified. Thus, the constructed sensor fulfilled all the requirements. In order to further improve the performance of the sensor, more research on the sensitivity, on the accuracy, measurements of hot oil samples and measurements in industrial conditions must be carried out.

List of Symbols

a_0, a_n, b_n	Fourier coefficients
c	Speed of light or concentration of a sample
d_e	Effective thickness
d_F	Diameter of a light source (collimating aperture)
d_p	Penetration depth
f	Focus length
Δf	Frequency band
g	Photon gain
h	Planck's constant
k	Force constant of a spring
$\vec{k}$	Wavevector
l	Sample thickness
m	Reduced mass
n	Vibrational quantum number or refractive index
p	Pyroelectric coefficient
q	Elementary charge
r	Amplitude reflection coefficient
$\vec{r}$	Distance between atoms
t	Amplitude transmission coefficient or time
x	Displacement
A	Absorbance
A_D	Detector area
B	Wien's constant
$B(\overline{\nu})$	Spectrum

BA	Background after
BB	Background before
C_{th}	Thermal capacitance
D	Detector detectivity
D^*	Normalized detector detectivity
E	Energy
E_g	Energy band-gap
$F1$	Filter 1
$F2$	Filter 2
$F(\omega)$	Fourier transform of $f(x)$
G	Generation rate
G_{th}	Thermal conductance
I	Light intensity
$I(\delta)$	Interferogram
I_{ph}	Photocurrent
J	Bessel function of the first art or rotational quantum number
K_0	Modified Bessel function
L_e	Radiance
$L_e(\overline{\nu})$	Spectral radiance
$L_{eD}(\overline{\nu})$	Spectral radiance measured at detector
$L_{eT}(\overline{\nu})$	Spectral radiance transmitted by a sample
$L_{e\eta}(\overline{\nu})$	Spectral radiance emitted by a sample
M_e	Radiant exitance (emittance)
$M_e(\overline{\nu})$	Spectral radiant exitance
N	Noise power
N_{eff}	Effective refractive index of a fiber
N_s	Number of collected data points
P	Internal polarization of a material
Q_e	Radiant energy
R	Reflectivity or the radial part of the wave function or recombination rate
R_{th}	Thermal resistance
R_V	Detector voltage responsivity
S	Poynting's vector

$S1$	Signal 1
$S2$	Signal 2
T	Transmittance or temperature
$T_{corr}(\overline{\nu})$	Corrected transmittance
$T_{meas}(T_i, \overline{\nu})$	Transmittance measured at temperature T_i
V_c	Eigenvector (factor, principal component)
V_n	Detector noise
$W_{e\nu}(\overline{\nu}, T)$	Spectral distribution of the radiant energy
α	Absorption coefficient
α_{max}	Maximum half-angle passed through an interferometer
β	Propagation constant
δ	Retardation (OPD)
δ_{max}	Maximum retardation
ε	Molar absorptivity of a sample
ε_0	Permittivity of vacuum
$\varepsilon(\lambda, T)$	Emissivity of a light source
η	Quantum efficiency
$\eta(\overline{\nu})$	Emission coefficient
θ_c	Critical angle
θ_D	Throughput
θ_i	Incidence angle
θ_r	Reflection angle
θ_t	Refraction angle
$\theta_{\overline{\nu}}$	Phase shift
λ	Wavelength
λ_c	Cut-off wavelength
λ_p	Peak wavelength
μ	Permeability
$\vec{\mu}$	Dipole moment
ν	Frequency
$\overline{\nu}$	Wavenumber
$\overline{\nu}_{max}$	Maximum measured wavenumber

$\Delta\overline{\nu}$	Resolution of an FTIR spectrum
ξ	Efficiency
σ	Stefan-Boltzman's constant
τ_e	Electrical time constant
τ_{th}	Thermal time constant
ω	Angular frequency

Δ	Normalized core-cladding index difference
Φ_e	Radiant power (radiant flux)
$\Phi_e(\overline{\nu})$	Spectral radiant power
Ψ	Wave function
Ω	Solid angle
Ω_{max}	Maximum tolerated solid angle

List of Abbreviations

AN	Anti-wear
ATF	Automatic Transmission Fluid
ATR	Attenuated Total Reflectance
a.u.	Arbitrary Units
BA	Background After
BB	Background Before
CLP	a class of mineral oils with improved corrosion, aging and wear resistance
CLS	Classical Least Squares
DTGS	Deuterated Triglicine Sulfate
EDX	Energy Dispersive XRF
EP	Extreme Pressure
FET	Field Effect Transistor
FTIR	Fourier-Transform-Infrared
FWHH	Half Width at Half Height
GUIDE	Graphical User Interface Development Environment
HLPD	Hydraulic oil enriched with detergents
HMFG	Heavy Metal Fluoride Glass
ILS	Instrument Line Shape or Inverse Least Squares
IR	Infrared
LED	Light Emitting Diode
MCT	Mercury Cadmium Telluride (HgCdTe)
mid-IR	Middle Infrared
MLR	Multiple Linear Regression
MTF	Manual Transmission Fluid
N.A.	Numerical Aperture

NEP	Noise Equivalent Power
OPD	Optical Path Difference
PAO	Polyalphaolefine
PC	Polycrystaline or Personal Computer
PCI	Personal Computer Interface
PCR	Partial Component Regression
PG	Polyglycol
PLS	Partial Least Squares
PS	Power Spectrum
PSD	Power Spectral Density
PTFE	Polytetrafluoroethylene
r.m.s.	Root Mean Square
SC	Single Crystal
SNR	Signal to Noise Ratio
Std. Dev.	Standard Deviation
TAN	Total Acid Number
TBN	Total Base Number
VB	Visual Basic
VI	Viscosity Index
VT	Viscosity-Temperature Characteristics
XRF	X-Ray Fluorescence Analysis
ZDDP	Zinc Diethyl Dithiophosphate

Bibliography

[1] Dieter Klamann. *Lubricants and Related Products.* Verlag Chemie, 1984.

[2] R.M. Mortier, S.T. Orszulik, editor. *Chemistry and Technology of Lubricants.* VCH Publishers, 1992.

[3] A.R. Lansdown. *Lubrication and Lubricant Selection. A Practical Guide.* Mechanical Engineering Publications, 1996.

[4] Theo Mang, Wilfried Dresel, editor. *Lubricants and Lubrication.* Wiley VCH, 2001.

[5] Werner H. Kara. *Schmierstoffe. Herstellung, Eigenschaften, Anwendung.* Deutsche Shell Aktiengesellschcaft, 1986.

[6] Robert Weiss. *Einfluß der Ölalterung auf die Zahnflankentragfähigkeit.* PhD thesis, Technische Universität München, Lehrstuhl für Maschinenelemente, 1994.

[7] Isabel Bayerdörfer. *Einfluß von betriebsbedingten Schmierstoffveränderungen auf die Flankentragfähigkeit einsatzgehärter Stirnräder.* PhD thesis, Technische Universität München, Lehrstuhl für Maschinenelemente, 2000.

[8] J. Li, H. Xu, G. Yin. Determination of alkylated polystyrene pour point depressant by preparative gel permeation chromatography, infrared spectrometry and nuclear magnetic resonance spectrometry. *Analytica Chimica Acta*, 373:73–81, 1998.

[9] M.S. Akhlaq. Characterisation of the isolated wetting crude oil components with infrared spectrosopy. *Journal of Petroleum Science and Engineering*, 22:229–235, 1999.

[10] M.I.S. Sastry, A. Chopra, A.S. Sarpal, S.K. Jain, S.P. Srivastava, A.K. Bhatnager. Carbon type analysis of hydrotreated and conventional lube-oil base stocks by i.r. spectroscopy. *Fuel*, 75(12):1471–1475, 1996.

[11] www.practicingoilanalysis.com.

[12] www.noria.com.

[13] www.pdma.com.

[14] www.wearcheck.ca.

[15] www.maintenanceresources.com.

[16] J. Zieba-Palus, P. Koscielniak. Differentiation of motor oils by infrared spectroscopy and elemental analysis for cryminalistic purposes. *Journal of Molecular Structure*, 482-483:533–538, 1999.

[17] Peter R. Gryffiths, James A. de Haseth. *Fourier Transform Infrared Spectrometry.* John Wiley & Sons, 1986.

[18] Wolfgang Gottwald, Gerhard Wachter. *IR-Spektroskopie für Anwender.* Wiley-VCH, 1997.

[19] Eugene Hecht. *Optik.* Addison-Wesley, 1989.

[20] Heinz Schilling. *Optik und Spektroskopie*, volume 2. Verlag Harri Deutsch, 1980.

[21] Werner Schmidt. *Optische Spektroskopie. Eine Einführung für Naturwissenschaftler und Techniker.* VCH, 1994.

[22] Bruce Hapke. *Theory of Reflectance and Emmitance Spectroscopy.* Cambridge University Press, 1993.

[23] Francis M. Mirabella, editor. *Internal Reflection Spectroscopy. Theory and Applications.* Marcel Dekker, 1992.

[24] N.J. Harrick. *Internal Reflection Spectroscopy.* Interscience Publishers, 1967.

[25] Michael Bass, Jay M. Enoch, Eric W. Van Stryland, William L. Wolfe, editor. *Handbook of Optics*, volume 4. McGRAW-HILL, 2001.

[26] Weissman, Yitzhak. *Fiber optic reflectance probe.* European Patent Application 0 675 352 A2, 1995.

[27] J.R. Berard, R.J. Burger, P.J. Melling, W.R. Moser. *Optical Fiber Coupled Devices for Remote Spectroscopy in the Infrared.* United States Patent 5,170,056, 1992.

[28] L.L. Day, G. Poulter. *Optical Fiber Probes for Remmote Analysis.* United States Patent 5,185,843, 1993.

[29] P.J. Melling. *Fiber-Optic Spectroscopic Probe with Interchangeable Sampling Heads.* United States Patent 5,754,722, 1998.

[30] P.J. Melling. *Mid-Infrared Fiber-Optic Spectroscopic Probe for Use at Elevated Temperatures.* United States Patent 5,923,808, 1999.

[31] P.J. Melling. *Mid-Infrared Fiber-Optic Spectroscopic Probe.* United States Patent 5,754,715, 1998.

[32] Wielfried J. Bartz, editor. *Additives for Lubricants and Operational Fluids*, volume 2. Technische Akademie Esslingen, 1986.

[33] Wielfried J. Bartz, editor. *Additives for Lubricants and Operational Fluids*, volume 1. Technische Akademie Esslingen, 1986.

[34] Brian Smith. *Infrared Spectral Interpretation. A Systematic Approach.* CRC Press, 1999.

[35] Helmut Günzler, Harald Böck. *IR-Spektroskopie. Eine Einführung.* VCH, 1990.

[36] A. Thorne, U. Litzen, S. Johansson. *Spectrophysics. Principles and Applications.* Springer Verlag, 1999.

[37] Jay Orear. *Fizyka.* Wydawnictwa Naukowo-Techniczne, 1993.

[38] Noel P.G. Roeges. *A Guide to the Complete Interpretation of Infrared Spectra of Organic Structures.* John Wiley & Sons, 1994.

[39] ORIEL Instruments. *The Book of Photon Tools.* 2000.

[40] Zbigniew Bielecki, Antoni Rogalski. *Detekcja Sygnalow Optycznych.* Wydawnictwa Naukowo-Techniczne, 2001.

[41] Glenn R. Elion, Herbert A. Elion. *Electro-Optics Handbook.* Marcel Dekker, 1979.

[42] Miles V. Klein, Thomas E. Furtak. *Optik.* Springer Verlag, 1988.

[43] Kenneth A. Jones. *Optoelektronik.* VCH, 1992.

[44] Roman Windpassinger. *Messung von Rauchgasen mittels FTIR-Absorptionsspektrometrie über offene Pfade.* PhD thesis, Technische Universität München, Lehtruhl für Messsystem- und Sensortechnik, 2001.

[45] *Progress in Fourier Transform Spectroscopy.* Springer Verlag, 1995.

[46] A. Simon, J. Gast, A. Keens. *Fourier Spectrometer.* United States Patent 5,309,217, 1994.

[47] Francis M. Mirabella, editor. *Modern Techniques in Applied Molecular Spectroscopy.* Viley-Interscience, 1998.

[48] Barbara Stuart, Bill George, Peter McIntyre. *Modern Infrared Spectroscopy.* John Wiley & Sons, 1996.

[49] John. R. Ferraro, K. Krishnan, editor. *Practical Fourier Transform Infrared Spectroscopy. Industrial and Laboratory Chemical Analysis.* Academic Press, 1990.

[50] W.O. George, H.A. Willis, editor. *Computer Methods in UV, Visible and IR Spectroscopy.* Royal Society of Chemistry, 1990.

[51] Kai Wülbern. *Prozeßgekoppelte Messung von Rauchgasen mit einem Fourier-Spektrometer.* PhD thesis, Technische Universität München, Lehtruhl für Elektrische Messtechnik, 1996.

[52] Stefan Behrning. *Messungen von Belegungen durch Fertigungshilfstoffe auf metallenen Werkstücken mittels mIR-Fasersonde.* PhD thesis, Universität des Saarlandes, Lehrstuhl für Fertigungstechnik, 2001.

[53] A. Ben-David, A. Ifarraguerri. Computation of a spectrum from single-beam fourier-transform infrared interferogram. *Applied Optics*, 41(6):1181–1189, 2002.

[54] A. Keens, N. Rapp. *Method of Obtaining an Optical FT Spectrum.* United States Patent 5,923,422, 1999.

[55] James R. Durig, editor. *Analytical Applications of FT-IR to Molecular and Biological Systems.* D. Reidel Publishing Company, 1980.

[56] K. Rahmelow, W. Hübner. Phase correction in fourier transform spectroscopy: subsequent displacement correction and error limit. *Applied Optics*, 36(26):6678–6686, 1997.

[57] R.L. Richardson, JR. Huseng Yang, P.R. Griffiths. Evaluation of a correction for photometric errors in ft-ir spectrometry introduced by a nonlinear detector response. *Applied Spectroscopy*, 52(4):565–571, 1998.

[58] L. Palchetti, D. Lastrucci. Spectral noise due to sampling errors in fourier-transform spectroscopy. *Applied Optics*, 40(19):3235–3243, 2001.

[59] J.R. Birch, F.J.J. Clarke. Interreflection errors in fourier transform spectroscopy: a preliminary appraisal. *Analytica Chimica Acta*, 380:369–378, 1999.

[60] T.J. Johnson, R.L Sams, T.A. Blake, S.W. Sharpe. Removing aperture-induced artifacts from fourier transform infrared intensity values. *Applied Optics*, 41(15):2831–2839, 2002.

[61] R.C.M. Learner, A.P. Thorne, J.W. Brault. Ghosts and artifacts in fourier-transform spectrometry. *Applied Optics*, 35(16):2947–2954, 1996.

[62] R.J. Keyes, editor. *Optics in Applied Physics. Optical and Infarered Detectors.*, volume 19. Springer Verlag, 1980.

[63] *Infrared Sensors & Systems.* AMA Service, 2002.

[64] *Anwendungen und Trends in der Optischen Analysenmesstechnik.* VDI Verlag, 2002.

[65] A. Rogalski. Infrared detectors: an overview. *Infrared physics and technology*, 43:187–210, 2002.

[66] S.G. Porter. A brief guide to pyroelectric detectors. *Ferroelectrics*, 33:193–206, 1998.

[67] G. Hofmann, N. Neumann. Spannungs- und strombetrieb pyroelektrischer detektoren. *Forschungsbericht der TU-Dresden*, 1980.

[68] G. Hofmann, N. Neumann. Spezifische detektivität pyroelektrischer detektoren bei lateraler wärmeleitung. *Forschungsbericht der TU-Dresden*, 1980.

[69] J. Soo Ko, W. Liu, W. Zhu. Substrate effects on the properties of the pyroelectric thin film ir detectors. *Sensors and Actuators*, 93:117–122, 2001.

[70] T. Schweizer, D.J. Brady, D.W. Hewak. Fabrication and spectroscopy of erbium doped gallium lanthanum sulphide glass fibers for mid-infrared laser applications. *Optics Express*, 1(4):102–107, 1997.

[71] R.K. Sharma, D. Verma, B.B. Sharma. Observation of below band gap photoconductivity in mercury cadmium telluride. *Infrared Phys. Technol.*, 35(5):673–680, 1994.

[72] O. Abe, K. Kawasaki, M. Wakaki. Improvement on nonlinearity and extension of wavelength region using tandem (pv+pc) type hgcdte detector (dual-mct) in ftir spectrometer. *Journal of Electronic Materials*, 28(6):858–863, 1999.

[73] L. Palchetti, G. Bianchini, U. Cortesi, E. Pascale, C. Lee. Assessment of detector nonlinearity in fourier transform spectroscopy. *Applied Spectroscopy*, 56(2):271–274, 2002.

[74] K. Rahmelow. Electronic influences on an infrared detector signal: nonlinearity and amplification. *Applied Optics*, 36(10):2123–2132, 1997.

[75] R.L. Richardson, JR. Huseng Yang, P.R. Griffiths. Effects of detector nonlinearity on spectra measured on three commercial ft-ir spectrometers. *Applied Spectroscopy*, 52(4):572–578, 1998.

[76] P.M. Amirtharaj, J.H. Burnett. *Narrow-gap II-IV Compounds for Optoelectronic and Electomagnetic Applications*, chapter 5.

[77] C.T. Elliot. *Narrow-gap II-IV Compounds for Optoelectronic and Electomagnetic Applications*, chapter 14.

[78] C.T. Elliot, C.L. Jones. *Narrow-gap II-IV Compounds for Optoelectronic and Electomagnetic Applications*, chapter 16.

[79] Y. Iwase, M. Ohmori. *Narrow-gap II-IV Compounds for Optoelectronic and Electomagnetic Applications*, chapter 20.

[80] A. Keens, A. Simon. *Correction of Non-linearities in Detectors in Fourier Transorm Spectroscopy.* United States Patent 4,927,269, 1990.

[81] R.M. Carangelo, D.G. Hamblen, C.R. Brouillette. *Method and System for Photoconductive Detector Signal Correction.* United States Patent 5,136,154, 1992.

[82] R.A. Hoult, R.P. Ragusa. *Detector Preamplifier for Use with a MCT Detector.* United States Patent 4,682,022, 1987.

[83] Keneth R. Beebe, Randly J. Pell, Mary Beth Seasholtz. *Chemometrics. A Practical Guide.* John Wiley & Sons, 1998.

[84] James N. Miller, Jane C. Miller. *Statistics and Chemometrics for Analytical Chemistry.* Prentice Hall, 2000.

[85] H.M. Heise, A. Bittner. Rapid and reliable spectral variable selection for statistical calibrations based on pls-regression vector chices. *Fresenius J. Anal. Chem.*, 359:93–99, 1997.

[86] S.P. Gurden, J.A. Westerhuis, R. Bro, A.K. Smilde. A comparison of multiway regression and scalling methods. *Chemometrics and intelligent laboratory systems*, 59:121–136, 2001.

[87] H. Martens. Reliable and relevant modelling of real world data: a personal account of the developement of pls regression. *Chemometrics and intelligent laboratory systems*, 58:85–95, 2001.

[88] Richard Kramer. *Chemometric Techniques for Quantitative Analysis.* Marcel Dekker Inc., 1998.

[89] S. Wold, J. Trygg, A. Berglund, H. Antti. Some recent developements in pls modeling. *Chemometrics and intelligent laboratory systems*, 58:131–150, 2001.

[90] D.M. Haaland, E.V. Thomas. Partial least-squares methods for spectral analyses. 1. relation to other quantitative calibration methods and the extraction of qualitative information. *Analytical Chemistry*, 60:1193–1202, 1988.

[91] E.R. Malinowski. Theory of error in factor analysis. *Analytical Chemistry*, 49(4):606–612, 1977.

[92] F. Vogt, M. Tacke. Fast principal component analysis of large data sets. *Chemometrics and intelligent laboratory systems*, 59:1–18, 2001.

[93] N.J. Harrick. Vertical double-pass multiple reflection element for internal reflection spectroscopy. *Applied Optics*, 5(1):1–3, 1966.

[94] N.J. Harrick, F.K. du Pre. Effective thickness of bulk materials and on thin films for internal reflection spectroscopy. *Applied Optics*, 5(11):1739–1743, 1966.

[95] N.J. Harrick, A.I. Carlson. Internal reflection spectroscopy: Validity of effective thickness equations. *Applied Optics*, 10(1):19–23, 1971.

[96] J.S. Sanghera, F.H. Kung, P.C. Pureza, V.Q. Nguyen, R.E. Miklos, I.D. Aggarwal. Infrared evanescent-absorption spectroscopy with chalcogenide glass fibers. *Applied Optics*, 33(27):6315–6322, 1994.

[97] A. Bornstein, D. Wolfman, M. Katz. *Attenuated Total Reflection Spectroscopy.* United States Patent 5,070,243, 1991.

[98] Marian Marciniak. *Modalowanie Falowodow Optycznych Metoda Propagacji Wiazki.* Wydawnictwa Komunikacji i Lacznosci, 1995.

[99] M. Young. *Optics and Lasers.* Springer Verlag, 1993.

[100] Matt Young. *Optik, Laser, Wellenleiter.* Springer Verlag, 1997.

[101] G. Mahlke, P. Gössing. *Fiber Optic Cables.* Publicis MCD Corporate Publishing, 2001.

[102] H. Fouckhardt. *Photonik.* B. G. Teubner, 1994.

[103] C. Chen, W. Brown, S. Lo. Calibration transfer from sample cell to fiber-optic probe. *Applied Spectroscopy*, 51(5):744–748, 1997.

[104] I. Tugendhaft, A. Bornstein, Y. Weissman, A. Hardy. Reflection intensity optical fiber sensors for the mid-infrared. *Applied Optics*, 36(6):1297–1302, 1997.

[105] O. Eyal, D. Shemesh, A. Katzir. Connectors, splices and couplers for infrared transmitting optical fibers. *Applied Optics*, 36(6):1185–1190, 1997.

[106] L.E. Curtiss, R.D. Driver. *Fiber Optic Mixer and Spectrometer.* United States Patent 5,212,748, 1993.

[107] Helmut Ehrhardt, editor. *Röntgen Fluorescenz-analyse. Anwendung in Betriebslaboratorien.* Springer Verlag, 1989.

[108] David Dolphin, Alexander Wick. *Tabulation of Infared Spectral Data.* John Wiley & Sons, 1977.

[109] Herman A. Szymanski, Ronald E. Erickson. *Infrared Band Handbook*, volume 1. IFI Plenum, 1970.

[110] Herman A. Szymanski, Ronald E. Erickson. *Infrared Band Handbook*, volume 2. IFI Plenum, 1970.

[111] L.M. Sverdlov, M.A. Kovner, E.P. Krainov. *Vibrational Spectra of Polyatomic Molecules.* John Wiley & Sons, 1974.

[112] Dieter O. Hummel, Friedrich K. Scholl. *Atlas der Kunststoff-Analyse*, volume 2. Carl Hanser Verlag, 1973.

[113] Hohe-Schaar-Str. 36 21107 Hamburg Deutsche Shell GmbH, PAE-Labor.

Acknowledgement

I would like to express my gratefulness to my supervisor Prof. Dr.-Ing. Alexander W. Koch for enabling me to conduct the experiments and his support by writing the thesis. I would like to thank Dipl.-Ing. Eduard Laukotka from Deutsche Shell GmbH for his involvement in the research, the supply of the samples, the chemical analysis of the lubricants and professional help in theoretical problems concerning the deterioration process of lubricants. I am also grateful to Prof. Dr. R. Niessner from the Institute of Hydrochemistry and Chemical Balneology of the Technische Universität München for enabling the analysis of the ATR crystal. I would also like to thank the coworkers of the Institute for Machine Elements, Gear Research Center of the Technische Universität München for delivering fresh and old samples of lubricants. Special thanks to my colleagues for their help and an excellent atmosphere at the Institute for Measurement Systems and Sensor Technology. At last, but not least a special thank to my husband for his professional support and a lot of patience during all these years.

Katarzyna Kudlaty

Publications

1. K. Kudlaty, A.W. Koch, "ATR-IR oil analysis", Proceedings of International Conference for Infrared Sensors & Systems, 14-16 May 2002, Erfurt, Germany
2. K. Kudlaty, A.W. Koch, "Development of an ATR-Infrared Sensor for Online Investigation of Lubricant Aging", International Symposium on Sensor Science, 16-20 June 2003, Paris, France
3. K. Kudlaty, A. Purde, A.W. Koch, "Development of an Infrared Sensor for On-line Analysis of Lubricant Deterioration", Proceedings of IEEE Sensors 2003 Conference, 21-24 October 2003, Toronto, Canada
4. K. Kudlaty, A.W. Koch, "In-situ-Analyse von Schmierölalterung mittels ATR-IR Sensorik", VDI Tagungsband: Sensoren und Messsysteme, 15-16 March 2004, Ludwigsburg, Germany
5. K. Kudlaty, A.W. Koch, "In-situ Lubricant Monitoring with ATR-IR Sensor", Proceedings of International Conference for Infrared Sensors & Systems, 25-27 May 2004, Nuremberg, Germany